



Norwegian University of Life Sciences
Faculty of Environmental Sciences
and Natural Resource Management

Philosophiae Doctor (PhD)
Thesis 2020:30

A novel framework for coupling mesoscale and steady-state CFD models for wind resource assessment

Ny metodikk for kobling av mesoskala
og stasjonære CFD modeller for
vindressurskartlegging

Pablo Durán

A novel framework for coupling mesoscale and steady-state CFD models for wind resource assessment

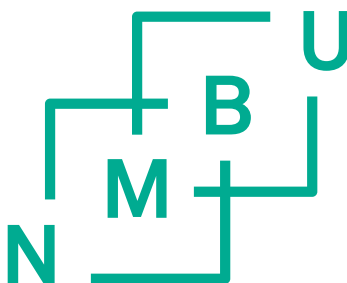
Ny metodikk for kobling av mesoskala og stasjonære CFD modeller for vindressurskartlegging

Philosophiae Doctor (PhD) Thesis

Pablo Durán

Norwegian University of Life Sciences
Faculty of Environmental Sciences and Natural Resource Management

Ås (2020)



Thesis number 2020:30
ISSN 1894-6402
ISBN 978-82-575-1693-2

PhD Supervisors

Professor Muyiwa Samuel Adaramola
Faculty of Environmental Sciences and Natural Resource Management
Norwegian University of Life Sciences
Ås, Norway

Dr. Catherine Meissner
Wattsight AS
Oslo, Norway

Associate Professor Sukanta Basu
Faculty of Civil Engineering and Geosciences
Delft University of Technology
Delft, The Netherlands

Dr. Arne Reidar Gravdahl
WindSim AS
Tønsberg, Norway

Evaluation committee

Dr. Erik Berge
Norwegian Meteorological Institute (MET)
Oslo, Norway

Dr. Carolin Schmitt
EnBW Energie Baden-Württemberg AG
Karlsruhe, Germany

Associate Professor Nils-Otto Kitterød
Faculty of Environmental Sciences and Natural Resource Management
Norwegian University of Life Sciences
Ås, Norway

Acknowledgments

First of all, I would like to thank all my supervisors for their advice and support during my PhD. Sam, you were always encouraging, and I always left your office in a better mood. A special thanks to Catherine for her dedication during my PhD. You were key in the direction and quality of the research. I have not only learned from your technical knowledge, but you were also an example for my professional life. I am also very grateful to Sukanta. It has been a real pleasure to collaborate with you and I hope we have the chance to work together again in the future. You always had those challenging questions that pushed me to investigate further. Last, but not least, thank you Arne for your supervision and useful discussions.

I would like to thank my partner Cecilie for her unconditional support during my PhD. You always showed an honest technical interest in my work and put time and effort into reading and discussing it. I am also grateful to my colleagues at WindSim: Di, Matteo, Ricardo, Tejo and Tine. I have learned a lot with you during these 3 years and it has been a pleasure to go with you to conferences, “julebord” and courses. I would also like to thank all my colleagues at MINA who were part of my everyday life at Sørhellinga. I would like to thank in particular Denis, Franz, Kristel, Mari, Mekdes, Miguel, Nils, Ross, Ruben, Silke, Solrun, Thomas, Vilde, Yennie, Yi-kuang and Yngvild. Finally, I would like to extend my gratitude to the renewable energy group as well as to the administrative team at Sørhellinga.

Sandvika, February 2020

Pablo Durán

Summary

The estimation of the energy production of wind farms is a key factor for the development of wind energy projects. Currently, these estimations utilize only a few onsite measurement points to estimate the wind resource at the location of the wind turbines by means of a wind flow model. One of the most advanced wind flow models utilized in the wind energy industry for this purpose are the steady-state computational fluid dynamic (CFD) models. These models have proven to be successful in modelling the wind flow in complex terrain. Nevertheless, there are some limitations in their applicability at sites with complex weather patterns.

In this PhD thesis, these limitations are addressed by coupling a CFD model with a mesoscale meteorological model (MMM). MMMs are widely used for weather forecast and can reproduce the complex weather phenomena that a CFD model lacks. In this study, the framework to couple both models consists in utilizing the mesoscale simulation results to compute the boundary conditions of the CFD model. Two variants of the meso-microscale coupling approach are here studied.

The first approach consists in utilizing the average values of the mesoscale fields by wind directional sector. It is shown that this approach improves the wind estimations in complex terrain and in areas that are located at the wake of the terrain features of a site. Nevertheless, the approach presents important limitations in sites where the wind blows from few wind directions. The second approach addresses this limitation by extracting weather patterns from the mesoscale simulations by means of a fully automated clustering methodology. This classification technique is capable of extracting the predominant weather patterns and organizing them in a meaningful way. Overall, by downscaling the extracted patterns the modelling error is reduced compared with the mesoscale model. Such a methodology has a lot of potential for wind turbine wake studies as well as for forecasting solutions that utilize CFD models.

Table of Contents

List of Papers	i
1 Introduction	1
1.1 Motivation of the research	1
1.2 Brief review of meso-microscale coupling literature.....	4
1.3 Objectives of the research.....	5
1.4 Thesis outline	6
2 Datasets and methodologies	9
2.1 Validation sites.....	9
2.1.1 Wind measurements.....	13
2.1.2 Digital terrain model	16
2.1.3 Mesoscale simulations	17
2.2 WindSim	17
2.3 Meso-microscale coupling procedure	20
2.3.1 Computation of representative mesoscale fields.....	20
2.3.1.1 Directional average	21
2.3.1.2 Two-level SOM clustering.....	22
2.3.2 Transferring of mesoscale fields to the microscale model.....	25
2.4 Validation metric	27
3 Summary of main results	29
3.1 Capabilities of the SOM2L classification	29
3.2 Capabilities of coupled simulations to downscale mesoscale patterns.....	30

3.3 Validation results	31
3.3.1 Meso-microscale coupling using directional average.....	32
3.3.2 Meso-microscale coupling using SOM2L patterns.....	34
4 Conclusions and future work.....	37
4.1 Coupled models for wind resource assessment	37
4.2 Two-level self-organizing map clustering methodology	38
4.3 Potential of coupled models using SOM2L	39
References	41

List of Papers

Paper I

Meso-microscale coupling for wind resource assessment using averaged atmospheric stability conditions

Durán P, Meißner C, Rutledge K, Fonseca R, Martin-Torres J, Adaramola MS

Published in Meteorologische Zeitschrift (2019)

doi: 10.1127/metz/2019/0937

Paper II

Automated classification of simulated wind field patterns from multiphysics ensemble forecasts

Durán P, Basu S, Meißner C, Adaramola MS

Published in Wind Energy (2019)

doi: 10.1002/we.2462

Paper III

A new meso-microscale coupled modelling framework for wind resource assessment: A validation study

Durán P, Meißner C, Casso P

Submitted to Renewable Energy

Paper IV

Wind resource assessment using a novel meso-microscale coupling framework based on two-level self-organized maps clustering: A preliminary study

Durán P

Manuscript

Chapter 1

Introduction

The goal of this section is to provide to the reader a context for the research described in this PhD thesis. Both the motivation of this research and their objectives are presented. Finally, the contents of the thesis are outlined, including the relation between the scientific articles of this thesis.

1.1 Motivation of the research

Wind energy generation has been identified by the Intergovernmental Panel on Climate Change as one of the renewable technologies with the highest mitigation potential due to its relatively low lifecycle greenhouse gas emissions and competitive costs.¹ The latter has driven a continuous increase in the total installed capacity of wind energy around the world.² By far, the most important factor for the profitability of a wind energy project is the total amount of energy produced,³ which in turn depends on the available wind resource and wind farm layout. In the planning phase of a wind energy project, energy produced by wind farm is estimated through a process called wind resource assessment. The main goal of this process is to predict the windiest locations within a given area. Due to the cost, it is only possible to concurrently measure wind speed and its associated variables (such as wind direction, ambient temperature and atmospheric pressure) in a limited number of locations within a given site considered for a wind farm. Therefore, a method is required to extrapolate few measurements to other locations of interest. For this purpose, the wind industry typically uses the so-called numerical wind flow models. These models are designed to predict the spatial variation of the wind by modelling the physical behavior of the wind flow.

The wind flow models that are mostly utilized for wind resource assessment in the industry can be classified into two categories: linear models and computational fluid dynamic (CFD) models. Historically, linear models⁴ have been popular within the wind industry because of their low use of computational resources. These models solve a linearized version of the equations that govern the motion of the fluids (Navier-Stokes equations). However, these linear models might not capture the influence of the terrain on the wind flow accurately, especially in complex terrain.⁵ On the other hand, CFD models numerically solve the Navier-Stokes

equations by making assumptions about the flow conditions. Different types of CFD models exist, which are mainly differentiated by the way they model the turbulence. The most popular CFD models in the wind energy industry utilizes the steady-state version of the Reynolds-Averaged Navier-Stokes (RANS) equations. RANS models have improved performance compared with linear models (Figure 1.1), while keeping the computational cost relatively low. More advanced CFD models, which are based on large-eddy simulations or unsteady RANS simulations, are commercially available for wind resource assessment. However, they are used to a lesser extent due to their high use of computational resources.⁶ Therefore, the focus of this study is on steady-state RANS models.

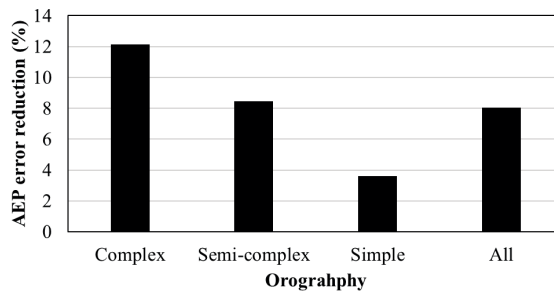


Figure 1.1. Average improvement of the estimated annual energy production (AEP) when using CFD versus linear models for 50 sites with different terrain complexity. Reproduced from Hristov et al. (2014).⁷

The wind flow solution obtained by a steady-state RANS model depends on the selected boundary conditions. These boundary conditions make explicit assumptions about the wind conditions, such as wind speed, wind direction, temperature and turbulence. In the wind energy industry, the boundary conditions are typically assumed to follow analytical formations based on the Monin-Obukhov similarity theory,⁸ as well as to be invariant across the simulated domain. This way of prescribing boundary conditions, referred to in this study as standalone simulations, are sufficient for many wind energy projects. Nevertheless, they present important limitations in sites with complex weather systems, where real conditions can not only differ from this analytical formulation, but also present a significant spatial variation (Figure 1.2).

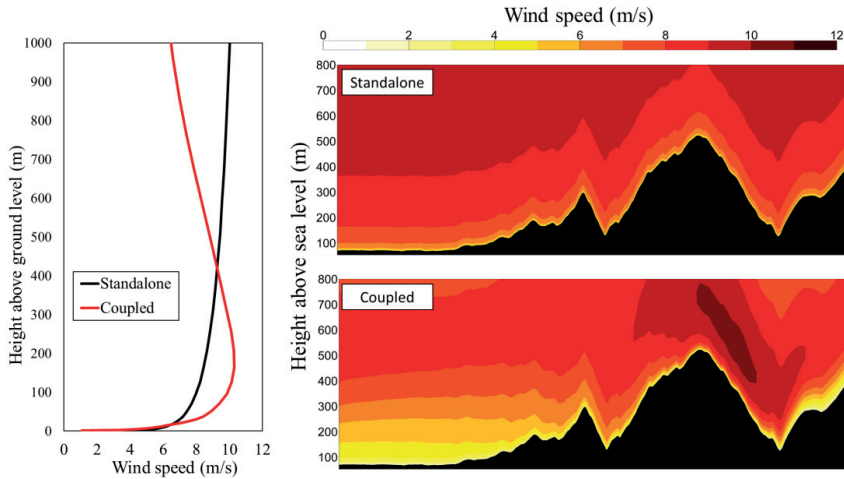


Figure 1.2. Comparison of the boundary conditions for standalone and coupled simulations. Left panel: comparison of the vertical profile of horizontal wind speed. Right panels: comparison of vertical planes of horizontal wind speed.

A necessary step towards improving steady-state microscale models is to have more realistic boundary conditions. The approach that is investigated in this thesis consists of computing the boundary conditions from models that can simulate the weather, the so-called mesoscale meteorological models (MMM). This approach is referred to in the literature as direct meso-microscale coupling.⁶ Nested domains in the MMM are used to physically downscale the global circulation to the regional winds and then to the atmospheric boundary layer wind flow (Figure 1.3). It is expected that the wind flow solution of a direct meso-microscale coupling approach would benefit from both more realistic weather conditions by the MMM and from a proper inclusion of the local orography by the microscale model. Recently, publicly available mesoscale data have been published at the New European Wind Atlas database.⁹ Other similar mesoscale simulation databases exist, like the Dutch Offshore Wind Atlas.¹⁰ It is expected that this kind of databases will be increasingly common in the future, and in order to exploit them, the development of direct meso-scale coupling methodologies is required.

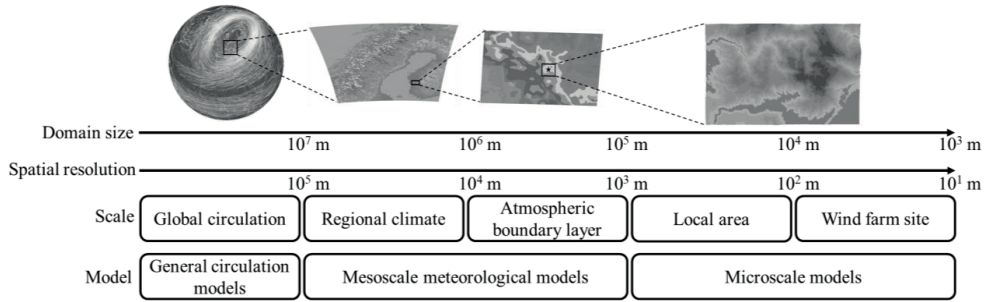


Figure 1.3. Spatial scale ranges of different wind flow modeling approaches. Adapted from Sanz et al. (2017).⁶

1.2 Brief review of meso-microscale coupling literature

As reported in Paper I, meso-microscale coupling models are widely studied within the wind modelling field. Most of the reviewed literature on meso-microscale coupling can be classified according to the modelling approach utilized at the microscale level:

- i. Direct coupling using an unsteady microscale model like large-eddy simulations or unsteady RANS
- ii. Direct coupling using a steady-state microscale model to simulate some timesteps
- iii. Steady-state microscale model using analytical boundary conditions, which is then scaled by the mesoscale wind speed at a given grid point(s)

As previously mentioned, approach (i) is not feasible for most of the wind industry given the extensive use of computational resources; while approach (ii) is mostly used for urban studies (like pollution dispersion) in order to simulate a specific event. Approach (ii) cannot be applied for wind resource assessment since it would require simulating too many timesteps (for example, each hour of a year). Approach (iii) has applications in wind energy for site screening or for the elaboration of wind atlases. Nevertheless, this approach does not solve the problem of unrealistic boundary conditions as it also uses analytical boundary conditions to force the model, and the mesoscale results are only used to scale the model. In wind resource assessment, the scaling is typically conducted using onsite measurements, which are regarded as a better representation of real wind conditions.

There are two challenges when using direct meso-microscale coupling with steady-state models for wind resource assessment purposes. First, it is necessary to define how many and which

mesoscale fields would be used to compute the boundary conditions. The idea is that the selected or computed fields are representative for the most predominant conditions at the site. Secondly, once having these representative mesoscale fields, a procedure to compute the boundary conditions is required. This is a problem that is commonly addressed by the studies that use approaches (i) and (ii), and much of their insights were used in this study. Nevertheless, in most of the studies the problem of finding representative mesoscale fields is typically not addressed. From the literature survey, the only work that deals with this problem is the study carried out by Duraisamy (2014).¹¹ In that study, the 3-D simulated mesoscale timeseries are classified using a *k*-means clustering approach, obtaining 64 fields that are then downscaled with a microscale model. The validation of the methodology in that study is rather limited as it is only applied at one site. Another shortcoming is that the applied clustering approach requires to define a priori the total number of clusters, which can lead to repeated or insufficient clusters. The study presented in this PhD is similar in the sense that classification approaches are applied to obtain representative mesoscale fields, which are then downscaled. However, this PhD thesis is focused as well on the automatization of the mesoscale classification and on a wider validation of the capabilities of the meso-microscale coupling models.

1.3 Objectives of the research

The aim of the research presented in this PhD thesis is to develop methodologies that enable the combined use of MMM simulations with steady-state RANS modelling for wind resource assessment applications. The main challenge of this meso-microscale coupling method is to cope with the different ways these models deal with time. MMM simulations are time dependent (also called transient), while steady-state RANS models are time independent. Thus, the challenge is to establish the number of coupled simulations needed to fairly represent the different conditions simulated by the MMM. This challenge is analogous to determining how many and which frames of a video are required to sufficiently convey the information contained in it.

It is expected that some information from the mesoscale simulation will be lost through the coupling procedure. On the one hand, the use of a steady-state model in the microscale will necessarily be unable to transfer transient phenomena, especially during unstable conditions. On the other hand, due to the simpler physics modeled by the RANS model used in this study, it is not possible to take into account the same physical processes as the mesoscale model.

Therefore, an additional objective of this study is to have a better understating of the limitations of the direct coupling methodologies developed. It is important to determine in a quantifiable manner which modelling approaches are more adequate for different types of terrain complexity, atmospheric stability conditions and local weather phenomena.

In summary, the specific objectives of this research are:

- i. Develop meso-microscale coupling methodologies for steady-state microscale models that utilize a reasonable number of simulations (≤ 36)
- ii. Quantify the gain in utilizing the developed meso-microscale coupling methodologies for different type of terrain and weather conditions
- iii. Identify the limitations of the developed meso-microscale coupling methodologies and the possible solutions to further enable their use for wind resource assessment

In the research articles of this thesis, two meso-microscale coupling methodologies are developed. In Papers I and III, a directional average approach is utilized, while Papers II and IV utilizes an approach based on neural networks. Both methodologies comply with using a reasonable number of simulations. Furthermore, the approach based on neural networks achieve this in a fully automated manner. In the articles, the coupling methodologies are validated at different sites with a variety of terrain and wind conditions. The capability of the coupling methodology to downscale different mesoscale wind patterns is evaluated qualitatively and quantitatively.

1.4 Thesis outline

The remaining of the PhD thesis is structured as follows: In Chapter 2, all the materials and methodologies utilized through the research are presented. These consist of the datasets used for the modeling and validation of the studied sites, as well as their corresponding mesoscale simulations. In the same section, technical details are provided for the microscale model and for the meso-microscale coupling methodology. Finally, the error metric utilized in the validation study is described. To avoid repetition, detailed information presented in the research articles of this thesis are not repeated in this synopsis. This especially applies to the datasets of the validation sites, the coupling methodologies and the validation metric. In Chapter 3, the results and findings of the articles are summarized. The results are organized into three main topics: (i) capabilities of the classification techniques utilized, (ii) capabilities of the coupled simulations to downscale mesoscale patterns and (iii) validation study results.

This PhD thesis contains four research articles, and the relation between them is outlined in Figure 1.4. The research contained in these articles can be summarized as a development and validation of two meso-microscale coupling methodologies. The main difference between the methodologies is the procedure utilized to obtain the representative mesoscale fields. One of these methodologies correspond to a simple approach that consists of using the average values of the MMM variables to prescribe the boundary conditions to the microscale model, which is proposed and validated in Paper I. In parallel to this work, a more sophisticated classification methodology was proposed in Paper II. This classification methodology is based on a machine learning technique, called self-organizing maps (SOM), to obtain prevalent patterns in a dataset in a fully automated fashion. In Paper II, the focus was only on the classification methodology and on proving its capabilities in classifying relevant wind patterns, in particular, wind speed profiles. Paper III further develops the work of Paper I, by introducing some improvements and more importantly, making use of a larger sample of sites and observational points to validate the coupling methodology. Finally, Paper IV utilizes the same classification method developed in Paper II to obtain the predominant patterns of a mesoscale simulation. These patterns are downscaled and validated using an identical coupling methodology as in Paper III.

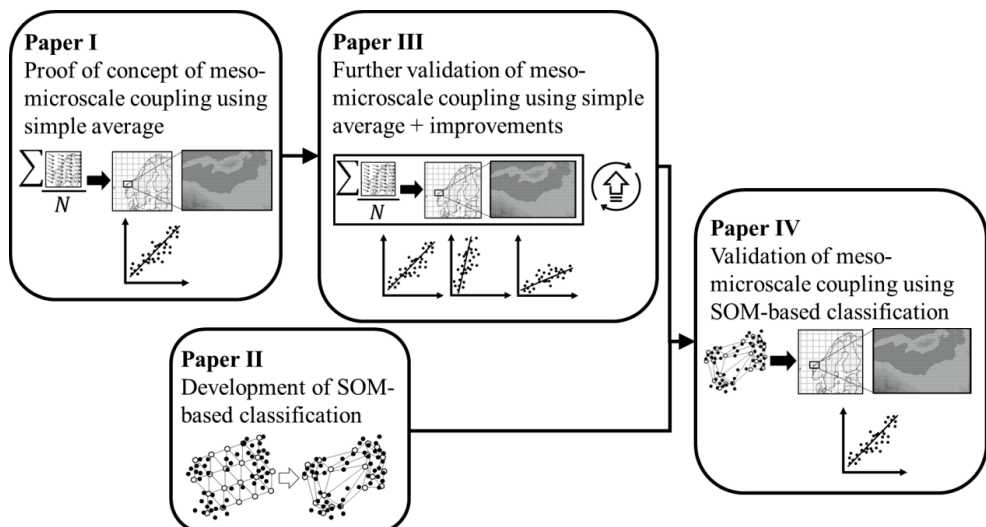


Figure 1.4. Relation of the research papers in this PhD thesis

Datasets and methodologies

The datasets and methodologies used to carry out this PhD study are presented in this chapter. In Figure 2.1, the relationship between these elements is outlined. The terrain datasets are utilized to build the digital terrain models of the microscale model of WindSim. This microscale model is coupled with the mesoscale simulations through a transferring procedure. The simulation results of this procedure are compared to the results of the standalone WindSim model, which are utilized as a benchmark. The results from both models are compared against onsite measurements using crosscheck prediction errors.

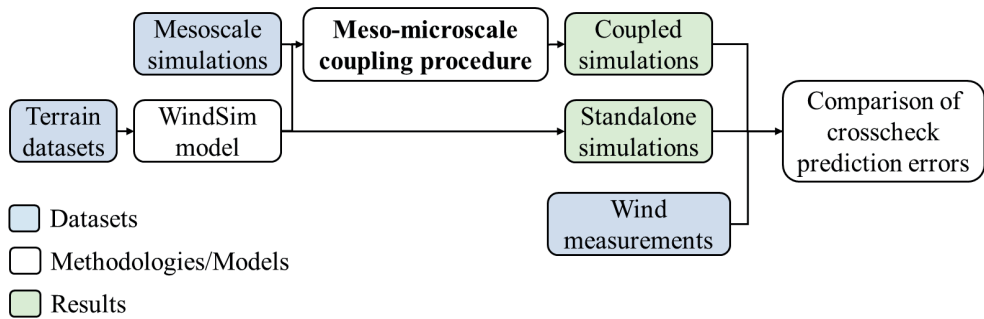


Figure 2.1. Relation of the models, methodologies and datasets used in this PhD thesis. The main contributions of the research are in the meso-microscale coupling procedure (indicated in bold).

The contributions of the research conducted in this thesis are mainly in the meso-microscale coupling procedures. Other minor contributions were introduced in the microscale modeling and in the crosscheck prediction error procedure of WindSim. Further technical details on the datasets, methodologies and models are provided in the following subsections.

2.1 Validation sites

Six sites, which are listed in Table 1, are used in this PhD study. All of them correspond to commercial wind energy generation projects in different states of development. Datasets from most of the projects were only provided for the purpose of this research, and therefore georeferenced data and absolute values of the measurements are not disclosed. The only site without restrictions regarding the datasets is Honkajoki. Non-public datasets for the Honkajoki

Datasets and methodologies

and CA sites were provided by the Novia University of Applied Sciences in Finland and RWE Renewables Americas LLC in the US, respectively. The remaining datasets were provided by Mainstream Renewable Power in Chile.

Table 1. Validation sites used in the research articles of this PhD thesis.

Name	Location	Meteorological conditions	Paper
Honkajoki	Finland	Very stable conditions	I
CM	Southern Cone	Near-neutral to stable conditions	III
CA	North America	Very stable conditions	III
CL	Southern Cone	Strong day-night cycle	III
CK	Southern Cone	Strong day-night cycle	III and IV
PS	Southern Cone	Near-neutral to stable conditions	III

None of the projects presented in Table 1 were utilized in Paper II. Instead, the locations of the FINO-1 and Cabauw meteorological towers were used. Due to the nature and scope of Paper II, no measurements were required, and these locations were only used because they are well-known experiments in the wind energy community. For each of the sites listed in Table 1, three kinds of datasets are used to carry out the study:

- 1) Wind measurements
- 2) Terrain
- 3) Mesoscale simulations

An overview of the datasets is presented in Figures 2.2-2.7. In the following subsections details of the datasets are provided.

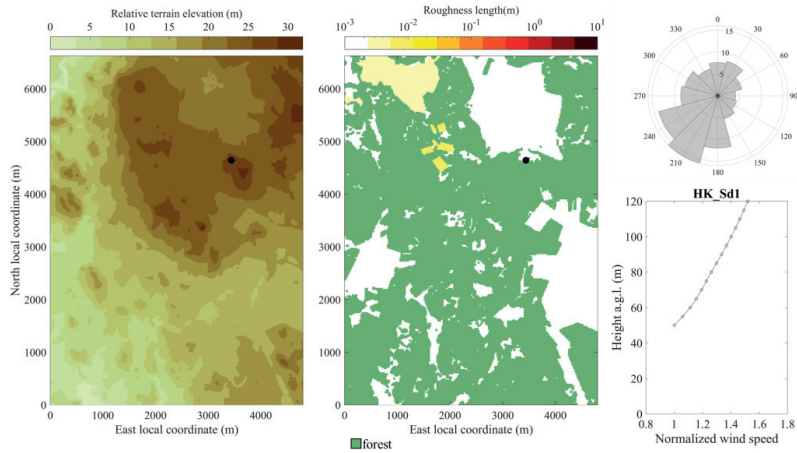


Figure 2.2. Terrain and wind characteristics at the Honkajoki site. The locations of the measurement are indicated by black circles in the maps. Polar and radial axis of the wind rose correspond to the wind direction (°) and frequency (%), respectively. The instrument used to compute the wind characteristics is indicated above of the bottom-right panel.

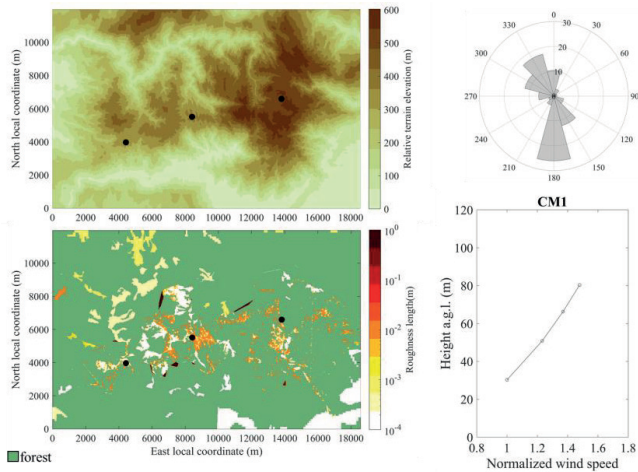


Figure 2.3. Same as Figure 2.2 but for the CM site.

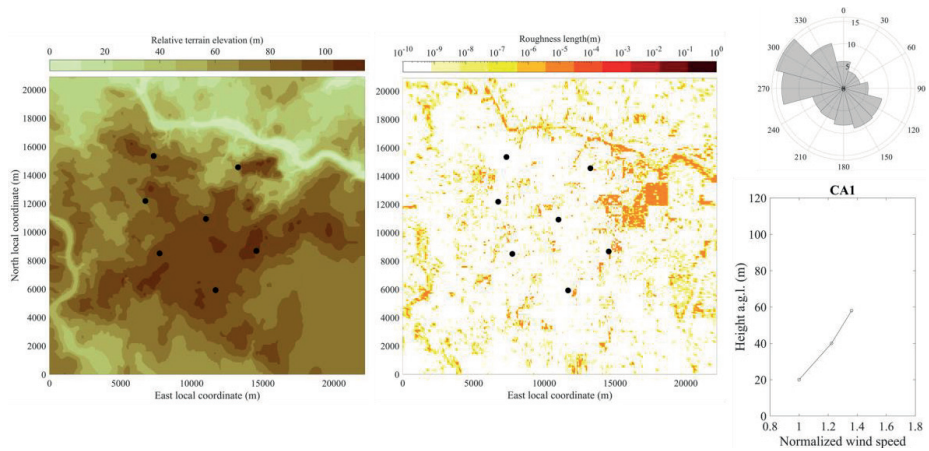


Figure 2.4. Same as Figure 2.2 but for the CA site.

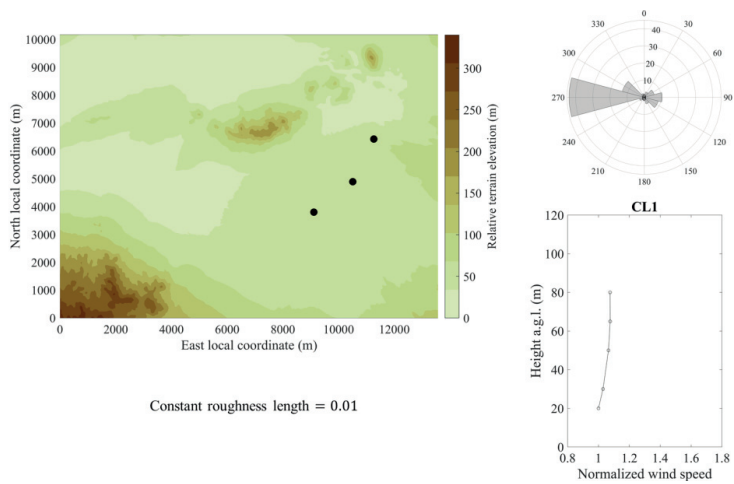


Figure 2.5. Same as Figure 2.2 but for the CL site.

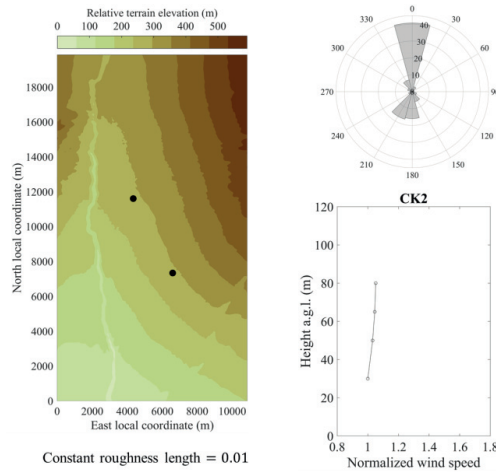


Figure 2.6. Same as Figure 2.2 but for the CK site.

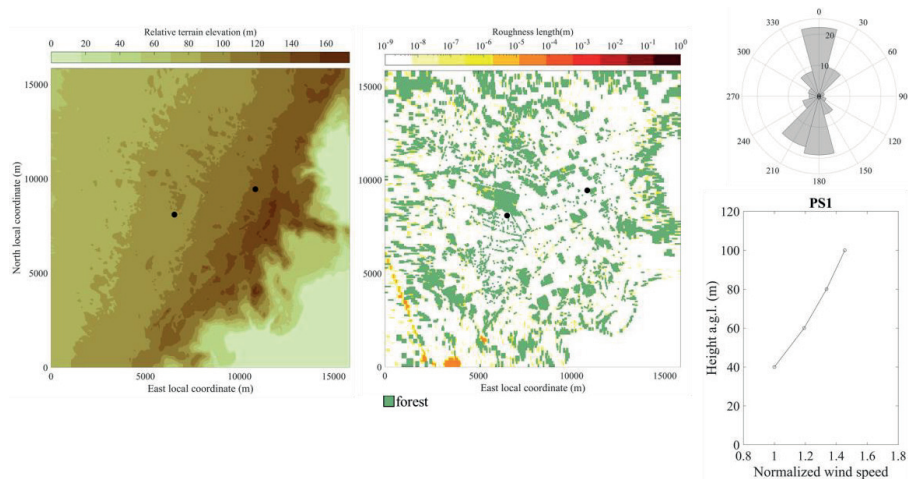


Figure 2.7. Same as Figure 2.2 but for the PS site.

2.1.1 Wind measurements

Onsite measurements of the wind conditions at the sites were obtained through different instruments. The type of instruments utilized for these measurements are some of the ones typically used for wind resource assessment: cup anemometers, wind vanes and light detection and ranging (LiDAR) systems (Figure 2.8). The measured variables that are used in the validation studies of this thesis are the wind speed and wind direction, which are averaged every 10 minutes. Other measured variables that were not directly used in the study include turbulence intensity (or standard deviation of the wind speed), vertical wind speed,

temperature, humidity and pressure. Most of these variables are used for suitability studies and energy yield calculations, which are beyond the scope of this work.



Figure 2.8. Instruments utilized at the CL site. Left and center panels: Anemometer and wind vane, respectively, mounted in a meteorological mast. Right panel: Deployed LiDAR. Courtesy of Mainstream Renewable Power.

Cup anemometers and wind vanes were calibrated using the parameters provided by external laboratories. The data collected from cup anemometers and wind vanes are cleaned for invalid or unrealistic values, as well as for icing events, utilizing the Windographer software (Figure 2.9). Cup anemometers and wind vanes are mounted into meteorological masts. Usually two anemometers are mounted per vertical level in order to prevent tower distortion (Figure 2.10). The data from both anemometers are combined into one timeseries, which considers the mast wake for a given range of wind directions.

The data collected by the LiDARs is already filtered from low quality measurements by the software included in the instrument. The data from some LiDAR brands had to be cleaned or corrected due to improper wind direction measurement. Further details on the type and number of instruments per site can be found in Papers I, III and IV.

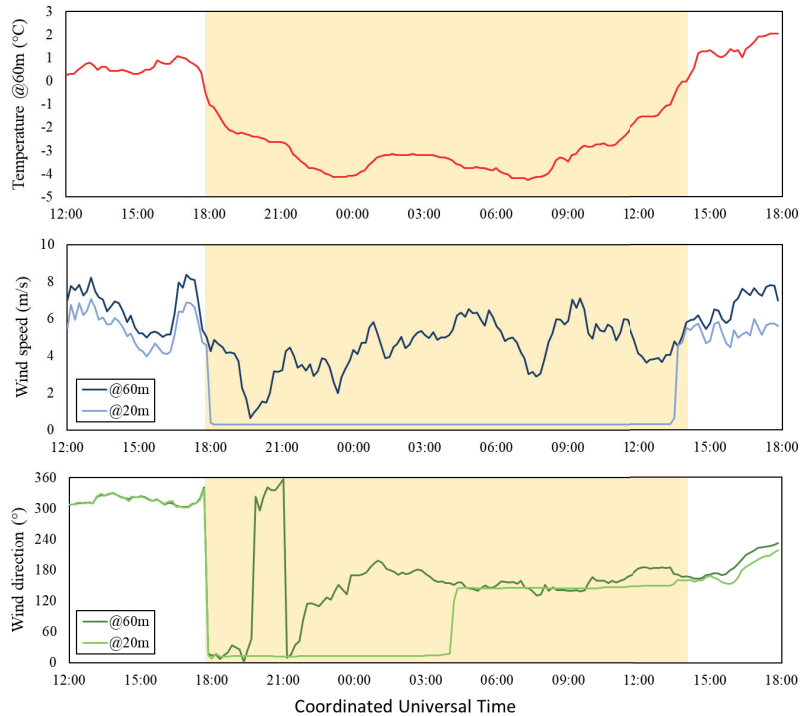


Figure 2.9. Example of an icing event (indicated in yellow). The cup anemometer and the wind vane @20m are affected by icing. Instruments @60m may also be partially affected by icing. Temperature and/or humidity measurements help to identify icing events.

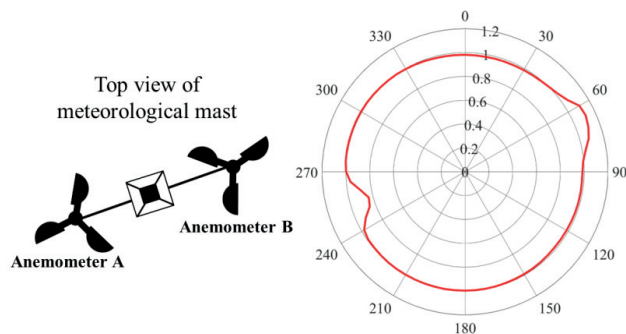


Figure 2.10. Example of tower distortion of measurements. The red line indicates the average ratio between the wind speed measured at anemometers B and A (radial axis) for a given wind direction (polar axis).

The measurement campaign of each site complies with the standards of the International Electrotechnical Commission, Measnet and/or other local standards. Out of the studied sites, Honkajoki is the only one that has measurements in just one location. For this reason,

validations at this site were only possible in the vertical direction. The sites Honkajoki, CM and CA present a high wind shear (Figures 2.2, 2.3 and 2.4), while the sites CL and CK present low wind shear (Figures 2.5 and 2.6). Both conditions are likely to be related to the predominant atmospheric stability conditions at the sites. Among them, Honkajoki and CA are the sites where the wind is the most evenly distributed between the different wind directions (Figures 2.2 and 2.4). The opposite is true for the CL and CK sites, where the wind mostly comes from one wind direction (Figures 2.5 and 2.6).

2.1.2 Digital terrain model

The most important factors that influence the behavior of the local wind flow are related to the terrain conditions. These conditions are represented in the digital terrain model of the site, which consists of a 2-D grid of point values of terrain elevation and roughness length. In forested sites additional information is required, which consist of the location of the forest, canopy height, forest sparsity and tree species. In the WindSim model, this information is used to set certain grid cells of the model as forest by defining them as a semi-permeable obstacle. More details on the forest modelling are provided in Section 2.2.

For the sites of this PhD thesis, the terrain elevation was obtained from the databases of the Shuttle Radar Topography Mission,¹² the Canadian Digital Elevation Data,¹³ the Finish National Land Survey¹⁴ and from LiDAR campaigns conducted by the project owner or commercial providers, like WorldDEM. Roughness length maps are constructed from land cover maps obtained from open databases like the GlobeLand30,¹⁵ the US National Land Cover Database 2001¹⁶ and/or commercial sources. These land cover maps are translated into roughness maps following conversion tables, usually based on the work of Davenport (1960).¹⁷ In the case of the CL and CK sites, a constant roughness value for the entire domain is used instead, as they present a very homogeneous terrain type and more detailed information of the terrain is not available in the aforementioned databases. Further characteristics of the digital terrain models can be found in Papers I, III and IV.

There is a wide variety of terrain complexity among the modeled sites. Honkajoki and CA have a relatively flat terrain (Figures 2.2 and 2.4). CL and PS also present a relatively flat terrain, but with some hilly areas and other terrain features (Figures 2.5 and 2.7). The terrain of the CK

site is relatively even with an overall inclination towards the north (Figure 2.6). By far, the most complex site is CM (Figure 2.3).

2.1.3 Mesoscale simulations

About one-year worth of mesoscale simulations are available for each of the modelled locations. These simulations were produced using the Weather Research Forecasting (WRF) model.¹⁸ Depending on the site, the runs were conducted by the High Performance Computing Center North (HPC2N),¹⁹ Vortex SL²⁰ or one of the co-authors of Paper II (Table 2). Further technical details about the settings of the WRF simulations are provided in Papers I, II and III. The postprocessing of the results was conducted using a time resolution of 1 hr for the outputs. The simulated periods were selected in order to cover the longest concurrent period measured at all observational points at each site.

Table 2. Source of the WRF simulations utilized in the research articles of this thesis.

Site	WRF version	Conducted by
Honkajoki	3.7.1	HPC2N
FINO-1	3.6.1	Co-author in paper
Cabauw	3.6.1	Co-author in paper
CM	3.7.1	Vortex SL
CA	3.7.1	Vortex SL
CL	3.7.1	Vortex SL
CK	3.7.1	Vortex SL
PS	3.7.1	Vortex SL

2.2 WindSim

In this study, the steady-state RANS model that is part of the commercial software WindSim is utilized as a microscale model. The model predicts the spatial perturbations of the wind speed for a given set of boundary conditions. For wind resource assessment applications, it is assumed that the solution of the model is Reynolds number independent, i.e. the spatial wind perturbations are independent of the wind speed. For example, if the model predicts variation of X% in the wind speed between point A and point B, this percentual change is independent of the wind speed at point A. However, wind speed perturbations are still dependent on the direction of the wind, and therefore several simulations with different wind directions are typically conducted to assess a site.

The governing equations of the WindSim's CFD model correspond to the RANS equations,²¹ assuming steady-state (derivatives in time =0) and incompressibility (constant density). All equations in this subsection are given in Einstein notation. Sub-indexes $i, j = 1, 2, 3$ correspond to north, east and vertical components, respectively. Mass conservation is expressed as:

$$\frac{\partial U_i}{\partial x_i} = 0 \quad (1)$$

where U_i and x_i correspond to the i -component of the wind speed vector and of the cartesian coordinate, respectively. The conservation of momentum in the horizontal direction is expressed as:

$$U_j \frac{\partial U_i}{\partial x_j} = -\frac{1}{\rho} \frac{\partial P}{\partial x_i} + \frac{\partial}{\partial x_j} \left(\nu \left(\frac{\partial U_i}{\partial x_j} + \frac{\partial U_j}{\partial x_i} \right) - (\overline{u_i u_j}) \right) \quad i = 1, 2 \quad (2)$$

where P is the pressure, ρ is the air density and ν is the air viscosity. The conservation of momentum in the vertical direction has an additional forcing term when thermal effects (atmospheric stability) are present:

$$U_j \frac{\partial U_3}{\partial x_j} = \frac{\theta_0 - \theta}{\theta_0} g - \frac{1}{\rho} \frac{\partial P}{\partial x_3} + \frac{\partial}{\partial x_j} \left(\nu \left(\frac{\partial U_3}{\partial x_j} + \frac{\partial U_j}{\partial x_3} \right) - (\overline{u_3 u_j}) \right) \quad (3)$$

where g is the gravitational acceleration, θ is the potential temperature and θ_0 its reference value. For neutral simulations $\theta = \theta_0$ and therefore the extra forcing term =0. The potential temperature is influenced by advection, thermal diffusion and turbulent heat transfer, expressed as:

$$U_i \frac{\partial \theta}{\partial x_i} = \frac{\partial}{\partial x_i} \left(\alpha \left(\frac{\partial \theta}{\partial x_i} \right) - (\overline{u_i \theta'}) \right) \quad (4)$$

where α is the kinematic molecular diffusivity for heat in air. The turbulent terms in Equations (2), (3) and (4) are parametrized as:

$$(\overline{u_i u_j}) = -\nu_T \left(\frac{\partial U_i}{\partial x_j} + \frac{\partial U_j}{\partial x_i} \right) + \frac{2}{3} \delta_{i,j} \quad (5)$$

$$(\overline{u_i \theta'}) = \frac{-\nu_T}{\sigma_\theta} \left(\frac{\partial \theta}{\partial x_i} \right) \quad (6)$$

where $\delta_{i,j}$ is the Kronecker delta and $\sigma_\theta (=1)$ is the turbulent Prandtl number for heat transfer. The turbulence viscosity ν_T is obtained from the standard $k - \varepsilon$ turbulence model as formulated by Laufer and Spalding (1974):²²

$$\nu_T = c_\mu \frac{k^2}{\varepsilon} \quad (7)$$

$$\frac{\partial(U_i k)}{\partial x_i} = \frac{\partial}{\partial x_i} \left(\frac{\nu_T}{\sigma_k} \frac{\partial k}{\partial x_i} \right) + P_k + P_b - \varepsilon \quad (8)$$

$$\frac{\partial(U_i \varepsilon)}{\partial x_i} = \frac{\partial}{\partial x_i} \left(\frac{\nu_T}{\sigma_\varepsilon} \frac{\partial \varepsilon}{\partial x_i} \right) + c_{\varepsilon 1} \frac{\varepsilon}{k} (P_k + c_{\varepsilon 3} P_b) - c_{\varepsilon 2} \frac{\varepsilon^2}{k} \quad (9)$$

$$P_k = \nu_T \left(\frac{\partial U_i}{\partial x_j} + \frac{\partial U_j}{\partial x_i} \right) \frac{\partial U_i}{\partial x_j} \quad (10)$$

$$P_b = -\frac{\nu_T}{\sigma_\theta} g \frac{1}{\theta} \frac{\partial \theta}{\partial x_3} \quad (11)$$

Here k corresponds to the turbulent kinetic energy (TKE) and ε to its dissipation rate (EDR). The values of the model constants c_μ , σ_k , σ_ε , $c_{\varepsilon 1}$, $c_{\varepsilon 2}$ and $c_{\varepsilon 3}$ are presented in Table 3. The term P_b is used in Equation (8) when thermal effects are present, otherwise $P_b = 0$.

Table 3. Values of the model constants of the standard $k - \varepsilon$ turbulence model used by Laufer and Spalding (1974).²³

c_μ	σ_k	σ_ε	$c_{\varepsilon 1}$	$c_{\varepsilon 2}$	$c_{\varepsilon 3}$
0.09	1.0	1.3	1.44	1.92	1.0

Since the potential temperature gradients in coupled simulations can be much more stably stratified than the analytical formulations, some limits were introduced to the values of P_b . In order to prevent too low turbulence in very stable conditions, P_b is limited in Equation (8) by $P_b = \max(-Rf_c P_k, P_b)$, where $Rf_c = 1 - c_{\varepsilon 1}/c_{\varepsilon 3} = 0.25$.²⁴ On the other hand, P_b is limited in Equation (9) by $P_b = \max(0, P_b)$.²⁵ These limits were used introduced Paper III and also used in Paper IV. Further justification of this addition is provided in Paper III.

In WindSim, forest is modelled by defining the grid-cells where it is located as a porous media. Therefore, source/sink terms S_j , S_k and S_ε are added at the right side of the governing equations of momentum (Equation (2) and (3)), TKE (Equation (8)) and EDR (Equation (9)), respectively. These terms are parametrized as:²⁶

$$S_j = -\rho C_d \sqrt{U_i U_i} U_j \quad (12)$$

$$S_k = C_d \left(\beta_p \sqrt{U_i} U_i^3 - \beta_d U_i k \right) \quad (13)$$

$$S_\varepsilon = C_d \left(c_{\varepsilon 4} \beta_p \frac{\varepsilon}{k} U_i^3 - c_{\varepsilon 5} \beta_d U_i \varepsilon \right) \quad (14)$$

where C_d is the drag coefficient of the forest and β_p , β_d , $c_{\varepsilon 4}$, and $c_{\varepsilon 5}$ are model constants, whose values are shown in Table 4. C_d values are chosen for each grid-cell defined as forest, depending on tree sparsity, tree species and the geographical location of the forest.

Table 4. Values of the forest constants according to the formulations of Sanz (2003)²⁷ using the model constants in Table 3.

β_p	β_d	$c_{\varepsilon 4}$	$c_{\varepsilon 5}$
1	6.51	1.24	1.24

2.3 Meso-microscale coupling procedure

The meso-microscale coupling procedure consists of two steps. First, a set of mesoscale fields that are representative of the predominant wind conditions at the site are obtained. Secondly, these representative mesoscale fields are transferred into the microscale model as boundary conditions. Paper II is focused only on the first step, while the other papers deal with both. Details about the procedures utilized at each step are provided in the following sections.

2.3.1 Computation of representative mesoscale fields

In this PhD thesis, two methodologies were proposed to obtain representative mesoscale fields. One consists of averaging the wind conditions per directional sector, while the other obtains these conditions in an automated fashion utilizing neural networks. The first approach is regarded as a simple method that resembles the normal modeling approach used in the wind industry (one simulation per directional sector). The second method requires a further understanding of the abstraction done by the neural map. Nevertheless, it provides a powerful tool to easily explore the wind conditions that occur in a site in a comprehensive manner.

A common procedure for both methodologies is to filter timesteps that have an average wind speed below 3 m/s, for all grid points between 50 and 150 m a.g.l. and that lie within the microscale domain. This way, all mesoscale timesteps that are not of interest for wind energy generation are filtered out. The variables of interest of the obtained mesoscale fields are U_i ($i = 1, 2, 3$), θ and the planetary boundary layer height.

2.3.1.1 Directional average

The first methodology proposed in this study consists in averaging all timesteps of the mesoscale simulation timeseries according to their wind direction. This procedure generates one representative wind condition per desired wind direction. The approach implicitly assumes that the wind conditions for a given wind direction are relatively similar in time. This assumption holds true in many wind energy projects, especially at sites where the wind rose is well spread across wind directions or if the site is strongly influenced by sea-land or mountain-valley winds.^{28,29} In any case, this assumption is also made when running a standalone microscale model. Therefore, the use of this methodology does not present additional assumptions with respect to the normal application of the microscale model in wind resource assessment. It is expected that by downscaling the obtained mesoscale fields, the wind flow solution will be better for wind directions strongly influenced by mesoscale circulations (Figure 2.11).

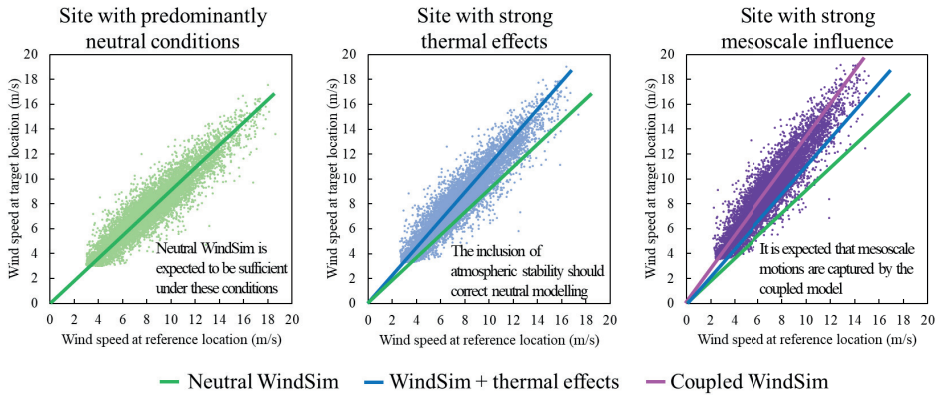


Figure 2.11. Expected application of different microscale modelling approaches. The dots correspond to onsite measurements and the lines to the prediction of the model.

Further technical details on the averaging procedure are provided in Papers I and III. The differences between the procedures used in those papers are presented here. In Paper I, the mesoscale fields of θ are directly averaged, while in Paper III the values of θ_0 and $\Delta\theta = \theta - \theta_0$ are separately averaged instead. Then, the average field of θ is calculated as $\bar{\theta} = \overline{\Delta\theta} + \bar{\theta}_0$. This second approach better captures the average atmospheric stability condition (contained in $\Delta\theta$) as it is not distorted by its absolute value. On the other hand, the mesoscale fields in Paper I are classified by their atmospheric stability in addition to the wind direction. Due to the small gain in model performance compared to the extra use of computational resources, as well as

difficulties in classifying onsite measurements by atmospheric stability, the method was not pursued in Paper III. A final difference is that in Paper III an additional coupling approach was introduced, which consists in filtering the θ mesoscale fields. In the same paper this approach is compared with coupled models without temperature filtering and without using the temperature fields at all.

2.3.1.2 Two-level SOM clustering

The second methodology proposed in this PhD to obtain representative mesoscale fields is based on a self-organizing map (SOM).³⁰ A SOM is a grid of interconnected nodes that are positioned in the space of the input data (Figure 2.12). The positions of the SOM nodes are iteratively modified in such a manner that the nodes are transferred closer to locations with a high density of input data points and further away from data-sparse areas (Figure 2.12c). This procedure is called training and it is repeated up to a prescribed number of iterations. Once the SOM is trained, it is possible to visualize the clustering structures of the data by plotting the distance between each node and its neighbors (Figure 2.12d).

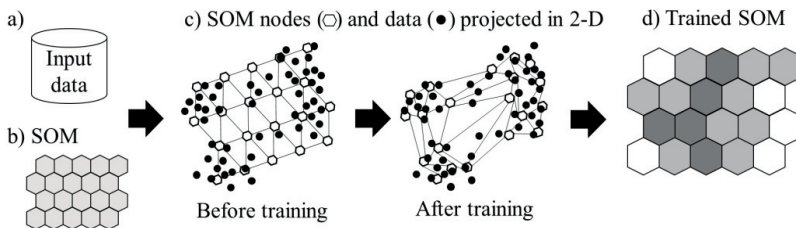


Figure 2.12. Example of the SOM training procedure with a dataset with 20 nodes and three clusters. Darker (lighter) shading in the SOM before (b) and after (d) training represents longer (shorter) distances between the node and its neighbors. Reproduced from Paper II.

As commented in the literature survey conducted in Paper II, most of the studies in meteorology that use SOM, directly use the nodes as a clustering solution. Nevertheless, such an approach presents certain problems. First of all, there is a practical constraint regarding the possible number of obtainable clusters, as the SOM can only be composed of a non-prime number of nodes. Additionally, neighboring nodes portray similar characteristics and therefore redundant patterns would be obtained. A more conceptual problem of this approach, as pointed out by Wu & Chow (2004),³¹ is that the purpose of a SOM is to extract and visually display the structure of the input data, while clustering is to partition the input data into groups. The

previously mentioned studies that directly use the nodes to cluster seem to mix these two objectives.

An important feature of SOMs is that the map preserves topological ordering. In other words, the nodes that are located close to each other share certain traits. For the context of this study, this implies that neighboring nodes share similar wind speed, wind shear, temperature shear and/or other characteristics (see for example Figure 2.13). This feature facilitates the characterization and understanding of the different conditions that occur in a site. By plotting different variables, it is possible to find relations (typically non-linear) among the different variables. For example, in Figure 2.13 it is possible to visually relate the speed and direction of the wind with the atmospheric stability conditions at the site.

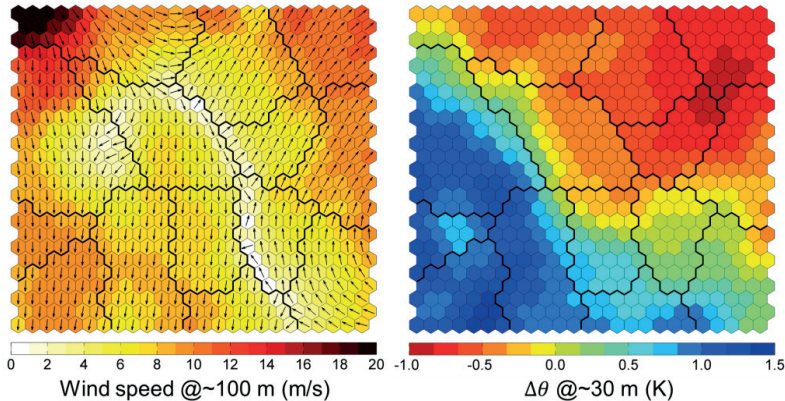


Figure 2.13. Representative wind speed (left) and $\Delta\theta$ (right) values of the nodes of a SOM of dimensions 25×25 used to classify WRF-simulated 3-D mesoscale fields at CK. The wind direction in the left panel is indicated by black arrows. The SOM partition is indicated by black lines. Adapted from Paper IV.

In order to use the SOM for clustering purposes, a two-level SOM clustering (SOM2L)³² approach is utilized. The SOM2L consists of partitioning (i.e. clustering) the nodes of the SOM (as illustrated in Figure 2.13). Several clustering techniques can be used for this stage, like k -means or hierarchical clustering. The disadvantage of using these techniques is that the total number of clusters has to be prescribed a priori. Therefore, in this study it has been opted instead for a methodology that exploits the topological ordering of the SOM. Specifically, the cluster centers are defined as the local minima of the distance between each node and its neighbors (Figure 2.14).³³ The remainder of the SOM nodes are then assigned to a cluster following Ward's criterion.³⁴

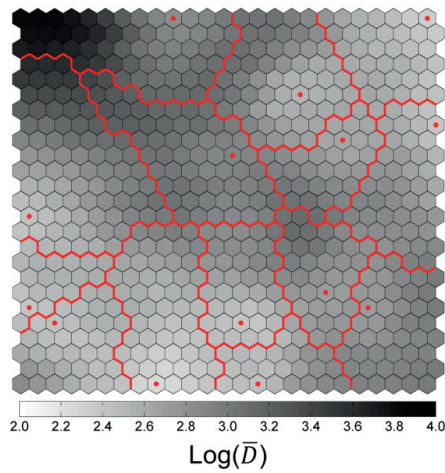


Figure 2.14. Partition of the SOM based on the local minima of \bar{D} . The local minima are indicated by the red dots and the partitions by the red lines. \bar{D} corresponds to the average distance between a node and its neighbors. Reproduced from Paper IV.

As a result, the application of the SOM2L methodology to the mesoscale simulations provides a set of mesoscale patterns. If the input data correspond to 3-D mesoscale fields (as in Paper IV), these patterns represent a variety of the predominant wind conditions at the site. In contrast to the method that uses the directional averages explained in section 2.3.1.1, the patterns obtained with the SOM2L can yield several wind conditions for the same wind direction (Figure 2.15). Moreover, very infrequent wind directions will not be found in the extracted patterns. Further technical details of the parameters used in the SOM2L are provided in Paper II and IV. Detailed justification of the selection of these parameters are provided in Paper II and the references therein. As argued by Vesanto and Sulkava (2002),³³ the distance map “may have some local minima which are a product of random variations in the data”. In order to prevent this, in Paper IV a smoothing function is applied to the distance map before computing the local minima.

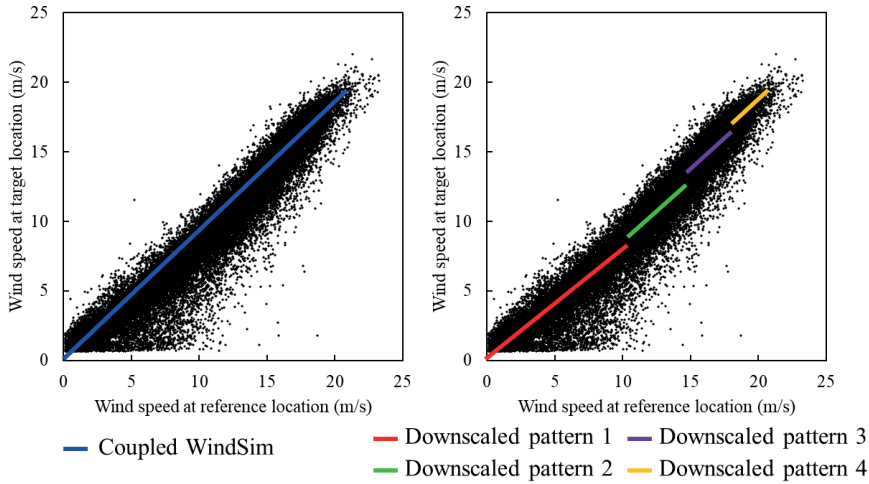


Figure 2.15. Conceptual comparison between the directional average coupling of section 2.3.1.1 (left) and the SOML2 coupling (right) for one directional sector. The dots correspond to onsite measurements and the lines to the prediction of the model.

2.3.2 Transferring of mesoscale fields to the microscale model

Once representative mesoscale fields are obtained, they are transferred into the microscale model as boundary conditions. There are six variables that are prescribed as boundary conditions: U_1 , U_2 , U_3 , θ , k and ε . The values of U_1 , U_2 , U_3 and θ are computed by interpolating the mesoscale values onto the microscale grid. Vertical interpolations are first conducted utilizing the cubic spline method. Then, horizontal bilinear interpolations are conducted. If the interpolations are conducted in the inverse order (horizontal first, vertical second) the interpolated values might have some discontinuities, especially close to the ground.

The lowest vertical level of the WRF simulations results are typically located at approximately 10 m above the ground. It is very common that a few grid points of the microscale model are located below this height. Therefore, the WRF values of U_1 , U_2 and θ are extrapolated using Monin-Obukhov similarity theory equations⁸ with the two lowest vertical levels of the WRF domain, located at ~ 10 m and ~ 30 m. To compute the necessary parameters like the Monin-Obukhov length or the friction velocity, the gradient method³⁵ is utilized. In few occasions, this method is not applicable because of very low winds speeds and/or very high temperature gradients.³⁶ In these cases, the values are obtained from the average of the surrounding grid points. The values of vertical wind speed are simple prescribed as $U_3 = 0$.

The values of k and ε are computed using the analytical formulas derived by Han et al. (2000).³⁷ These formulas are also based in the Monin-Obukhov similarity theory. Most of the parameters required to apply these formulas are the same as the ones utilized in the extrapolations. In addition, the planetary boundary layer (PBL) height values transferred from the mesoscale are utilized. These values are obtained by horizontally interpolating the PBL height from the mesoscale simulations.

Further technical details of the interpolation and extrapolation procedures, as well as on the computation of k and ε are provided in Paper I. In Papers III and IV, the methods to compute the values are very similar. The only difference is that in Paper I the θ values are interpolated with respect to the height above ground level (a.g.l.), while in Papers III and IV they are interpolated with respect to the height above sea level (a.s.l.). As shown in Figure 2.16 the approach used to interpolate θ has an important impact in its vertical structure. It is important to preserve the PBL height transferred from the mesoscale (implicitly in the contained in the θ field) since the top of the PBL blocks the vertical motion of the flow. The site used in Paper I (Honkajoki) is very flat and therefore the θ field is barely distorted. In Paper III, most of the sites have a more complex terrain than Honkajoki, which made necessary to introduce this improvement in the interpolation procedure.

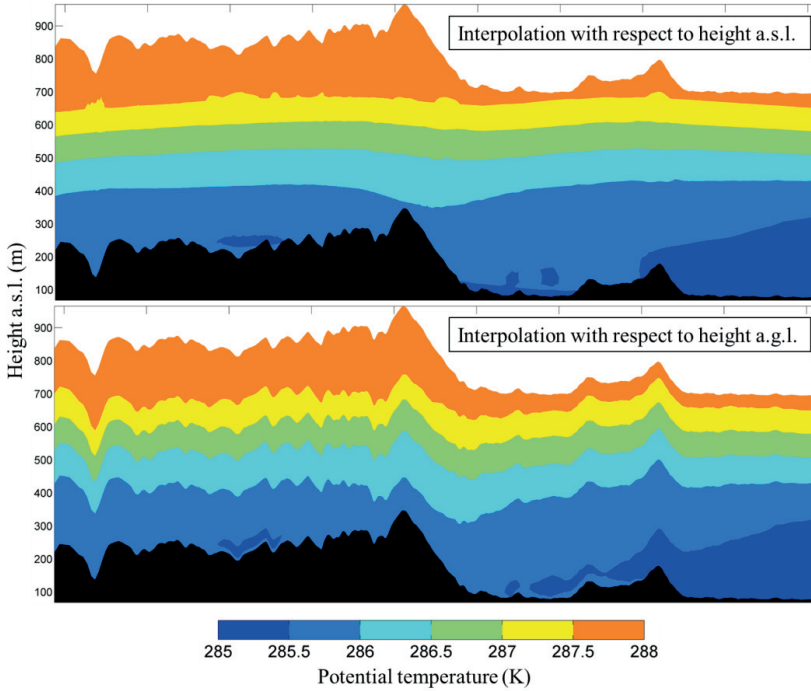


Figure 2.16. Comparison of vertical planes of potential temperature for different interpolation procedures.

2.4 Validation metric

As mentioned in Section 1.1, the purpose of the wind flow simulations in wind resource assessment is to extrapolate the wind measurements. These extrapolations consist in obtaining the wind speed at a target location T (typically a wind turbine) by multiplying the measured wind speed at a reference point R by a factor (Figure 2.17b). This factor is called the speed-up ratio SU , and it is calculated as:

$$SU(R, T) = \frac{u_T}{u_R} \quad (15)$$

where u_R and u_T are the modeled wind speeds at points R and T (Figure 2.17a). Therefore, the performance of a model is quantitatively evaluated by comparing the modeled SU with the measured one, between selected pairs of measurements. Specifically, the mean values of SU and wind speeds are utilized to calculate the so-called crosscheck prediction XPE as:

$$XPE(R, T) = \frac{\overline{SU(R, T)} \times \overline{u_R} - \overline{u_T}}{\overline{u_T}} \quad (16)$$

It is possible to calculate one *XPE* per pair of measurement points. The specific error metrics utilized in Papers III and IV are based on the *XPE* values. These metrics were utilized in these research articles to facilitate the discussion of extrapolation errors when several reference and target points are evaluated simultaneously. For further technical details, the reader is referred to those articles.

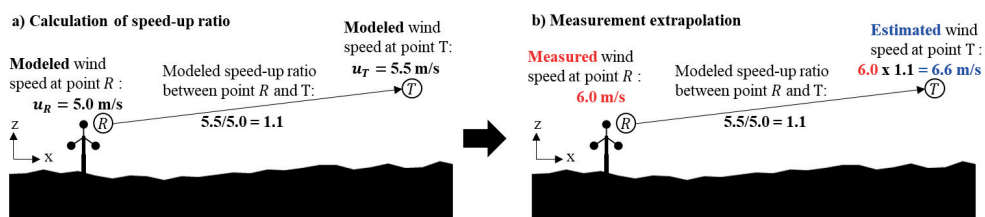


Figure 2.17. Example of the calculation of the speed-up ratio (a) and measurement extrapolation (b). Adapted from Paper I.

Summary of main results

In this chapter, the main results of this PhD thesis are presented. The findings can be ordered in three categories: (i) capabilities of the SOM2L classification, (ii) capabilities of coupled simulations and (iii) validation results of the meso-microscale coupling methodologies. Findings (i) focuses only in the strengths of the proposed classification, independent of the application. Findings (ii) and (iii) are related qualitatively and quantitatively results to the simulations of the coupled models.

3.1 Capabilities of the SOM2L classification

The SOM2L methodology proposed in Paper II provides in a fully automated manner the predominant patterns in the input data. In Paper II, the methodology was capable of finding wind speed profiles of various shapes. Some of these shapes correspond to well-known profiles, such as high shear, low shear or low-level jets. It was found that some of the obtained profiles had similar shape as the ones manually obtained in a observational study by Peña et al. (2014)³⁸, as shown in Figure 3.1. It is clear that the use of the SOM2L approach can be a better alternative to a more arduous manual approach.

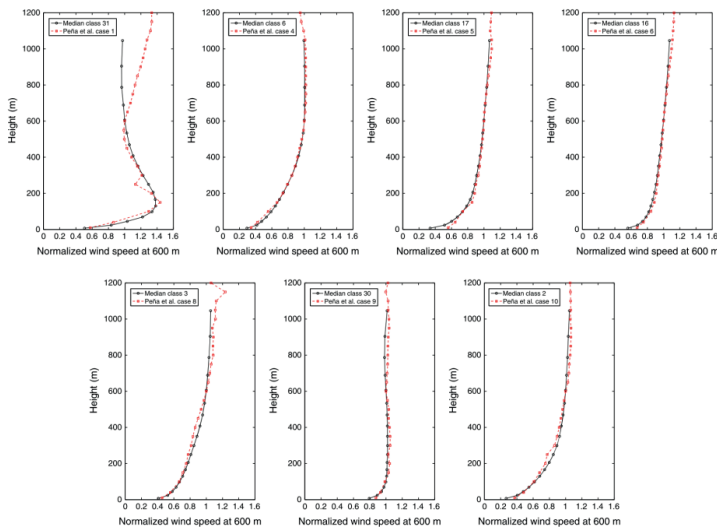


Figure 3.1. Comparison of a few wind speed vertical profiles reported by Peña et al. (2014)³⁸ against the SOM2L-based results. Reproduced from Paper II.

In Paper IV, the SOM2L is applied to the 3-D mesoscale fields simulated for the CK site. The SOM2L clearly provides distinctive patterns, regarding wind speed, wind direction and atmospheric stability. The methodology allows for an easy characterization of these patterns. In particular for this site, relationships regarding wind direction, atmospheric stability, wind shear, time of the day and season were effortlessly explored due to the ordering provided by the SOM. Furthermore, a total number of 14 patterns were found, which is adequate for the computational resources typically available in the industry for downscaling purposes.

3.2 Capabilities of coupled simulations to downscale mesoscale patterns

Mesoscale models can reproduce some wind patterns that are not possible to obtain when utilizing a standalone microscale model. For some of the representative mesoscale fields, the coupled models are capable to downscale such mesoscale patterns. As shown in Figure 3.2, the overall mesoscale pattern is sustained in the microscale domain. However, the wind flow is modified by the microscale model by including the influence of finer terrain features in the local wind flow. As discussed in Paper III, the microscale model includes the influence of the mesoscale model in a better way in complex terrain, when the thermal effects are considered.

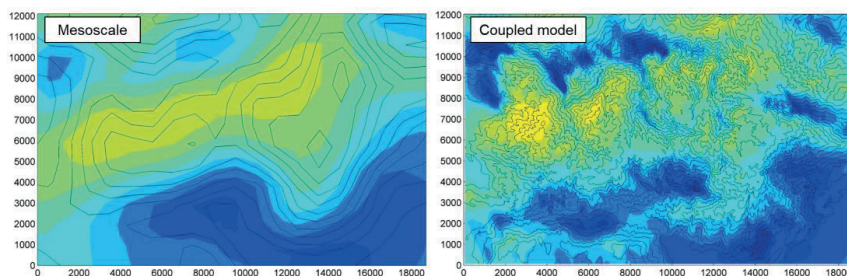


Figure 3.2. Horizontal planes of wind speed @ $\sim 100^\circ$ at the CM site for mesoscale (left) and coupled (right) simulations. The black lines in the map correspond to the contour lines of terrain elevation for every 50 m. Adapted from Paper III.

Some wind patterns that are of interest for the wind energy community, namely strong wind turning and low-level jets, were reproduced by the WRF simulations. The coupled simulations are able to downscale these patterns into the microscale. As reported in Paper III, these patterns are very different from the ones obtained when using analytical profiles. In the case of the wind turning (Figure 3.3), the standalone microscale simulation does not present a turning at all. The same is true in the case of the low-level jets (Figure 3.4), as analytical formulations follow

logarithmic shapes. For both patterns it was found that the use of atmospheric stability is necessary to maintain the wind turning and the low-level jet shape.

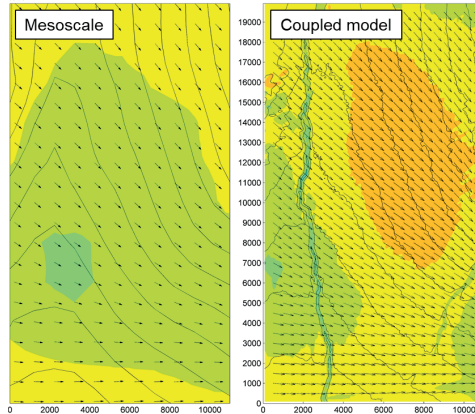


Figure 3.3. Horizontal planes of wind speed @ ~100 m from sector 300° at the CK site for mesoscale (left) and coupled (right) simulations. The black arrows indicate the direction of the wind. The black lines in the map correspond to the contour lines of terrain elevation for every 50 m. Adapted from Paper III.

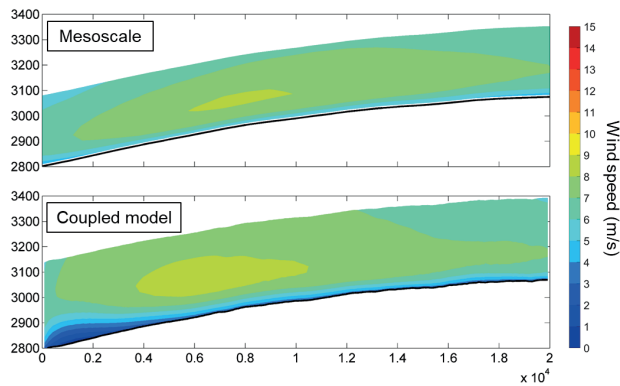


Figure 3.4. Vertical planes of wind speed from sector 0° at the CK site for mesoscale (left) and coupled (right) simulations. The black line corresponds to the digital terrain height. Adapted from Paper III.

3.3 Validation results

In this section the meso-microscale coupling results are evaluated. As mentioned in Section 1.1, the wind flow models are utilized to extrapolate onsite measurements. Therefore, the performance of the models is compared with respect to their capability to accurately do such extrapolations. The comparisons are conducted by using the crosscheck prediction errors explained in Section 2.4. This error metric is obtained by extrapolating a measurement to the location of another measurement and comparing the prediction against the observed values.

Further technical details of the meso-microscale coupling results using the mesoscale fields obtained from the directional average and from the SOM2L, can be found in the Papers III and IV, respectively.

3.3.1 Meso-microscale coupling using directional average

In Figure 3.5, the coupled models that utilize the directionally averaged mesoscale fields are compared against the mesoscale and the standalone microscale simulations. For vertical extrapolations, the coupled simulations have for most sectors smaller errors than the mesoscale or standalone simulations. Improvements of the coupled results respect to the mesoscale results, are mainly due to a better accounting of the influence of the finer features in the terrain. This is more evidently when comparing the results of the CM site, which is very complex. Moreover, in CA, where the terrain is very flat, the differences are rather small and actually mesoscale simulations perform slightly better as the wind profile is mostly influenced by the weather conditions rather than the terrain. Differences between coupled and standalone simulations are in general lower, as the latter uses analytical profiles whose parameters were adapted to the observed profiles. Nevertheless, there are important differences in the performance at some sectors. The source of these differences is the limitation of the analytical boundary conditions to reproduce non-analytical shapes. For example, very stable conditions present at CA were, as expected, associated with very high wind shear. This shear is well reproduced in the standalone simulation close to the ground. Nevertheless, it fails in reproducing very fast vertical changes of shear that are observed at the site as they do not follow an analytical shape. In the case of the CL site, very low shear profiles are observed due to the presence of wide low-level jets that are not possible to capture in the standalone simulations.

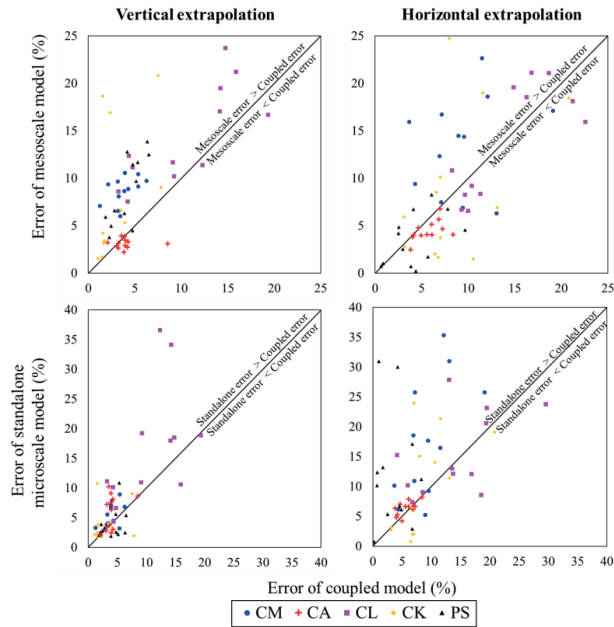


Figure 3.5. Comparison of crosscheck prediction errors between the mesoscale and coupled simulations (top panels), and standalone and coupled simulations (bottom panels). Adapted from Paper III.

For horizontal extrapolations in complex terrain (e.g. CM site), the coupled model performs better than the mesoscale and standalone simulations. This indicates that to properly model such sites it is not only sufficient to utilize models with finer resolution, but also with the adequate stability conditions. In the case of the very flat and very stable sites (e.g. CA site), it is better not to couple the potential temperature and run with neutral stratification instead. As discussed in Paper III, the inclusion of the atmospheric stability under these conditions results in too low turbulence in the microscale model to transfer the momentum downwards. At the remainder of the studied sites, the relative performance of the mesoscale and coupled simulations are very dependent on the wind direction. If the wind is perturbed by even small obstacles like small valleys, rivers, ridges or small hills, the coupled simulations tend to perform better. It must be noted that even when the mesoscale and coupled errors are similar, the latter have much finer features in the wind flow due to their higher resolution. Similar as with the vertical extrapolation, the coupled models perform better than the standalone simulation for most sectors, independent of the terrain or stability conditions. Depending on the sector, these differences are product of improved stability conditions in the standalone model (due to limited information) or due to the influence of mesoscale patterns that are significantly different to the analytical formulations.

3.3.2 Meso-microscale coupling using SOM2L patterns

Similar to the results in Section 3.3.1, most of the extracted patterns by the SOM2L are significantly modified by the microscale model. The main factors for these modifications are the finer terrain features included in the microscale model as well as the propagation of the wind conditions at the inlets into the domain. For most patterns with stable atmospheric conditions (patterns 1, 2, 4 and 8; see Figure 3.6), the microscale model reduces the error significantly, ranging from 4 to 15 % in error reduction (Figure 3.7). For most patterns with unstable atmospheric conditions (patterns 5, 9, 11 and 13) the microscale simulation performs worse than the mesoscale one, with an error increase between 3 to 7 %. A similar trend is observed for the neutral simulations, where the most stably stratified (pattern 12) has an error reduction of 2% and the most unstably stratified (patterns 6 and 10) have an error increase of 7% and 4% after downscaling, respectively. Overall, the error is reduced by 2.7% when using the downscaling procedure.

The mesoscale and microscale simulations of the SOM2L patterns produce very similar vertical profiles of wind speed. In addition, for most patterns both simulations reproduce well the measured winds speed profiles. For patterns with unstable atmospheric conditions (patterns 5, 9, 11, 13 and 14), the wind speeds profiles are particularly well reproduced. For patterns 4, 7 and 8, none of the models is able to reproduce the negative shear observed at the measurements. These deviations are due to the inability of the WRF model to reproduce the height of the jet for these patterns, a defect that is transferred to the microscale model. In the case of the pattern 3, the jet height is well reproduced and therefore is also correct in the microscale.

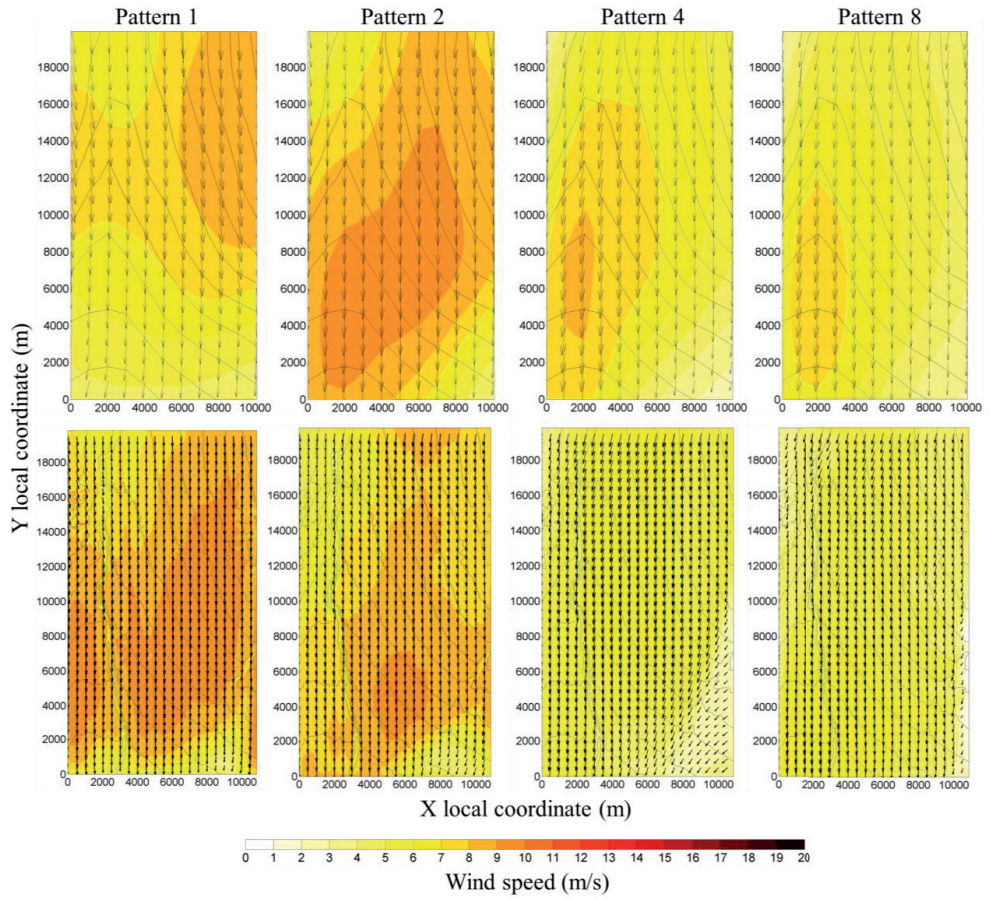


Figure 3.6. Extracted (top row) and downscaled (bottom row) patterns 1, 2, 4 and 8. The wind direction is indicated by the black arrows. Adapted from Paper IV.

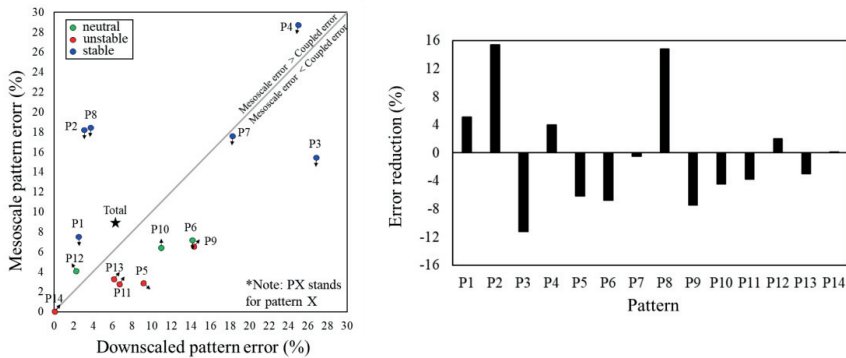


Figure 3.7. Left panel: Comparison of the crosscheck prediction errors between the mesoscale and downscaled patterns. The arrow and color of each circle indicate the wind direction and the atmospheric stability condition of the pattern, respectively. Right panel: Crosscheck prediction error reduction after downscaling the patterns. Reproduced from Paper IV.

Conclusions and further work

Two methodologies have been proposed for the coupling of mesoscale simulations with steady-state CFD microscale model. The first methodology utilizes the average values of the variables of interest per directional sector. Such a methodology is an easy way to produce more realistic boundary conditions for the microscale model. However, in some cases the averaged values of different weather conditions do not provide a good representation of the mean state of the atmosphere. The second proposed methodology derives predominant weather patterns utilizing a two-level self-organizing map clustering technique. This clustering technique fully automates the obtention of the mesoscale patterns and splits them according to their characteristics. Compared to the previous method, the loss of information is much lower as the averaging of values is conducted over similar mesoscale fields. This methodology is also able to deal with sites with different weather conditions despite of having similar wind directions.

Further remarks of the research conducted in this thesis are provided in the following paragraphs. In addition, recommendations for further research are provided for each topic.

4.1 Coupled models for wind resource assessment

Coupled simulations reproduce better the observed profiles compared to standalone simulations, if the shape of the profiles does not follow analytical formulations. Otherwise, the difference between the models is rather low. However, vertical validations in this study (and in general) are rarely conducted for heights higher than 150 m. For these heights, the coupled simulations present more realistic wind shear compared to the standalone simulations as the analytical formations (which are based on Monin-Obukhov similarity theory) are usually not valid anymore. This is important to consider in wind resource assessment as wind turbines get higher and higher. Coupled simulations tend to better reproduce the profiles at higher heights because of the information about the wind shear provided by the mesoscale model. However, the coupled models also perform better than the mesoscale model in vertical extrapolations because the latter are not able to properly take into account the influence of the surface on the lower part of the profiles.

For horizontal extrapolations, the use of coupled models performs better compared to mesoscale or standalone microscale models. In the case mesoscale models, the coupled models

are simple more beneficial due to their higher resolution. In the case of microscale simulations, the coupled models have the advantage of a proper stability effects without the need of tweaking the stability conditions. Furthermore, make use of spatial distribution of the atmospheric stability in the site. This appears to be as important as using a finer resolution. which is of big importance for a proper modelling in complex terrain. Even if mesoscale simulations perform similar than the coupled model in terms of errors (typically at relatively flat terrain), the coupled model is able to include finer features in the wind flow, like rivers or forest clearings. This makes the coupled approach more advantageous for the micro-siting of the wind turbines.

For very stable conditions at flat sites, the coupled model is not capable to perform well in both vertical and horizontal extrapolations, simultaneously. Vertical extrapolations are better than any of the other models when thermal effects are considered. For horizontal extrapolations, the mesoscale and coupled models where similar, if in the latter neutral stratification is considered. When stable stratification is used instead, there is not sufficient turbulence in the microscale model to transfer momentum downwards. For very stable conditions, the wind has a quasi-laminar behavior, while turbulence models like the k- ϵ standard model are designed for turbulent flow. In order to enable the use of steady-state CFD models for meso-microscale coupling, it is recommended to further research modelling alternatives or modifications to RANS. This may include the addition of forcing terms based on observational data (nudging).

The validation study carried out through this work can be extended to other problems in wind resource assessment, like assessing the sensitivity of the energy yield and/or wind farm layout due to the use of mesoscale, standalone or coupled approaches. Moreover, it is recommended to further investigate and validate the turbulence intensity simulated by these set-ups. The turbulence intensity is key for site suitability studies of the wind turbines, which is important for wind energy project developers as well as for wind turbine manufacturers.

4.2 Two-level self-organizing map clustering methodology

The two-level self-organizing map technique proposed in this PhD thesis can in an objective manner extract the predominant wind patterns from a dataset. The methodology does not require any a priori prescription of cluster size and prevents the use of excessively large number of clusters by reducing redundant classes. The self-organizing map allows for the analysis of

how the extracted patterns evolve with respect to time and space, and therefore associate them with underlying atmospheric phenomena or processes. The SOM2L has a lot of potential for different applications in wind energy. Below, some possible applications are listed:

- i. With use concepts from the field of symbolic dynamics, it would be possible to study the evolution of certain wind patterns. Predominant sequences of patterns can be then be identified to be downscaled
- ii. Classification of onsite measurements to explore the different conditions monitored by the instruments
- iii. The patterns extracted from measured or simulated datasets can be used as states in Markov chains (or similar) for data reconstruction or for the generation of a typical year
- iv. Wind energy forecasting frameworks

The applications listed above are only tentative and they require further research to be properly implemented.

4.3 Potential of coupled models using SOM2L

For the studied site in Paper IV, the meso-microscale coupling framework utilizing SOM2L improves the wind estimations compared with the use of the mesoscale model. Nevertheless, the microscale model is not able to properly downscale some of the obtained wind conditions. The reason is that the microscale model is only able to provide information from the inlets into the domain. Therefore, any pattern that is located within the domain and not “seen” at the inlets is not kept in the microscale simulation. In general, the weather conditions at the studied site were rather extreme (from very stable to very unstable stratification). Further validation of the methodology is required for simpler weather conditions as well as for more complex terrain.

Assuming that it is possible to properly downscale the extracted patterns by the SOM2L, the proposed framework has a lot of potential for wind turbine wake simulations. In order to resolve the turbine wake in a steady-state CFD model, different wind speeds for the same wind direction must be simulated. This increase the number of total simulations dramatically, even more if different atmospheric stability classes must be taken into account. With the SOM2L, infrequent combinations can be skipped, and only simulate the predominant ones.

References

1. Intergovernmental Panel on Climate Change. *Climate Change 2014 Mitigation of Climate Change*. (Cambridge University Press, 2014). doi:10.1017/CBO9781107415416.
2. GWEC. Global Wind Report 2015. 75 (2016).
3. Stehly, T., Beiter, P., Heimiller, D. & Scott, G. *2017 Cost of Wind Energy Review*. (2018).
4. Jackson, P. S. & Hunt, J. C. R. Turbulent wind flow over a low hill. *Q. J. R. Meteorol. Soc.* **101**, 929–955 (1975).
5. Yamaguchi, A., Ishihara, T. & Fujino, Y. Applicability of Linear and Nonlinear Wind Prediction Models To Wind Flow in Complex Terrain. in *The World Wind Energy Conference and Exhibition* (2002).
6. Sanz Rodrigo, J. *et al.* Mesoscale to microscale wind farm flow modeling and evaluation. *Wiley Interdiscip. Rev. Energy Environ.* **6**, (2017).
7. Hristov, Y., Oxley, G. & Žagar, M. Improvement of AEP Predictions Using Diurnal CFD Modelling with Site-Specific Stability Weightings Provided from Mesoscale Simulation. *J. Phys. Conf. Ser.* **524**, 012116 (2014).
8. Monin, A. S. & Obukhov, A. M. Basic laws of turbulent mixing in the surface layer of the atmosphere. *Contrib. Geophys. Inst. Acad. Sci. USSR* **24**, 163–187 (1954).
9. New European Wind Atlas. www.neweuropeanwindatlas.eu.
10. Dutch Offshore Wind Atlas. <https://www.dutchoffshorewindatlas.nl/>.
11. Jothiprakasam, V. D. Downscaling wind energy resource from mesoscale to local scale by nesting and data assimilation with a CFD model. 183 (2014).
12. Farr, T. G. *et al.* The Shuttle Radar Topography Mission. *Rev. Geophys.* **45**, RG2004 (2007).
13. Canadian Digital Elevation Model. <https://open.canada.ca/data/en/dataset/7f245e4d-76c2-4caa-951a-45d1d2051333>.
14. National Land Survey of Finland. <https://www.maanmittauslaitos.fi/en>.
15. Jun, C., Ban, Y. & Li, S. Open access to Earth land-cover map. *Nature* **514**, 434–434 (2014).
16. Wickham, J. *et al.* The Multi-Resolution Land Characteristics (MRLC) Consortium — 20 Years of Development and Integration of USA National Land Cover Data. *Remote Sens.* **6**, 7424–7441 (2014).

References

17. Davenport, A. Rationale for determining design wind velocities. *Trans. Am. Soc. Civ. Eng.* **126**, (1960).
18. Skamarock, W. C. *et al.* A Description of the Advanced Research WRF Version 3. *Tech. Rep.* 113 (2008) doi:10.5065/D6DZ069T.
19. High Performance Computing Center North. <https://www.hpc2n.umu.se/>.
20. Vortex webpage. <https://vortexfd.com/>.
21. Reynolds, O. On the Dynamical Theory of Incompressible Viscous Fluids and the Determination of the Criterion. *Philos. Trans. R. Soc. A Math. Phys. Eng. Sci.* **186**, 123–164 (1895).
22. Launder, B. E. & Spalding, D. B. The numerical computation of turbulent flows. *Comput. Methods Appl. Mech. Eng.* **3**, 269–289 (1974).
23. Launder, B. E. & Spalding, D. B. The numerical computation of turbulent flows. *Comput. Methods Appl. Mech. Eng.* **3**, 269–289 (1974).
24. Duynkerke, P. G. Application of the E – ϵ Turbulence Closure Model to the Neutral and Stable Atmospheric Boundary Layer. *J. Atmos. Sci.* **45**, 865–880 (1988).
25. Duynkerke, P. G. & Driedonks, A. G. M. A Model for the Turbulent Structure of the Stratocumulus–Topped Atmospheric Boundary Layer. *J. Atmos. Sci.* **44**, 43–64 (1987).
26. Green, S. R. Modelling Turbulent Air Flow in a Stand of Widely-Spaced Trees. *PHOENICS J. Comput. Fluid Dyn. its Appl.* 294–312 (1992).
27. Sanz, C. A Note on k - ϵ Modelling of Vegetation Canopy Air-Flows. *Boundary-Layer Meteorol.* **108**, 191–197 (2003).
28. Zhong, S. & Takle, E. S. An Observational Study of Sea- and Land-Breeze Circulation in an Area of Complex Coastal Heating. *J. Appl. Meteorol.* **31**, 1426–1438 (1992).
29. Goldreich, Y., Druyan, L. M. & Berger, H. The interaction of valley/mountain winds with A diurnally veering sea/land breeze. *J. Climatol.* **6**, 551–561 (1986).
30. Kohonen, T. K. *Self-Organizing Maps*. (Springer-Verlag, 2001).
31. Wu, S. & Chow, T. W. S. Clustering of the self-organizing map using a clustering validity index based on inter-cluster and intra-cluster density. *Pattern Recognit.* **37**, 175–188 (2004).
32. Vesanto, J. & Alhoniemi, E. Clustering of the self-organizing map. *IEEE Trans. Neural Networks* **11**, 586–600 (2000).
33. Vesanto, J. & Sulkava, M. Distance Matrix Based Clustering of the Self-Organizing Map. in *International Conference on Artificial Neural Networks 2002* 951–956 (Springer, Berlin, Heidelberg, 2002). doi:10.1007/3-540-46084-5_154.

34. Everitt, B. S., Landau, S., Leese, M. & Stahl, D. *Cluster Analysis*. (2011).
35. Arya, S. P. *Introduction to Micrometeorology*. (Academic Press, 1998).
36. Berkowicz, R. & Prahm, L. P. Evaluation of the profile method for estimation of surface fluxes of momentum and heat. *Atmos. Environ.* **16**, 2809–2819 (1982).
37. Han, J., Arya, S. P., Shen, S. & Lin, Y.-L. *An Estimation and Energy Atmospheric Theory of Turbulent Dissipation Boundary Kinetic Energy Rate Based on Layer Similarity*. *NASA technical report*. (2000).
38. Peña, A., Floors, R. & Gryning, S. E. The Høvsøre Tall Wind-Profile Experiment: A Description of Wind Profile Observations in the Atmospheric Boundary Layer. *Boundary-Layer Meteorol.* **150**, 69–89 (2014).

Paper I

Meso-microscale coupling for wind resource assessment using averaged atmospheric stability conditions

PABLO DURÁN^{1,2*}, CATHÉRINE MEISSNER², KENDALL RUTLEDGE³, RICARDO FONSECA⁴,
JAVIER MARTIN-TORRES^{4,6} and MUYIWA S. ADARAMOLA¹

¹Norwegian University of Life Sciences, Ås, Norway

²WindSim AS, Fjordgaten 15, Tønsberg, Norway

³Novia University of Applied Sciences, Vasa, Finland

⁴Luleå University of Technology, Luleå, Sweden

⁵Instituto Andaluz de Ciencias de la Tierra (CSIC-UGR), Granada, Spain

⁶The Pheasant Memorial Laboratory for Geochemistry and Cosmochemistry, Institute for Planetary Materials, Okayama University at Misasa, Tottori 682-0193, Japan

(Manuscript received July 31, 2018; in revised form April 9, 2019; accepted April 30, 2019)

Abstract

A methodology to couple Numerical Weather Prediction (NWP) models with steady-state Computational Fluid Dynamic (CFD) models for wind resource assessment applications is proposed. NWP simulations are averaged according to their atmospheric stability and wind direction. The averaged NWP simulations are used to generate the initial and boundary conditions of the CFD model. The method is applied using one year of Weather Research and Forecasting (WRF) simulations at the Honkajoki wind farm in Finland and validated by Sonic Detection and Ranging (SODAR) measurements at the site. It is shown that coupled simulations reproduce a more realistic shear for heights above 150 m. In terms of estimated energy production, there is not a big difference between coupled and standalone models. Nevertheless, a considerable difference in the horizontal wind speed patterns can be seen between the coupled and non-coupled approaches. The WRF model resolution has only a small influence on the coupled CFD results.

Keywords: Mesoscale microscale coupling, Wind energy resource assessment, Computational Fluid Dynamics (CFD), Physical downscaling, Boundary conditions

1 Coupled Computational Fluid Dynamics models in wind resource assessment

Recent wind energy projects are being increasingly developed in areas with high terrain complexity. In this kind of terrain, Computational Fluid Dynamic (CFD) models have shown much better performance compared to linear models (HRISTOV *et al.*, 2014), which have been traditionally used by the wind industry. Furthermore, it has been shown that linear models overpredict the horizontal wind speed for terrain slopes higher than 20°, whereas CFD models accurately predict the wind (YAMAGUCHI *et al.*, 2002). For these reasons, over recent years CFD models have become more preferred for wind resource assessment. Among commercial CFD codes for wind resource assessment, mostly steady-state modelling is available because of its reasonable use of computational power.

The simulated flow of CFD models depend on the prescribed initial and boundary conditions. Typically,

these boundary conditions are imposed as analytical logarithmic wind profiles. CFD models that utilize this type of boundary conditions are referred in this work as “standalone”. This approach has been traditionally used in the wind industry given their simplicity and relatively good performance when the atmospheric conditions are predominantly neutral. Nevertheless, those theoretical profiles often deviate from the observed wind profile in the area. One way to use profiles that are more realistic is to use atmospheric data calculated by Numerical Weather Prediction (NWP) models. The use of atmospheric conditions derived from an NWP model to feed a local-scale model is referred in the literature as meso-to-microscale modelling.

NWP models can reproduce mesoscale and regional wind circulation phenomena such as baroclinic pressure systems and thermal winds. Therefore, they can provide more realistic boundary conditions for CFD models than simple analytical profiles. The use of NWP model data is very common in the wind industry because of its global coverage for several decades (AL-YAHYAI *et al.*, 2010). Nevertheless, even the finest mesoscale NWP models, with horizontal grid resolutions of several hundred of meters, are not sufficient for the correct representation of the orography. This prevents a good microscale wind

*Corresponding author: Pablo Durán, Norwegian University of Life Sciences, Universitetstunet 3, 1430 Ås, Norway, e-mail: paduran@nmbu.no

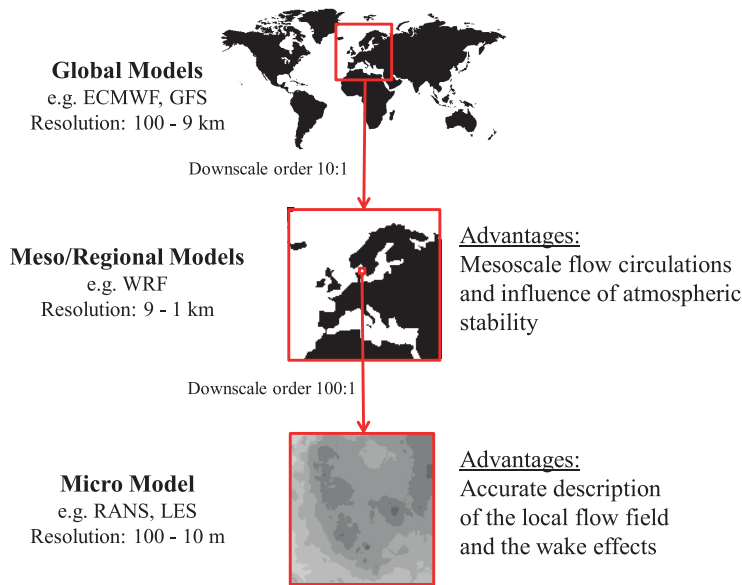


Figure 1: Spatial resolution and advantages of different numerical models used to simulate the wind flow.

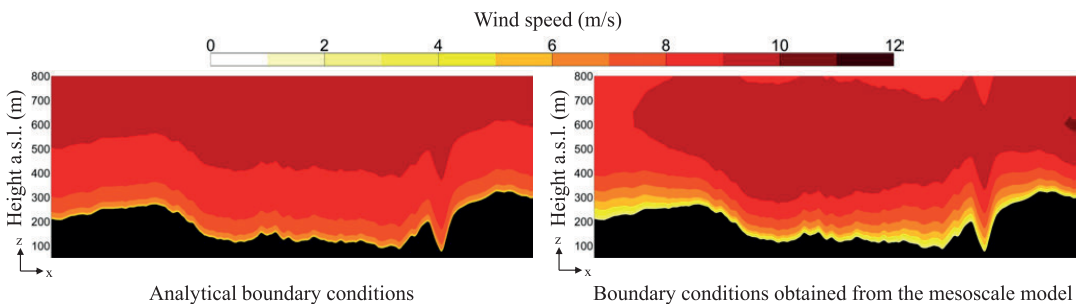


Figure 2: Example of boundary conditions for standalone (left panel) and coupled (right panel) CFD simulations.

resource estimation, especially in complex sites (BILAL et al., 2016a). It is expected that this drawback can be corrected by coupling them with microscale models like RANS CFD models, which have a horizontal grid resolution of tens of meters (Fig. 1). For this reason, the meso-to-microscale models are being widely studied in the industry and literature.

Meso-microscale methodologies that integrate input from an NWP model into a nested CFD model with finer grid are defined as physical downscaling methods (SANZ RODRIGO et al., 2017a). Different physical downscaling methods differ mainly in the downscaling procedure, the mesoscale and microscale model used, and their application (Table 1). The Weather Research and Forecasting (WRF) model (SKAMAROCK et al., 2008) is one of the most commonly used NWP models and therefore it is expected that it is also one of the most commonly used for downscaling purposes. On the other hand, the most

used CFD models correspond to large eddy simulation (LES) and Reynolds-averaged Navier–Stokes (RANS) models. Many RANS model codes exist, among which WindSim, OpenFOAM, FLUENT and VENTOS are the most cited in the literature.

In general terms, LES models are more accurate but more computational demanding in comparison with RANS models (DURASAMY, 2014). For this reason, RANS CFD models are more commonly used in the wind energy industry (DURASAMY, 2014; VEIGA RODRIGUES et al., 2016). In the current study the CFD Software WindSim, which uses steady-state RANS equations, is used.

There are two main approaches for physical downscaling of mesoscale model results using CFD models. One approach is to run the CFD simulation using analytical boundary conditions and scale the 3-D CFD wind field with the mesoscale wind speed at one or several se-

Table 1: Classification of previous studies that use meso-microscale coupling. RANS based models are highlighted in bold.

Model		Application	Reference(s)
Mesoscale	Microscale		
WRF	WindSim	Wind energy	BILAL et al., 2016a; BILAL et al., 2016b; CASTELLANI et al., 2006; MEISSNER et al., 2015
WRF	OpenFOAM	Wind energy Urban flow	BOUTANIOS et al., 2010; LEBLEBICI et al., 2014; LEBLEBICI and TUNCER, 2015 MIAO et al., 2013; ZHENG et al., 2015
WRF	HELIOS	Wind energy	GOPALAN et al., 2014; SITARAMAN, 2013; SITARAMAN et al., 2013
Others	FLUENT	Wind energy Urban flow	LI et al., 2010; SCHNEIDERBAUER and PIRKER, 2010 LI et al., 2007; SOLAZZO et al., 2006
Others*	VENTOS	Wind energy Urban flow	VEIGA RODRIGUES et al., 2008, 2016 VEIGA RODRIGUES and PALMA, 2014
WRF	LES	Wind energy Urban flow	LIU et al., 2011; LUNDQUIST et al., 2008; MIROCHA et al., 2013, 2014; MIROCHA and KIRKIL, 2010; MOENG et al., 2007; MUÑOZ-ESPARZA et al., 2014; SANZ RODRIGO et al., 2017b KINBARA et al., 2010; LIU et al., 2012; NAKAYAMA et al., 2011
MM5	Various CFD	Urban flow	BAIK et al., 2009; NOZU et al., 2009; SOLAZZO et al., 2006; TAKEMI et al., 2006
Others	Linear	Wind energy	AL-YAHYAI et al., 2012; BADGER et al., 2014; CARVALHO et al., 2013; MURAKAMI et al., 2003; YU et al., 2006

*Mostly WRF

Table 2: List of publications that conduct meso-microscale physical downscaling with RANS CFD models.

Reference	Downscaling method	Type of simulation	Long term statistics or duration	Application
LI et al., 2007	Direct coupling	Steady-state	Selected NWP time-steps	Urban wind flow
ZHENG et al., 2015	Direct coupling	Steady-state	2 days approx.	Urban wind flow
FOLCH et al., 2016	Scaled Default CFD	Steady-state	24 directional sectors	Gas dispersion
SANZ RODRIGO et al., 2010	Scaled Default CFD	Steady-state	12 directional sectors	Regional wind map
BILAL et al., 2016a	Scaled Default CFD	Steady-state	12 directional sectors	Wind energy production
DURASAMY et al., 2014	Direct coupling	Steady-state	Clustering	Wind energy production

lected grid points. The second approach, referred to as direct coupling in the literature (SANZ RODRIGO et al., 2017a), uses the NWP model output to define the initial and boundary conditions of the CFD simulation (Fig. 2). The scope of this study is to explore the capabilities of the latter approach.

Most of the literature about coupled RANS CFD models is focused on unsteady simulations which allows for the temporal description of wind flow (BAIK et al., 2009; CASTRO et al., 2015; LI et al., 2010; VEIGA RODRIGUES et al., 2016; VEIGA RODRIGUES and PALMA, 2014; SCHNEIDERBAUER and PIRKER, 2010). Wind resource assessment models used in the wind industry are usually validated with measurements covering some years, which makes unsteady simulations too expensive in terms of time and computational power. Hence, steady-state simulations are preferred in the wind industry. However, most of the previous studies on coupled steady-state CFD models (see Table 2) have not explored direct coupling for wind energy applications.

In this work, we propose a direct coupling methodology for steady-state CFD simulations for wind resource assessment purposes. It intends to improve the CFD simulations by transferring the average wind speed patterns

from the mesoscale model to the CFD model. The consideration of different atmospheric stability conditions in the coupling procedure allows the CFD to capture the observed predominant wind flow conditions, while still making a reasonable use of computational resources in the context of the industry.

This paper is divided into five sections. In Section 2 details about the validation site, datasets, coupled numerical models and validation methodology, are presented. In Section 3 the coupling methodology applied to the WRF and WindSim models is presented. In Section 4 the coupling model is evaluated to then provide conclusions in Section 5.

2 Dataset, models and methods

In the following subsections, the measurement data as well as the data and set-up used to build the WRF and CFD models are presented. Finally, the validation methodology used in this study is explained.

2.1 Validation site and data sets

The Honkajoki wind farm is used as a validation site of the proposed methodology. The wind farm consists of

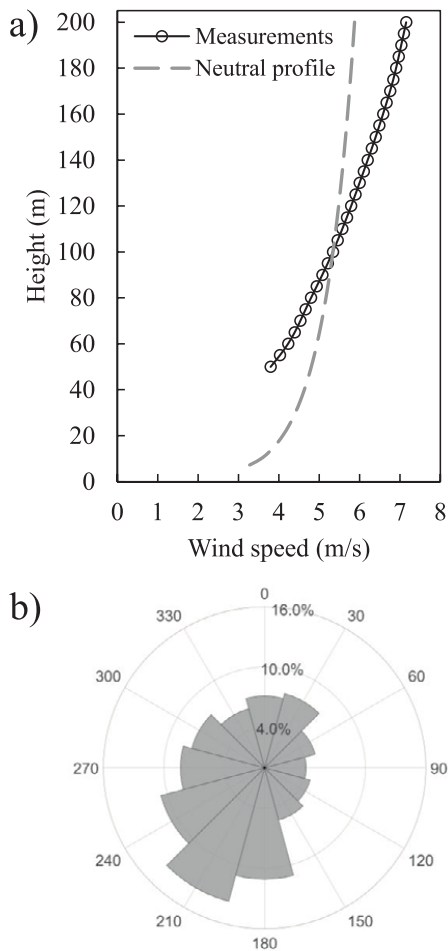


Figure 3: a) Measured vertical profile of mean horizontal wind speed and b) wind rose at 100 meters.

9 Nordex N117/2400 units with a hub height of 120 m and a rotor diameter of 117 m. The site is located in Honkajoki municipality of Satakunta region, in Finland, about 3.5 km to the southeast of the town of Honkajoki and around 45–50 km east from the coast. The terrain at the site is flat, with an absolute height difference of approximately 33 m within the area modelled in the microscale domain. The surface cover consists mainly of forest with presence of an urban area belonging to the Honkajoki town, in the north-west corner of the site.

The wind conditions have been monitored through a SODAR positioned at the coordinates 61.98° N, 22.32° E and elevation 117.1 m, between 19 February 2016 and 19 April 2017. For this period ten-minute averages and standard deviations of horizontal and vertical wind components are available at altitudes between 50 m and 200 m above ground level (a.g.l.) with a vertical res-

olution of 5 m. The measured vertical profile of mean horizontal wind speed has a higher shear compared to a neutral wind profile as shown in Fig. 3. This is due to a strong influence of stable atmospheric conditions in the site, which are common in mainland Finland. As presented in Fig. 3, the main wind directions are southerly (180°) and south-westerly (210° and 240°).

2.2 WRF model

In this study WRF version 3.7.1 is forced with the National Centers for Environmental Prediction Climate Forecast System Reanalysis (CFSR) 6-hourly data (SAHA et al., 2010) and is run for 1 year from March 2016 to March 2017. The WRF version used in this work contains most of the improvements made in Polar WRF (HINES and BROMWICH, 2008), a modified version of the model optimized for the polar regions and is therefore suitable for this year-long simulation. The wind farm parameterization scheme available in WRF based on FITCH et al. (2012) is switched on in all model domains and set up for the Honkajoki wind farm using turbine data provided by the manufacturer. This scheme assumes that the wind turbines act as a momentum sink on the mean flow transferring a fraction of the kinetic energy into electricity and the rest into turbulent kinetic energy. The latter represents the mixing of the ambient flow by the turbines.

The following physics parameterizations are selected: Goddard (six-class) Cloud Microphysics Scheme (TAO et al., 1989); Rapid Radiative Transfer Model for Global Circulation Model Applications (IACONO et al., 2008) with climatological aerosol distribution (TEGEN et al., 1997) for both short-wave and long-wave radiation; Monin-Obukhov surface layer scheme (MONIN and OBUKHOV, 1954) with the Mellor-Yamada Nakanishi and Niino level 2.5 Planetary Boundary scheme (NAKANISHI and NIINO, 2004, 2006); Noah land surface model (CHEN and DUDHIA, 2001); and Betts-Miller-Janjić (JANJIĆ, 1994) cumulus scheme with precipitating convective cloud scheme (KOH and FONSECA, 2016). The WRF model configuration used in this work is the one found to give the best agreement with observed data at the Honkajoki site out of the different configurations considered for the month of April 2016.

Three domains were used in the WRF model experiments (Fig. 4). The setup of domains 1 and 2 are identical to the ones used by WANG et al. (2019). Domain 1 has a spatial resolution of 15 km and comprises the entire Scandinavian Peninsula (144×160 grid nodes). Domain 2 uses a 3 km resolution and includes most of the Botnia-Atlantica region (301×381 grid nodes). Domain 3 uses a 600 m resolution, centered over the Honkajoki wind park (96×96 grid nodes). The model has 60 vertical levels, spanning up to 30 hPa (~25 km). A higher vertical resolution in the Planetary Boundary Layer is used, with about 20 levels in the lowest 200 m. In domain 2 and 3, the cumulus parametrization scheme is not used and instead convection is explicitly resolved

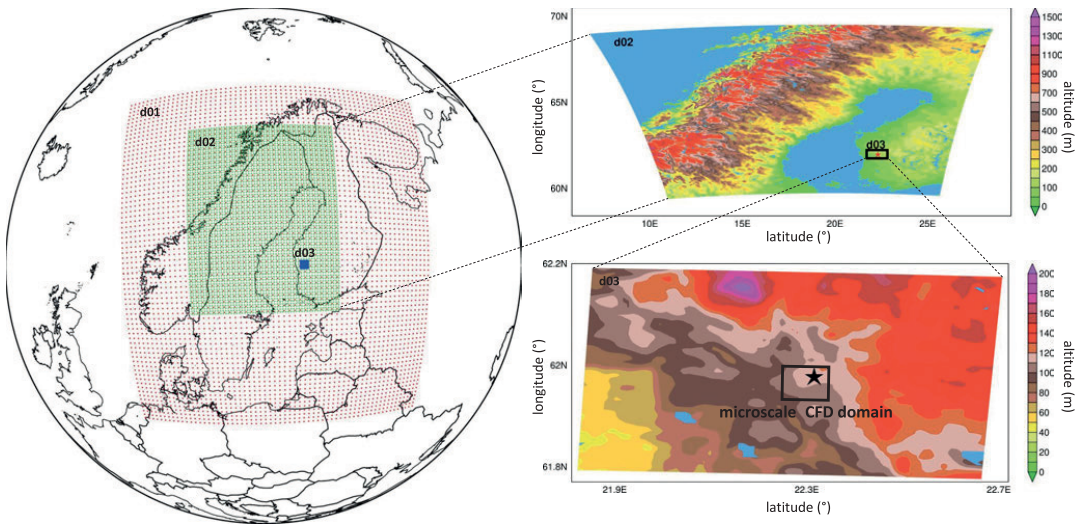


Figure 4: Spatial extent of domain 1 (d01), domain 2 (d02), domain 3 (d03) of the WRF model used in the simulations. The microscale CFD domain is indicated as a black rectangle in the lower-right panel. The sodar position is indicated with a star in the top- and bottom-right panels.

by the model. In domain 1, grid nudging towards CFSR is employed. The water vapor mixing ratio is nudged in the mid- and upper-troposphere while the horizontal wind components and potential temperature perturbations are nudged in the upper-troposphere and lower stratosphere. The nudging time-scale is set to 1 h for all variables.

In order to limit the accumulation of integration errors, following Lo et al. (2008), each month’s run is broken into three overlapping 11/12-day periods with the first day regarded as model spin-up. For example, for March 2016 the model is run from 29th February to 11th March, 10th March to 21st March and 20th March to 1st April. The output is stored every 3 h, 1 h and 10 min for the domains 1, 2 and 3, respectively. For this work, the output of grids d02 and d03 are used.

The albedo, vegetation fraction and leaf area index used in the WRF simulations are derived from the National Oceanic and Atmospheric Administration Advanced Very High Resolution Radiometer (AVHRR) multi-year data (Csizsar and Gutman, 1999; Gutman and Ignatov, 1998). The other land surface parameters are assigned to each land category from a 1 km AVHRR data spanning April 1992 to March 1993 (Loveland et al., 2000). The terrain input used in the WRF runs is interpolated from a ~925 m spatial resolution dataset generated by the United States Geological Survey (USGS) that comes with the WRF pre-processor.

2.3 WindSim model

The CFD software WindSim is used to simulate the wind flow in the microscale model domain. The WindSim CFD model is based on RANS equations for momentum, turbulence and temperature, using the standard

$k-\varepsilon$ turbulence closure scheme. More information about the governing equations of the model are detailed in the works of GRAVDAHL (1998). To consider atmospheric stability effects in the atmosphere the potential temperature equation is solved explicitly. The change of the mean potential temperature is influenced by advection, thermal diffusion and turbulent heat transfer (MEISSNER et al., 2009). Forest is modelled in accordance to BUSCH (2017). The software solves the atmospheric steady-state flow for a given set of initial and boundary conditions through numerical methods. In this study, the Coriolis force is not included in the microscale modelling. Wind turbines are not explicitly represented in the microscale model. For energy calculations in Section 4.4, an analytical wake model is used to account for the impact of the wind turbines.

The digital terrain model has a horizontal spatial resolution of 20 m × 20 m. In the vertical direction, the grid extends up to 450 m, with a finer vertical spatial resolution towards the ground, which has a grid size lower than 10 m for heights below 100 m a.g.l (Fig. 5). The modelled area is a rectangle of approximately 4.8 km × 6.6 km, with the lower left corner at 565,498 m east 6,867,799 m north and the upper right at 570,318 m east 6,874,439 m north in the Universal Transverse Mercator coordinate system, Zone 34.

Data about the elevation and canopy of the site was retrieved from the National Land Survey of Finland (<https://www.maanmittauslaitos.fi/en>). This website provides laser altimetry data and various resolution altimetry models for most of Finland. The datasets retrieved from this website correspond to elevation model data with a horizontal resolution of 2 m and point-like laser scanning data depicting objects on the ground with

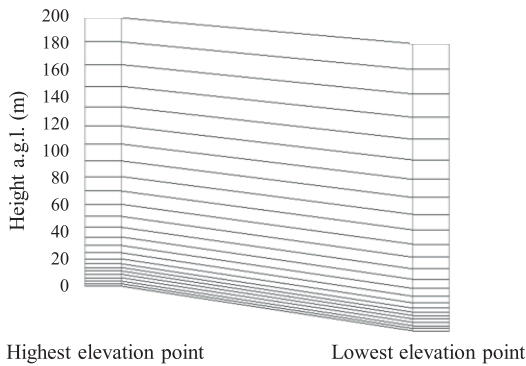


Figure 5: The left and right columns display a schematic view of the vertical grid distribution at the position with maximum and minimum elevation, respectively, in the CFD domain. For visualization purposes up to 200 m a.g.l. is displayed.

Table 3: Canopy height (h_c) ranges used to model the forest. For a given range, one canopy height and a number of cells are used to build the forest in the model.

Canopy height range (m)	Modeled Canopy height (m)	Number of grid cells used
$1 < h_c \leq 2.5$	1.75	1
$2.5 < h_c \leq 5$	3.75	2
$5 < h_c \leq 7.5$	6.25	3
$7.5 < h_c \leq 10$	8.75	4
$10 < h_c \leq 12.5$	11.25	5
$12.5 < h_c$	13.75	6

their respective horizontal and vertical coordinates. The data was retrieved in December 2018. Both datasets were aggregated into the 20 m resolution grid of the CFD model. The canopy height was obtained by subtracting the elevation from the laser altimetry data and then used to model 6 layers of forest (Table 3). For canopy heights lower than 1 m it was assumed that no forest was present and therefore they correspond to grassland. By visual inspection, for important areas of the site the aerodynamic roughness data was manually corrected, like farmlands, asphalt, residential areas and buildings (Fig. 6).

2.4 Validation methodology

In wind resource assessment studies, it is necessary to extrapolate measurements taken at one point, to the planned turbine positions in order to assess the wind energy potential. The horizontal and vertical transfer in space of those measurements need to be done either by analytical formulas or by 3-D models, like RANS CFD. For wind energy applications, RANS CFD model results are Reynolds number independent (BACHANT and WOSNIK, 2016; BERG et al., 2011). This means that wind flow relative perturbations caused by the orography are independent of the wind speed. In other words, the ratio be-

tween the wind speed values at two different locations of the simulated domain are independent of the wind speed. Such ratio is defined as the “speed-up ratio” and is the variable used to quantify the performance of the microscale model. Since the speed-up ratios depend only on the orography, they also depend only on the wind direction. In this study, 12 different wind directions are simulated, generating 12 sets of speed-up ratios.

The validation of the microscale model consists in first “transferring” the wind speeds from a reference measurement to the location of a target measurement (Fig. 7). The transferring is performed by multiplying the wind speeds at the reference, u_R , by the corresponding speed-up ratio, SU . For a given measured wind direction at the reference point α_R , the speed-up ratio is obtained by linearly interpolating the speed-ups of the two closest wind directions. For example, if the total number of simulated directional sectors, D , is 12 as in this study, and the measured direction is 15° , the SU is interpolated from the speed-ups modelled for wind directions 0° and 30° . The transferred values are compared to the measured wind speed at the target, u_T . The performance of the model is then quantified by the crosschecking prediction error, XPE , defined as:

$$XPE(R, T) = \frac{\sum_{t=1}^{N(R,T)} \frac{u_R(t)}{N(R,T)} \cdot \sum_{t=1}^{N(R,T)} \frac{SU(\alpha_R(t))}{N(R,T)} - \sum_{t=1}^{N(R,T)} \frac{u_T(t)}{N(R,T)}}{\sum_{t=1}^{N(R,T)} \frac{u_T(t)}{N(R,T)}} \quad (2.1)$$

$N(R, T)$ is the total number of concurrent measured timesteps t between the reference R and the target measurement T , and α_R is the measured wind direction at the reference point. In contrast to validation metrics used in WRF or Unsteady RANS models, where deterministic values are compared, the objective of the XPE is to validate the simulated speed-up ratios and not the simulated wind speed values.

Crosschecking prediction errors can also be obtained for a particular directional sector, in which case is denoted as $XPE_\Lambda(R, T)$, with $\Lambda = \{(i - 1) \cdot 360^\circ / D, i = 1, \dots, D\}$. In this case, the same expression as in equation (2.1) is used, with the summation limited to α_R values within the range $[\Lambda - 360^\circ / 2D, \Lambda + 360^\circ / 2D]$, in which case the total number of concurrent timesteps is denoted as $N_\Lambda(R, T)$.

3 Meso-to-microscale coupling methodology

The WRF simulations results are used to drive the microscale wind flow model. Representative WRF fields are generated for different atmospheric stability conditions and wind directions by averaging the WRF data. These averaged fields are used to generate the initial and boundary conditions of the CFD model. The averaging and transferring methodologies are detailed in the following subsections.

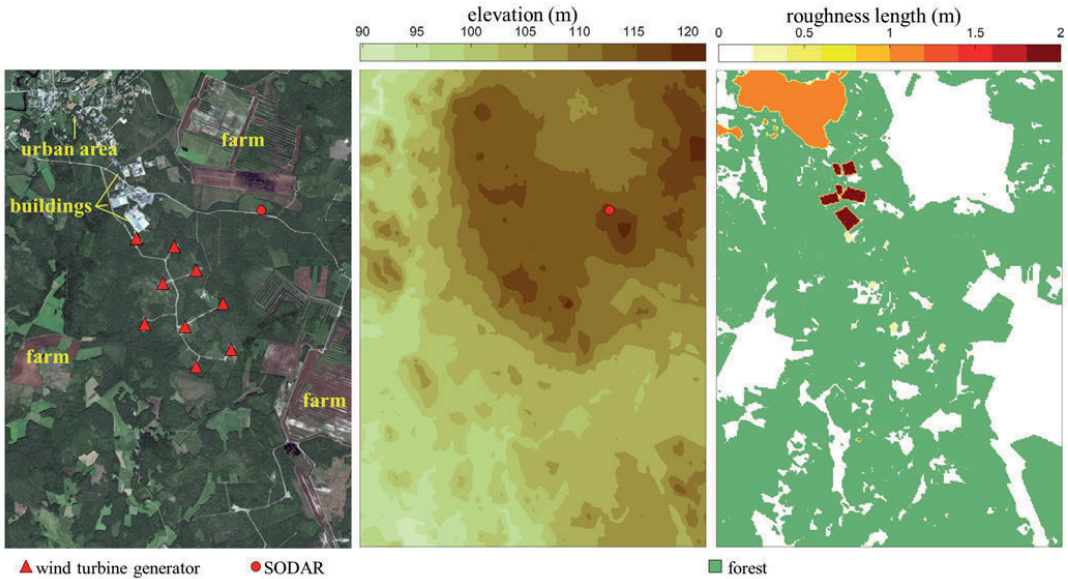


Figure 6: Satellite image (left), elevation (center) and aerodynamic roughness length (right) of the CFD digital model. In the satellite image the position of the wind turbines of the Honkajoki windfarm is shown as well as relevant areas in the domain.

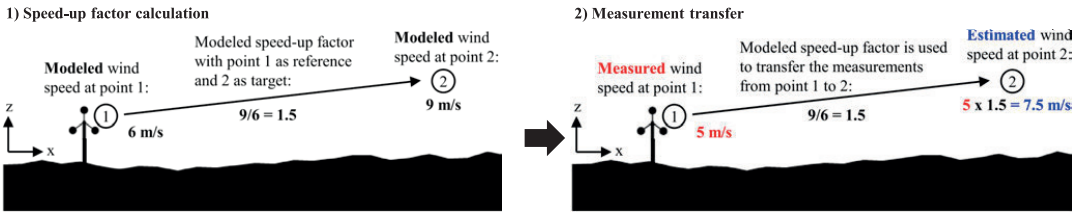


Figure 7: Example of measurement transfer using RANS CFD model results.

3.1 Calculation of representative atmospheric conditions

The meso-microscale coupling could be conducted by running one microscale simulation for each timestep of the WRF data. With this procedure, the estimation of the annual energy production of a wind energy project would require 8760 steady-state simulations for hourly WRF data. This high demand of computational resources is prohibitive in the industry, and therefore, a method to generate representative boundary conditions has been proposed.

The developed methodology consists in generating one representative mesoscale field per wind direction and/or per atmospheric stability condition, from the 1-year WRF simulation. These fields are computed by averaging all WRF data with the same representative main wind direction and atmospheric stability. The main wind direction is determined by averaging the wind directions of all WRF grid-points at the inlets of the micro-

scale domain between 60 m and 160 m a.g.l. By using this procedure, it is expected that the main mesoscale conditions at the heights of interest for wind energy generation can be captured.

When atmospheric stability is considered, the representative atmospheric stability is estimated from the shear exponent of one vertical profile of horizontal wind speed (SUTTON, 1949). This profile is obtained by averaging in the horizontal direction the wind speeds of all WRF grid-points inside the CFD domain. All vertical levels between 50 and 100 m are used to compute the shear exponent. The thresholds used to classify the atmospheric stability are based on the work of WHARTON and LUNDQUIST (2012) and the reference therein. Shear exponents <0.1 are considered unstable, >0.2 are considered stable and between those two thresholds it is considered neutral.

In this work, two versions of the proposed coupling methodology are used, one without considering atmospheric stability, here referred as to “all-stabilities”, and

the other considering three atmospheric stability classes: unstable, neutral and stable. All-stabilities simulations correspond to the average of all WRF timesteps throughout the year for a given wind direction, whereas the other simulations average the WRF timesteps throughout the year that belong to a particular stability class. The averaging procedure is conducted for each of the 12 directional sectors, yielding a total of 12 WRF fields for each of the four cases.

The averaging is conducted at each grid-point of the WRF domain. The following variables from the WRF model are considered in the coupling: (i) wind velocity vector, (ii) potential temperature, (iii) boundary layer height and (iv) friction velocity. These variables are directly averaged except for the horizontal components of wind speed and friction velocity. In the case of horizontal wind speed, magnitude and direction are averaged instead. Then the horizontal components of the wind are calculated by projecting the averaged horizontal wind speed according to their averaged direction. On the other hand, the averaged friction velocity is computed using the root mean square of the friction velocities.

3.2 Boundary conditions for CFD simulations

In RANS CFD simulations the values of all variables are iteratively re-calculated inside domain until they converge to a stable solution. This iterative procedure starts from a set of initial values which, in the case of steady-state CFD simulations, are fixed at the lateral and top boundaries during the whole simulation. The prescribed variables are the horizontal wind speed u , potential temperature θ , turbulent kinetic energy (TKE), k , and its energy dissipation rate (EDR), ε . In this study, two sets of initial and boundary conditions are used: 1) standalone and 2) coupled. For standalone simulations, the boundary conditions are computed from analytical profiles. For coupled simulations, wind speed and potential temperature are directly interpolated from the WRF model, while TKE and EDR are calculated using variables derived from the WRF model, in a similar fashion as DURAISAMY (2014). One year of WRF output is used to generate the boundary conditions for the coupled simulations. Each of these simulations is compared with standalone simulations using similar wind direction and atmospheric stability.

3.2.1 Standalone CFD simulations

Analytical profiles are prescribed for every given wind direction. These profiles are derived from the Monin-Obukhov similarity theory in HAN et al. (2000):

$$u(z) = \begin{cases} \frac{u_*}{\kappa} \left[\ln\left(\frac{z}{z_0}\right) - \psi_m\left(\frac{z}{L}\right) + \psi_m\left(\frac{z_0}{L}\right) \right] & , z \leq h \\ u_G & , z > h \end{cases} \quad (3.1)$$

$$\theta(z) = \theta_0 + \frac{\theta_*}{\kappa} \left[\ln\left(\frac{z}{z_{h0}}\right) - \psi_h\left(\frac{z}{L}\right) + \psi_h\left(\frac{z_{h0}}{L}\right) \right] \quad (3.2)$$

$$k(z) = \begin{cases} \frac{u_*^2}{\sqrt{C_\mu}} \left(1 - \frac{z}{h}\right)^2 & , z \leq h; \\ & , L < -200; \\ & , L > 0 \\ \left(0.36 + \left(0.9 \left(\frac{z}{h}\right)^{2/3} \left(1 - 0.8 \frac{z}{h}\right)^2\right) w_* \right) & , z \leq h; \\ & , -200 < L < 0 \\ 0 & , z > h \end{cases} \quad (3.3)$$

$$\varepsilon(z) = \begin{cases} \frac{u_*^3}{\kappa C_\mu} \left(1.24 + 4.3 \frac{z}{L}\right) \left(1 - 0.85 \frac{z}{L}\right)^{3/2} & , z \leq h; L > 0 \\ \frac{w_*^3}{h} \left(0.8 - 0.3 \frac{z}{L}\right) & , z \leq h; L < 0 \\ 0 & , z > h \end{cases} \quad (3.4)$$

$$w_* = \left(\frac{g}{\theta_0} (\overline{w\theta}) h\right)^{1/3} \quad (3.5)$$

$$\psi_m = \begin{cases} -5 \frac{z}{L} & , \frac{z}{L} \geq 0 \\ 2 \ln\left(\frac{1+x}{2}\right) + \ln\left(\frac{1+x^2}{2}\right) & , \frac{z}{L} \leq 0 \\ -2 \arctan(x) + \frac{\pi}{2} & \end{cases} \quad (3.6)$$

$$\psi_h = \begin{cases} -5 \frac{z}{L} & , \frac{z}{L} \geq 0 \\ 2 \ln\left(\frac{1+x^2}{2}\right) & , \frac{z}{L} \leq 0 \end{cases} \quad (3.7)$$

$$x = \left(1 - 16 \frac{z}{L}\right)^{1/4} \quad (3.8)$$

$$L = -\frac{\theta_0 u_*^3}{\kappa g (\overline{w\theta})} = \frac{\theta_0 u_*^2}{\kappa g \theta_*} \quad (3.9)$$

Here u_* is the friction velocity, u_G is the geostrophic wind, z_0 is the roughness length, h is the atmospheric boundary layer height, κ ($= 0.4$) is the Von Karman constant and L is the Monin-Obukhov length. The convective velocity scale, the gravitational acceleration, the reference temperature and the surface sensible heat flux are denoted as w_* , $g\theta_0$ and $(\overline{w\theta})$ respectively. ψ_m and ψ_h are the stability correction functions for wind speed and potential temperature, respectively (BUSINGER et al., 1971; DYER, 1974). It is assumed $z_{h0} = 0.1z_0$ (GARRATT, 1992). If neutral conditions are considered, the friction velocity is computed by enforcing $u(h) = u_G$ in equation (3.1). Otherwise, the friction velocity is obtained from a prescribed reference speed u_{ref} at a certain height z_{ref} by $u(z_{ref}) = u_{ref}$. The values of θ_* and $(\overline{w\theta})$ are computed from equation (3.9). At the top boundary of the CFD model, a no-friction wall is prescribed. Wind direction is assumed to be constant with height.

3.2.2 Coupled CFD simulations

For coupled CFD simulations, wind speed and potential temperature boundary conditions are computed by interpolating and extrapolating the WRF values onto the microscale grid. Vertical interpolation is conducted using cubic spline interpolation and horizontal interpolation by linear interpolation. In the case of the wind speed, the interpolation is conducted with respect to

the height above ground level, whereas for the potential temperature it is conducted with respect to the height above sea level. For the grid cells of the microscale domain below the lowest vertical level of the WRF model (z_{\perp}), extrapolation is conducted using equations (3.10) and (3.11), where u_{\perp} and θ_{\perp} are the wind speed and potential temperature at the lowest vertical level of the WRF domain. u_* is retrieved from the WRF model, L is computed using the gradient method (ARYA, 1998), θ_* is computed from equation (3.2) and $(\overline{w\theta})$ is computed from equation (3.9).

$$u(z) = u_{\perp} - \frac{u_*}{\kappa} \left[\ln\left(\frac{z_{\perp}}{z}\right) - \psi_m\left(\frac{z_{\perp}}{L}\right) + \psi_m\left(\frac{z}{L}\right) \right] \quad (3.10)$$

$$\theta(z) = \theta_{\perp} - \frac{\theta_*}{\kappa} \left[\ln\left(\frac{z_{\perp}}{z}\right) - \psi_h\left(\frac{z_{\perp}}{L}\right) + \psi_h\left(\frac{z}{L}\right) \right] \quad (3.11)$$

Because interpolated values might not conserve mass in the microscale domain, mass conservation is enforced at the top and lateral boundaries. As done in VEIGA RODRIGUES et al. (2016), the correction factor ϕ_b for the normal velocities at the boundary b is calculated from equations (3.12) and (3.13). Here A_i is the grid area and S_b is the set of points belonging to the boundary $b \in [1, 5]$ (four lateral boundaries plus top boundary). \dot{m}_b corresponds to the mass flow, where positive sign indicates that mass is flowing into the domain.

$$\phi_b = 1 - \text{sgn}(\dot{m}_b) \frac{\sum_{k=1}^5 \dot{m}_k}{\sum_{k=1}^5 |\dot{m}_k|} \quad (3.12)$$

$$\dot{m}_b = \sum_{i \in S_b} \rho A_i u_{\perp, i} \quad (3.13)$$

TKE and EDR cannot be directly transferred from the mesoscale model to the microscale model. Coarser grids cannot describe smaller fluctuations of the wind flow, and therefore, the amount of TKE in a grid-box would be higher compared to a finer grid (MOENG et al., 2007). Therefore, TKE and EDR are computed using equations (3.3), (3.4) and (3.5) in a similar fashion as DURAISAMY (2014). Here u_* and h are horizontally interpolated from the WRF domain.

4 Comparison of the coupled and standalone simulations

The methodology presented in Section 3 is used to produce representative WRF data for the previously defined atmospheric stability conditions: (i) all-stabilities, (ii) unstable, (iii) neutral and (iv) stable. The representative WRF fields of each of the 12 directional sectors are used to force the coupled microscale CFD models. In order to assess the improvement of the coupled methodology, the results are compared for each stability case with their corresponding standalone microscale simulations and the averaged WRF field.

Standalone simulations correspond to the standard application of CFD models in the wind industry for

wind resource assessment. The values used to compute the boundary conditions of the standalone microscale simulations are presented in Table 4. These values were selected in order to have a good fit with the observed SODAR profile for each respective atmospheric stability case.

To calculate the simulation error of each atmospheric stability case, the measurements are also filtered according to the measured shear exponent between 50 and 100 m. The classification of measurements is performed over 30-min averages in order to reduce the noise. The same thresholds used in the classification of the WRF fields are used for the measurements. The frequency distribution of the atmospheric stability in the WRF simulations and measurements is presented in Fig. 8. Domain 2 and 3 of the WRF model have identical wind roses and therefore only the last is presented. The wind rose of the WRF simulations is quite similar to the measured one when all data is compared. This is also true for the stable case but not for the unstable and neutral case. Nevertheless, over the full year, the proportion of stability classes in the WRF simulations and SODAR is similar, with a slight over representation of neutral cases in the WRF model.

The main purpose of wind flow models is to extrapolate measured wind horizontally and vertically. Typically, measurements are conducted at about 60 to 120 m and vertically extrapolated to higher heights and/or horizontally extrapolated at places where wind turbines would like to be placed. For this reason, all comparisons in this section were conducted using the measured wind speed at 80 or 120 m as a reference. Only wind speeds above 3 m/s were considered for the calculation of the wind profiles and errors, since they are of interest for wind energy calculations. Only directional sectors with a frequency higher than 5.5 % (~15 days) are discussed in the following section. This assures that the discussion is based on observation with statistical significance.

4.1 Vertical profiles of horizontal wind speed

For each atmospheric stability case, the profiles of horizontal wind speed simulated at the SODAR position by the different approaches are compared. The approaches correspond to one set standalone simulations and two sets of coupled simulations. Each of these sets correspond to one simulation per directional sector. In addition, the averaged profile of the WRF d02 and d03 at the SODAR position are shown for each case. The profiles were scaled to match the SODAR wind speed at 80 m in order to validate the speed-up ratios, as discussed in the previous paragraph. This qualitative comparison is presented for the most frequent wind directions at 80 m for all-stabilities and stable cases (Fig. 9 and Fig. 10). The number of occurrences for the neutral and unstable case are very low, therefore only the sector with the highest frequency will be shown (Fig. 11).

When all stabilities are considered (Fig. 9) there are not important differences between the coupled and stan-

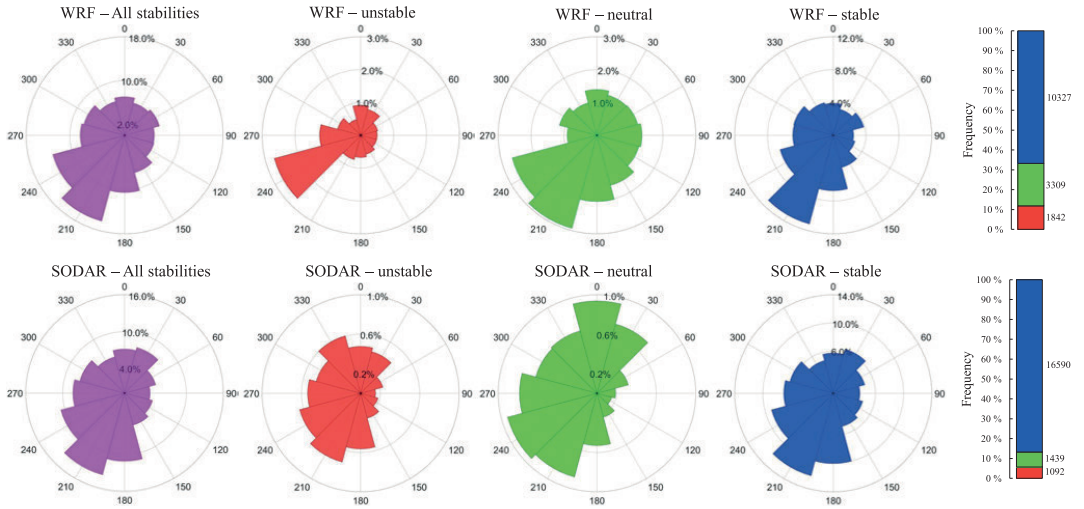


Figure 8: Wind roses of the representative direction of the WRF d03 timesteps (top) and of the measured wind at 100 m by the SODAR (bottom) for the different stability classes: all stabilities (magenta), unstable (red), neutral (green) and stable (blue). In the right panels the frequencies of the stability classes within the simulated and measured period, respectively, are displayed. Next to the bars, the number of 30-min timesteps per stability is shown.

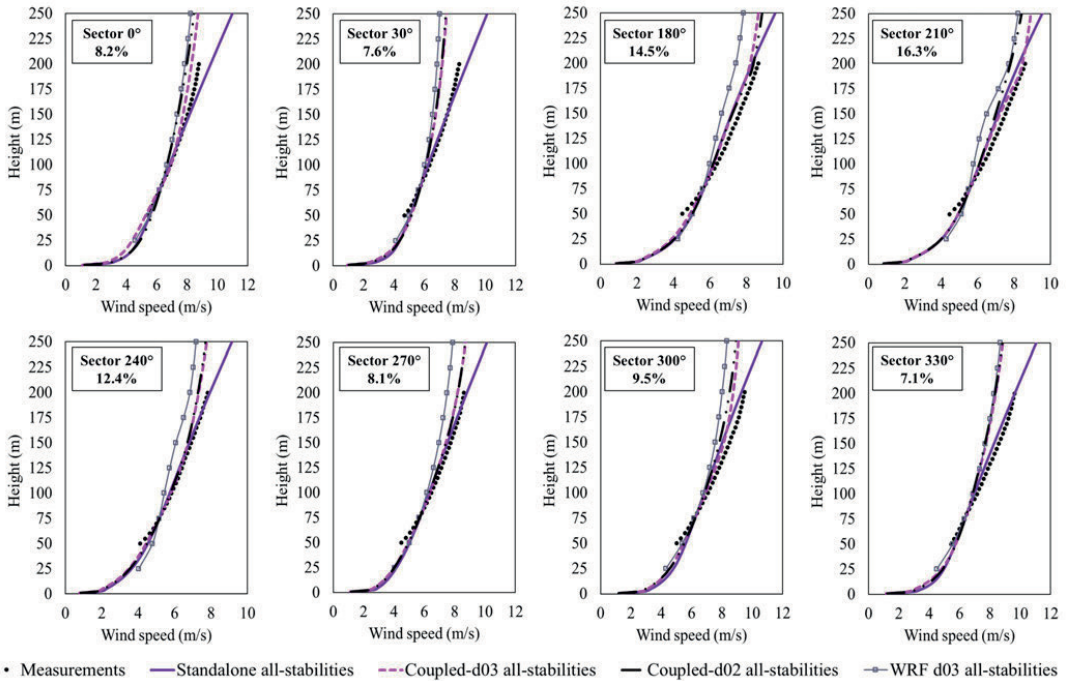


Figure 9: Simulated horizontal wind speed vertical profiles for the main wind directions for all stabilities. Standalone, coupled and WRF simulated profiles are shown. At the top-left corner of each panel, the directional sector and its frequency is displayed. Coupled-d02 and Coupled-d03 are forced using WRF output from grids d02 and d03, respectively.

Table 4: Prescribed physical parameters used to compute the boundary conditions of each standalone microscale simulation.

Atmospheric stability condition	Input variables				
All stabilities	$u_{ref} = 6.13$ m/s	$z_{ref} = 100$ m	$h = 400$ m	$\theta_0 = 280$ K	$L = 150$ m
Unstable	$u_{ref} = 4.39$ m/s	$z_{ref} = 100$ m	$h = 1000$ m	$\theta_0 = 280$ K	$L = -200$ m
Neutral	$u_G = 6.30$ m/s		$h = 500$ m		
Stable	$u_{ref} = 6.26$ m/s	$z_{ref} = 100$ m	$h = 400$ m	$\theta_0 = 280$ K	$L = 100$ m

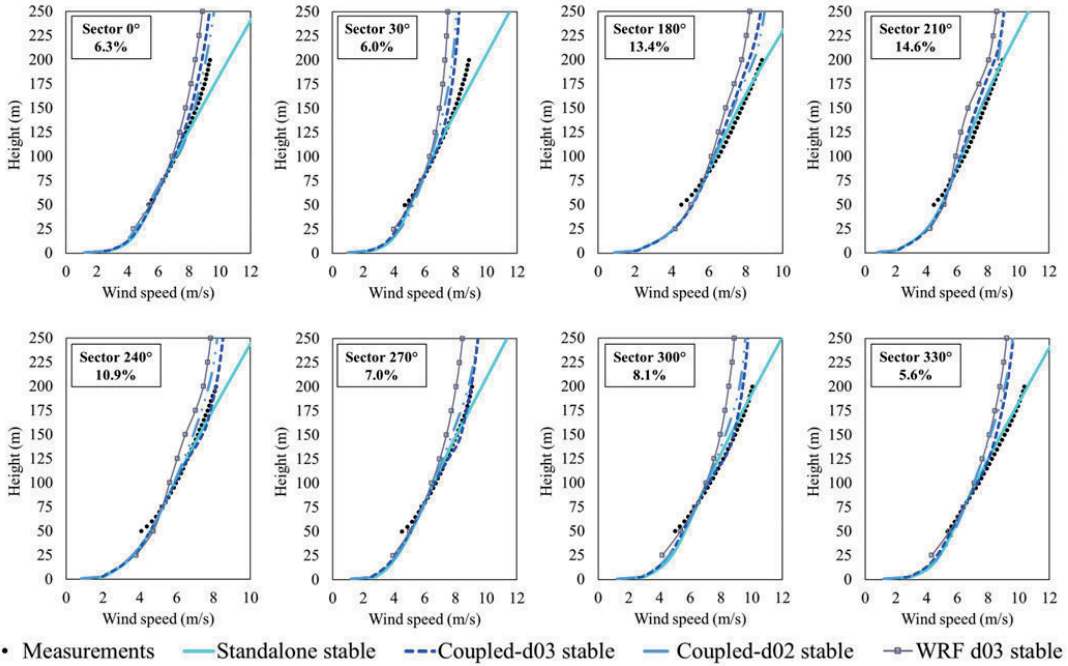


Figure 10: Same as Fig. 9 but for stable atmospheric conditions.

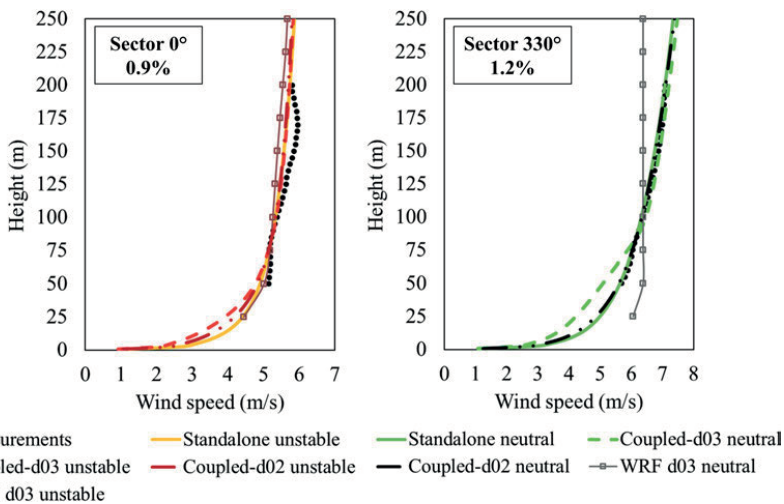


Figure 11: Same as Fig. 9 but for unstable (left) and neutral (right) atmospheric conditions.

alone approaches. In some sectors, the coupled simulations present a better performance (sectors 0° and 210°), in some sectors the standalone profiles fit better (sectors 30° , 240° , 330°) and for some sectors, they can be quite similar (sectors 180° , 270° , 300°). In most of the presented sectors, differences are rather small. In addition, for most sectors the microscale simulations present a better performance compared with the profile obtained from the WRF model. It is interesting to note that there is not a big difference between the coupled simulations forced by the WRF outputs from d02 and d03.

Despite these inconclusive results, it is important to highlight that coupled simulations tend to present a more realistic shear for heights above 150 m. Standalone simulations presents a rather high and constant shear above 80 m. In the coupled simulations, the shear decreases towards higher heights, which is also seen in the measurements. It is then expected that coupled simulations have a better performance when extrapolating measurements to higher heights. Standalone simulations cannot reproduce this since their boundary conditions use wind speed profiles assuming that Monin-Obukhov similarity theory is valid up to the boundary layer height.

For stable simulations (Fig. 10), the coupled simulations are as good or better than the standalone approach for sectors 0° , 30° , 180° , 210° , 240° and 270° . In sectors 0° , 240° and 270° the improvements are important. In most sectors, both coupled sets of simulations behave similarly. Nevertheless, the one forced by the highest resolution WRF output (d03) presents a lower performance for sectors 240° and 270° . For all sectors, the direct use of the WRF output gives worse results, as the shear is lower than the measured one. The most probable reason for the lower shear is that in stable cases the wake from the wind farm is sustained longer and therefore underestimating the wind speed.

In the same way as when all stabilities were considered, standalone simulations present a high and constant shear above 80 m. This is not the case for the coupled simulations, which present a more realistic shear at higher heights. In addition, the coupled simulations using the WRF d03 output shows a change in the shear at 150 m in sectors 240° , 270° and 300° . Nevertheless, this cannot be seen in the measurements.

The number of occurrences for unstable and neutral cases is too low in order to draw conclusions (Fig. 11). Especially for the unstable case, where the averaged profile of wind speed does not follow a power law behavior. In the neutral case, the microscale models can reproduce a neutral profile, with the exception of the coupled simulations using the d03 domain. This indicate that the profile obtained from the WRF d03 is not proper, whereas the one from d02 is. This suggest that going from a 3 km resolution to 600 m might not necessarily improve WRF simulation results in a flat area.

In overall, there are differences between the profiles simulated by the coupled and standalone approaches when they are compared to the measurements, depending on the analyzed directional sector. Considerable im-

provements from the coupled approach was obtained in some cases, especially for stable conditions. Nevertheless, the limited improvement is in part expected given the simplicity of the terrain. Flat sites can be easily be modelled different atmospheric stabilities by just adjusting the shear at the inlet (as done in the standalone simulations), as long as there are no complex weather patterns in the site. In addition, as seen in Fig. 9 and Fig. 10, the wind speed profile of some sectors are not properly captured by the WRF simulations.

Coupled simulated profiles show a more realistic shear at higher heights. In the case of the stand-alone simulations, the profiles tend to have a constant shear above 80 meters, whereas in the coupled simulations the shear changes above 150 m. In particular for the stable case, there is a notable increase in the wind shear above 50 meters and a decrease above 150 meters. This is an expected shape for a stable atmosphere. The WRF model reproduces this profile and it is transferred to the microscale simulation through the proposed methodology.

For the directional sectors 0° , 30° , 300° and 330° , the simulated shear presented in Fig. 9 and Fig. 10 is considerably lower than the measured one. This reduced shear is not caused by the wake simulated by the WRF model since the wind farm is situated southwest of the SODAR position. Therefore, measurements could only be affected by the wake when the wind is coming from the directional sectors 180° to 270° (see Fig. 6). A possible explanation is that the WRF simulations do not properly reproduce the average shear of these sectors given their low frequency. In fact, all of these directional sectors have a frequency lower than 8 % (Fig. 8).

4.2 Cross-check prediction errors

In order to quantitatively assess the simulated vertical profiles with respect to the observed data, the sector-wise crosschecking prediction errors (XPE_A) are used. In order to study the performance of the models in the typical context of wind resource assessment, errors are calculated using the measured wind speed by the SODAR at 80 m as a reference and measurements at 120 m which equals the hub height of the turbines (Table 5). It is also of interest to compare the performance of the models at higher heights close to the tip of the turbines. For this reason, errors are also calculated using 120 m as a reference and 200 m as a target (Table 6). As previously discussed, unstable and neutral cases will not be discussed given their low occurrence.

When using 120 m as a target and all stabilities are considered, the coupled simulations forced with the WRF d03 presents slight improvements compared with the standalone approach for sectors 180° to 300° . This improvement has an average of 0.78 % and a maximum for 300° of 1.52 %. Standalone simulations perform significantly better for sectors 30° to 120° . Nevertheless, these sectors correspond to some of the least frequent

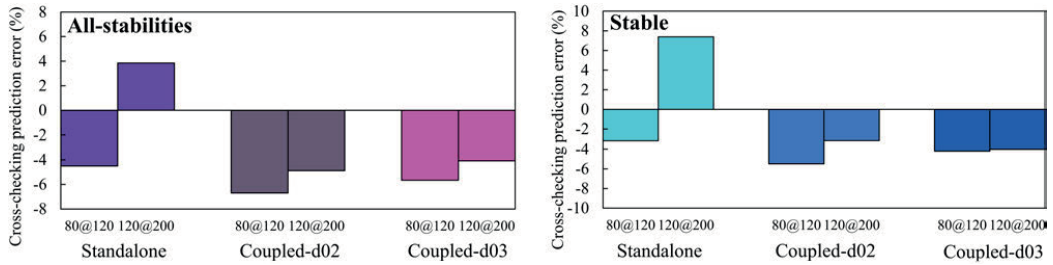


Figure 12: Total crosscheck prediction error. In each panel, the atmospheric stability condition is shown in the top-left corner. X@Y corresponds to the error using X m as reference and Y m as a target measurement.

Table 5: Sectorwise crosschecking prediction error using the wind speed measured by the SODAR at 80 m as a reference and 120 m as a target, for all microscale simulations. Darker colors represent higher frequencies and errors. Model errors are colored in red for over-prediction and in blue for underprediction. SA: standalone, CPd02: coupled with WRF d02 and CPd03: coupled with WRF d03.

Directional sector	Error (%) – all stabilities				Error (%) – stable			
	Freq.	SA	CPd02	CPd03	Freq.	SA	CPd02	CPd03
0	3445	-2.06	-7.02	-2.92	2839	-0.89	-0.14	-3.61
30	3686	-3.97	-9.07	-9.01	3213	-2.34	-8.17	-4.09
180	5778	-5.14	-4.41	-4.48	5432	-3.77	-5.58	-5.92
210	6777	-5.18	-5.75	-4.46	6179	-4.44	-4.26	-5.68
240	5356	-3.08	-2.73	-2.19	4803	-1.89	-3.54	-0.21
270	3853	-2.75	-2.93	-2.63	3443	-1.74	-3.47	1.23
300	4070	-5.72	-6.38	-4.20	3590	-4.42	-6.01	-0.81
330	3093	-4.60	-8.27	-8.07	2521	-3.99	-7.07	-4.05

Table 6: Same as Table 5 but using SODAR measurements at 120 m as reference and 200 m as target.

Directional sector	Error (%) – all stabilities				Error (%) – stable			
	Freq.	SA	CPd02	CPd03	Freq.	SA	CPd02	CPd03
0	2623	9.03	-4.11	-4.71	2063	11.60	-4.46	-3.83
30	2909	6.85	-8.45	-8.22	2399	10.02	-7.56	-9.47
180	4385	2.31	4.72	2.13	4056	6.82	2.45	-0.81
210	6433	0.48	-5.06	1.73	5857	4.49	0.03	0.07
240	5428	2.91	-5.80	-6.16	4783	6.78	-3.01	-1.49
270	3130	5.78	-1.64	-1.66	2753	9.40	0.74	-1.61
300	3091	3.60	-5.33	-4.70	2618	6.59	-3.49	-6.47
330	2468	4.15	-6.64	-6.75	1953	5.55	-5.83	-8.80

ones. Except for sectors 0° and 300°, the coupled simulations do not present important differences when forced by the d02 or the d03 of the WRF. This is consistent with the results presented in the previous subsection.

In the case of stable simulation results, significant differences among models are found for sectors 240°, 270° and 300°. For these sectors, error reductions of 1,7 %, 3 % and 3,6 % were obtained by using coupled simulations forced with the WRF d03 compared with the standalone results. This improvement is also seen when comparing between coupled simulations but with a lower magnitude. In these sectors, the high resolution WRF simulation seems to provide improvements for the coupled approach compared to the low resolution WRF simulation. The opposite happens for sector 30° and 180°, where the standalone simulations show a

better fit to the measurements. The high variability in the performance of the coupled simulations indicates that the simulated shear by the WRF model between 80 and 120 m is very well reproduced in some sectors and very off for some others.

When using 200 m as a target and 120 m as reference, the performance of the models depends on the atmospheric stability. When all stabilities are considered, the overall performance of the models is similar. Nevertheless, for some individual sectors these differences can be significant. For example, in sectors 0° and 270° the both coupled models have an error reduction of about 4 %. The opposite happens in sectors 240° and 330° where the standalone model performs about 3 % better than the coupled one. The dependence of the model performances with the sectors indicates that the average shear might be modeled wrong for few sectors in the WRF simulations.

For stable simulations, the coupled models have the best overall performance. When the CFD is forced by the d02 of the WRF model, the error is on average reduced by 4.3 %, with a maximum reduction of 8.7 % in sector 270°. When forced with d03, the average error reduction is 4,1 % with a maximum reduction of 7.8 %, also in sector 270°. Despite the coupled models perform similarly, the sector in which they perform better are different. It is interesting to note that standalone simulations overpredict the wind for all directional sectors while the opposite happens for the coupled approaches. This reflects the limitation of the near-to-constant shear simulated by the standalone model. Since the shear is not reduced at higher heights (as in the coupled model) the wind is overpredicted.

In order to compare the overall performance of the models, the $XPE(R, T)$ are presented in Fig. 12. Overall, the standalone model performs about 2 % better than the coupled model at heights below 120 m. For heights above 120 m, both approaches perform similar when all stabilities are considered. If only stable cases are taken into account, then the coupled models perform about 4 % better. Given the shape of the profiles shown in Section 4.1, it is expected that the use of higher heights as reference give a better result for the coupled models. The reason is that in the coupled models the

shear is better represented at higher heights, while in the lower heights the opposite occurs.

The improvement of using d03 instead of d02 is rather small. Therefore, there is no need to increase the resolution of the WRF model, if the objective is to obtain averaged profiles in a flat site. It is important to note that these metrics serve to evaluate the simulated vertical profiles only for the heights for which measurements are available. It does not take into account the wind flow at higher heights, nor the validity of horizontal flow patterns what will be discussed in Section 4.3.

4.3 Horizontal wind speed patterns

In addition to different simulated vertical profiles of horizontal wind speed, it is expected that different boundary conditions produce different horizontal wind speed patterns. In order to compare such patterns, the 120 m horizontal wind speed of sector 210° is presented for the whole domain for the standalone, coupled and WRF models (Fig. 13). In order to facilitate the comparison of the speed up factors, the wind speeds are normalized by the wind speed at the lower left corner of the domain. For the microscale simulations, no wake is visible as it is not explicitly resolved in the CFD model. Only in the domain d03 of the WRF model it is visible. Nevertheless, it has no effect in the coupled CFD results. When wake calculations are needed in the microscale (as in Section 4.4) analytical formulas were used.

The patterns are quite different between the coupled and standalone simulations. In both approaches, for all stabilities, neutral and stable cases, there is a decrease of the wind speed in the downstream side of the domain. In the coupled simulations, the decrease is much stronger than in the standalone model. This higher decrease in the coupled simulations is due to increased turbulence around 120 m in that area caused by the forest. Differences in simulated turbulence is affected from a series of factors like friction velocity, boundary layer height and atmospheric stability.

It is expected that different stability conditions will generate different wind patterns. The coupled simulation presents such dependency, when comparing the unstable case with the stable or neutral ones. Such dependency is not seen in the standalone case, whose patterns have similar shape, despite the values of the increase and decrease of the wind speed varies.

Given the low resolution of the WRF model, their simulations do not present the microscale flow features seen in the CFD models. In the later, small speed up areas matching the elevation of the terrain can be seen scattered in the domain. Nevertheless, given the lack of measurements located at different positions inside the CFD simulation domain, it is not possible to validate such features. Also, it is not possible to evaluate which of the microscale models have a better representation of them. Finally, there are no major differences in the patterns generated by the coupled simulations forced by the domains d02 or d03 of the WRF model. As discussed

in Sections 4.1 and 4.2, this indicates that there is no need to use resolutions higher than 3 km in non-complex areas.

4.4 Energy production

The CFD results are used to estimated energy production of the Honkajoki wind farm. The production is estimated by transferring a reference measurement to the positions of the wind turbines (see Figure 7). The frequency distribution of the transferred wind speeds is translated into energy output through the power curve presented in Fig. 14. The power curve is based on the turbine model Nordex N117/2400 with a hub height of 120 m. Wake losses are estimated using Jensen's analytical wake model (KATIC et al., 1987) which uses as input the drag coefficient presented in Fig. 14.

The transferred wind speeds are calculated by using the speed-up ratios obtained from the standalone and coupled results. The models that considers only one atmospheric stability are only valid for measurements with that stability. Therefore, to compare them with the all-stabilities cases, their estimated energy production is weighted averaged by their frequency. As before, the SODAR at 80 m was used as a reference measurement to compute the speed-up ratios. The capacity factor estimated for each model is presented in Fig. 15.

The estimated production, as well as the wake losses, are very similar among the standalone and coupled simulations. The main reason is that the energy production calculation is based on the SODAR at 80 m. This measurement is first vertically extrapolated to 120 m and then horizontally extrapolated to the turbine positions. As seen in Section 4.2, the speed-up ratio from 80 m to 120 m at the SODAR position is not that different among models. The same is expected for the horizontal speed-ups since the terrain is flat. Given these conditions, it is also expected that the estimated energy production is relatively similar.

5 Conclusions

The performance of coupled simulations depends on the studied atmospheric stability and directional sector. When all stabilities are considered, the coupled model forced by the d03 of the WRF model perform similarly to the standalone simulations. In the case of stable conditions, the coupled simulation have an error reduction of 4 % for heights above 120 m. When the coupled model was forced with the d02 of the WRF model instead, the improvement in the stable case was similar for these heights. Nevertheless, the standalone performed 1.5 % better when all stabilities taken into account. These differences did not have a big effect in the estimated energy production.

The shear obtained from the coupled models at higher heights tends to be more realistic. The reason is

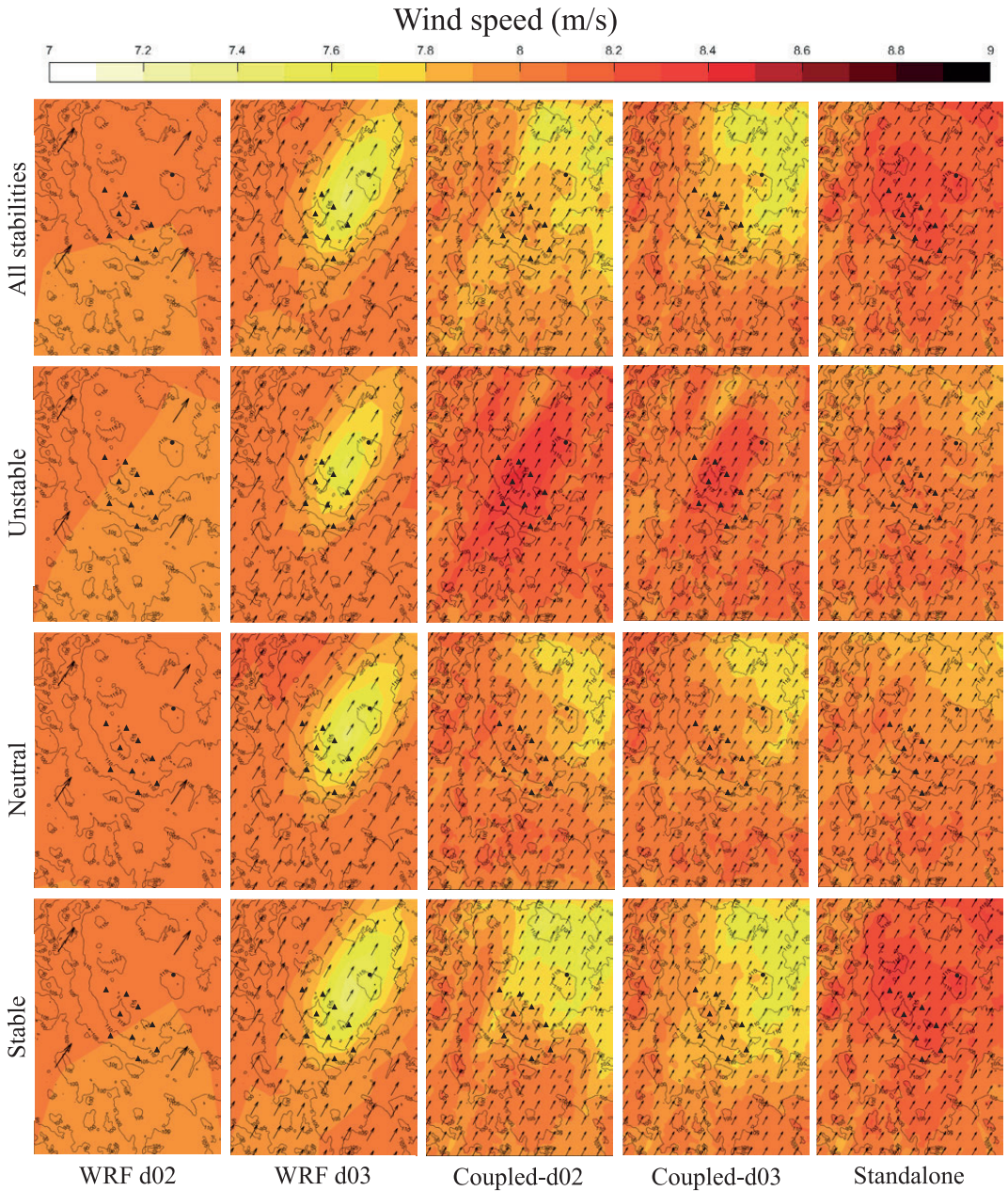


Figure 13: Simulated wind speed patterns for directional sector 210° at 120 m above ground. The corresponding atmospheric stability and type of simulation is indicated at the left and bottom side of the figure, respectively. Values are normalized by the simulated wind speed at the lower left corner and multiplied by 8 m/s. In all panels, the contours of the CFD elevation is displayed as black lines with a number indicating their elevation in meters. The black arrows indicate the direction of the wind for that node in the simulation. For CFD simulations, some arrows were skipped for visualization purposes. The position of the wind turbines are indicated with black triangles and the position of the SODAR with a black dot.

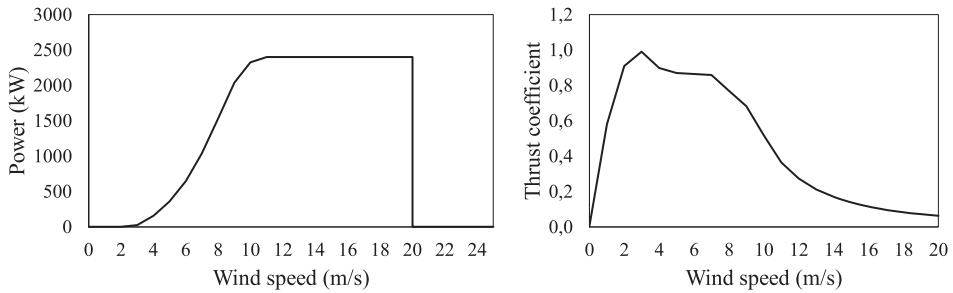
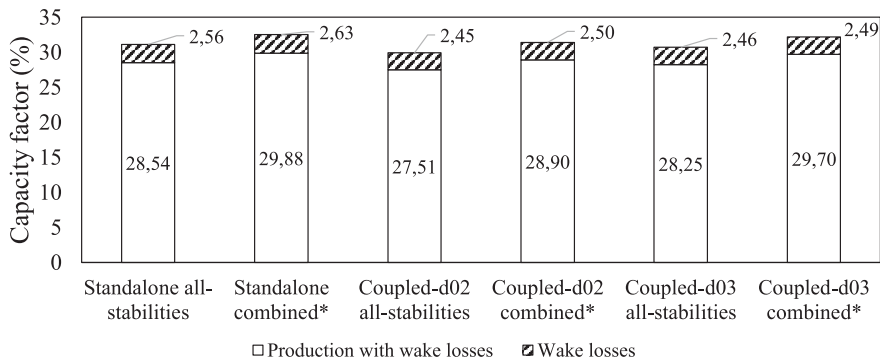


Figure 14: Power curve (left) and thrust coefficient (right) for the Nordex N117/2400 turbine with an air density of 1.225 kg/m^3 .



*weighted average of unstable, neutral and stable simulations

Figure 15: Estimated production of the Honkajoki wind farm by the standalone and coupled models, using the SODAR at 80 m as a reference measurement.

that WRF simulations provide information about the local atmospheric conditions in the area. This is more advantageous than the standalone approach that assumes Monin-Obukhov similarity theory all the way up in the boundary layer and constant wind speed above. This characteristic of the coupled profiles is very important as the trend is that wind turbine hub heights get higher for wind project development.

It is possible to further improve standalone simulations by tuning the parameters which are used to prescribe the boundary condition. For example, to get higher shear, the Monin-Obukhov length could be reduced, the boundary layer height could be lowered, the geostrophic wind could be increased, or a combination of these. The proposed methodology skips this tuning, preventing a subjective choice of such variables by indirectly including them in the shapes of the wind speed and temperature profiles interpolated from the WRF domain. Furthermore, such tweaking could only be conducted to match just one measurement position at the time, which does not guaranty a match for other positions.

Since the terrain of the modelled site is flat, it is expected that the CFD results depend mostly on the

boundary conditions. This implies that any deviation in the WRF model results will have a big influence in the microscale results. The reason is that the corrections done by the microscale model are limited given that the orography does not play an important role, and only forest and roughness length changes influence the wind. For some directional sectors the averaged WRF simulated profile is not able to reproduce the shear seen in the measurements. These are the same sectors in which the coupled simulations have a lower performance. It is noted that this mainly happens in the least frequent directional sectors. This might indicate that in order to have on average a good reproduction of the shear in the WRF simulations, a relatively high frequency of occurrence is needed.

Independent of the results in terms of the vertical profiles, one of the expected gains from coupling with mesoscale models is to obtain more realistic horizontal wind patterns. In fact, in Section 4.3 was shown that the horizontal wind patterns are different between coupled and standalone models. Unfortunately, only the vertical profiles of horizontal wind speed of the CFD models could be validated due to the lack of observational data at different position than the SODAR. Even hav-

ing a good modelling of the vertical profiles, it is still possible to have poor horizontal modelling of the wind. Therefore, the methodology will now be applied to sites which have several measurement masts to understand the added value of the coupled simulations for simulating the horizontal wind speed patterns.

The results between the coupled models using the results from the WRF domains d02 and d03 are not significantly different. In the case of the vertical profiles, the results are similar for most sectors. Small differences can be found in few sectors, but any of the models performs consistently better. In the case of the horizontal patterns, the similarities are also high. Few differences can be found in some small pockets of the domain, but the overall pattern is the same. This result suggests that there is not an important gain in using higher resolutions in the WRF model when the terrain is flat. Nevertheless, in the case of complex sites, it is expected that such high resolutions are required to properly represent the topography, land use and small-scale flow features in the boundary layer.

Acknowledgments

This research was supported by a grant from The Norwegian Research Council, project number 271080. We acknowledge Botnia-Atlantica, an EU-programme financing cross border cooperation projects in Sweden, Finland and Norway, for their support of this work through the WindCoE project. We would like to thank the High Performance Computing Center North (HPC2N) for providing the computer resources needed to perform the numerical experiments presented in this paper. We would also like to thank the two anonymous reviewers for their useful comments.

References

- AL-YAHHYI, S., Y. CHARABI, A. GASTLI, 2010: Review of the use of numerical weather prediction (NWP) models for wind energy assessment. – *Ren. Sustain. Energy Rev.* **14**, 3192–3198, DOI: [10.1016/j.rser.2010.07.001](https://doi.org/10.1016/j.rser.2010.07.001).
- AL-YAHHYI, S., Y. CHARABI, A. AL-BADI, A. GASTLI, 2012: Nested ensemble NWP approach for wind energy assessment. – *Ren. Energy* **37**, 150–160, DOI: [10.1016/j.renene.2011.06.014](https://doi.org/10.1016/j.renene.2011.06.014).
- ARYA, S.P., 1998: Introduction to Micrometeorology, 2nd ed. – San Diego: Academic Press.
- BACHANT, P., M. WOSNIK, 2016: Effects of Reynolds Number on the Energy Conversion and Near-Wake Dynamics of a High Solidity Vertical-Axis Cross-Flow Turbine. – *Energies* **9**, 73, DOI: [10.3390/en9020073](https://doi.org/10.3390/en9020073).
- BADGER, J., H. FRANK, A.N. HAHMANN, G. GIEBEL, 2014: Wind-climate estimation based on mesoscale and microscale modeling: Statistical-dynamical downscaling for wind energy applications. – *J. Appl. Meteor. Climatol.* **53**, 1901–1919, DOI: [10.1175/JAMC-D-13-0147.1](https://doi.org/10.1175/JAMC-D-13-0147.1).
- BAIK, J., S. PARK, J. KIM, 2009: Urban Flow and Dispersion Simulation Using a CFD Model Coupled to a Mesoscale Model. – *J. Appl. Meteor. Climatol.* **48**, 1667–1681, DOI: [10.1175/2009JAMC2066.1](https://doi.org/10.1175/2009JAMC2066.1).
- BERG, J., J. MANN, A. BECHMANN, M.S. COURTNEY, H.E. JØRGENSEN, 2011: The Bolund Experiment, Part I: Flow Over a Steep, Three-Dimensional Hill. – *Bound.-Layer Meteor.* **141**, 219–243, DOI: [10.1007/s10546-011-9636-y](https://doi.org/10.1007/s10546-011-9636-y).
- BILAL, M., Y. BIRKELUND, M. HOMOLA, M. VIRK, 2016a: Wind over complex terrain – Microscale modelling with two types of mesoscale winds at Nygårdsfjell. – *Ren. Energy* **99**, 647–653, DOI: [10.1016/j.renene.2016.07.042](https://doi.org/10.1016/j.renene.2016.07.042).
- BILAL, M., K. SOLBAKKEN, Y. BIRKELUND, 2016b: Wind speed and direction predictions by WRF and WindSim coupling over Nygårdsfjell. – *J. Physics: Conference Series* **753**, 082018, DOI: [10.1088/1742-6596/753/8/082018](https://doi.org/10.1088/1742-6596/753/8/082018).
- BOUTANIOS, Z., C. MILLER, H. HANGAN, 2010: Computational analysis of the Manitoba September 5 1996 Storm: mesoscale WRF-ARW simulations coupled with microscale OpenFOAM CFD simulations. – In: *The Fifth International Symposium on Computational Wind Engineering*.
- BUSCH, K., 2017: Application and Validation of the Forest Model inside WindSim CFD Software resp. Phoenix with the new GCV solver. – Master Thesis. Carl von Ossietzky Universität Oldenburg.
- BUSINGER, J.A., J.C. WYNGAARD, Y. IZUMI, E.F. BRADLEY, 1971: Flux-Profile Relationships in the Atmospheric Surface Layer. – *J. Atmos. Sci.*, published online, DOI: [10.1175/1520-0469\(1971\)028<0181:Fpita>2.0.CO;2](https://doi.org/10.1175/1520-0469(1971)028<0181:Fpita>2.0.CO;2).
- CARVALHO, D., A. ROCHA, C. SILVA SANTOS, R. PEREIRA, 2013: Wind resource modelling in complex terrain using different mesoscale–microscale coupling techniques. – *Appl. Energy* **108**, 493–504, DOI: [10.1016/j.apenergy.2013.03.074](https://doi.org/10.1016/j.apenergy.2013.03.074).
- CASTELLANI, F., C. BUSILLO, F. CALASTRINI, G. GUALTIERI, G. MOLINA, L. TERZI, 2006: An hybrid approach for downscaling RAMS data for Wind Resource Assessment in Complex Terrains. – In: *European Wind Energy Conference*, 1–4.
- CASTRO, F.A., C. SILVA SANTOS, J.C. LOPES DA COSTA, 2015: One-way mesoscale-microscale coupling for the simulation of atmospheric flows over complex terrain. – *Wind Energy* **18**, 1251–1272, DOI: [10.1002/we.1758](https://doi.org/10.1002/we.1758).
- CHEN, F., J. DUDHIA, 2001: Coupling an Advanced Land Surface-Hydrology Model with the Penn State-NCAR MM5 Modeling System. Part II: Preliminary Model Validation. – *Mon. Wea. Rev.* **129**, 587–604, DOI: [10.1175/1520-0493\(2001\)129<0587:Caalsh>2.0.CO;2](https://doi.org/10.1175/1520-0493(2001)129<0587:Caalsh>2.0.CO;2).
- CSISZAR, I., G. GUTMAN, 1999: Mapping global land surface albedo from NOAA AVHRR. – *J. Geophys. Res. Atmos.* **104**, 6215–6228, DOI: [10.1029/1998JD200090](https://doi.org/10.1029/1998JD200090).
- DURASAMY, V.J., 2014: Downscaling wind energy resource from mesoscale to local scale by nesting and data assimilation with a CFD model. – PhD Thesis. University of Paris-Est.
- DURASAMY, V.J., E. DUPONT, B. CARISSIMO, 2014: Downscaling wind energy resource from mesoscale to microscale model and data assimilating field measurements. – *J. Physics: Conference Series* **555**, 012031, DOI: [10.1088/1742-6596/555/1/012031](https://doi.org/10.1088/1742-6596/555/1/012031).
- DYER, A.J., 1974: A review of flux-profile relationships. – *Bound.-Layer Meteor.* **7**, 363–372, DOI: [10.1007/BF00240838](https://doi.org/10.1007/BF00240838).
- FITCH, A.C., J.B. OLSON, J.K. LUNDQUIST, J. DUDHIA, A.K. GUPTA, J. MICHALAKES, I. BARSTAD, 2012: Local and Mesoscale Impacts of Wind Farms as Parameterized in a Mesoscale NWP Model. – *Mon. Wea. Rev.* **140**, 3017–3038, DOI: [10.1175/MWR-D-11-00352.1](https://doi.org/10.1175/MWR-D-11-00352.1).
- FOLCH, A., J. BARCONS, T. KOZONO, A. COSTA, 2016: High-resolution modeling of atmospheric dispersion of dense gas using Twodee-2. 1: application to the 1986 Lake Nyos limnic eruption. (December). – *Nat. Hazards Earth Syst. Sci.* **17**, 861–879, DOI: [10.5194/nhess-2016-343](https://doi.org/10.5194/nhess-2016-343).

- GARRATT, J.R., 1992: The atmospheric boundary layer. – Cambridge, UK: Cambridge University Press.
- GOPALAN, H., C. GUNDLING, K. BROWN, B. ROGET, J. SITARAMAN, J.D. MIROCHA, W.O. MILLER, 2014: A coupled mesoscale-microscale framework for wind resource estimation and farm aerodynamics. – *J. Wind Enginer. Indust. Aerodyn.* **132**, 13–26, DOI: [10.1016/j.jweia.2014.06.001](https://doi.org/10.1016/j.jweia.2014.06.001).
- GRAVDAHL, A.R., 1998: Meso Scale Modeling with a Reynolds Averaged Navier-Stokes Solver Assessment of wind resources along the Norwegian coast. – In: 31st IEA Experts Meeting State of the Art on Wind Resource Estimation, 1–14. Risø, Denmark.
- GUTMAN, G., A. IGNATOV, 1998: The derivation of the green vegetation fraction from NOAA/Avhrr data for use in numerical weather prediction models. – *Int. J. Remote Sens.* **19**, 1533–1543, DOI: [10.1080/014311698215333](https://doi.org/10.1080/014311698215333).
- HAN, J., S.P. ARYA, S. SHEN, Y. LIN, 2000: An Estimation and Energy Atmospheric Theory of Turbulent Dissipation Boundary Kinetic Energy Rate Based on Layer Similarity. – NASA technical report. Hampton, Virginia.
- HINES, K.M., D.H. BROMWICH, 2008: Development and Testing of Polar Weather Research and Forecasting (WRF) Model. Part I: Greenland Ice Sheet Meteorology*. – *Mon. Wea. Rev.* **136**, 1971–1989, DOI: [10.1175/2007MWR2112.1](https://doi.org/10.1175/2007MWR2112.1).
- HRISTOV, Y., G. OXLEY, M. ŽAGAR, 2014: Improvement of AEP Predictions Using Diurnal CFD Modelling with Site-Specific Stability Weightings Provided from Mesoscale Simulation. – *J. Physics: Conference Series* **524** (Torque), 012116, DOI: [10.1088/1742-6596/524/1/012116](https://doi.org/10.1088/1742-6596/524/1/012116).
- IACONO, M.J., J.S. DELAMERE, E.J. MLAWER, M.W. SHEPHARD, S.A. CLOUGH, W.D. COLLINS, 2008: Radiative forcing by long-lived greenhouse gases: Calculations with the AER radiative transfer models. – *J. Geophys. Res. Atmos.* **113**, 2–9, DOI: [10.1029/2008JD009944](https://doi.org/10.1029/2008JD009944).
- JANJIĆ, Z.I., 1994: The Step-Mountain Eta Coordinate Model: Further Developments of the Convection, Viscous Sublayer, and Turbulence Closure Schemes. – *Mon. Wea. Rev.* **122**, 927–945, DOI: [10.1175/1520-0493\(1994\)122<0927:Tsmecm>2.0.CO;2](https://doi.org/10.1175/1520-0493(1994)122<0927:Tsmecm>2.0.CO;2).
- KATIC, I., J. HØJSTRUP, N.O. JENSEN, 1987: A Simple Model for Cluster Efficiency. – EWEC'86. Proceedings 407–410.
- KINBARA, K., S. IZUKA, M. KUROKI, A. KONDO, 2010: Merging WRF and LES models for the analysis of a wind environment in an urban area. – In: The Fifth Symposium Computational Wind Engineering.
- KOH, T., R. FONSECA, 2016: Subgrid-scale cloud-radiation feedback for the Betts-Miller-Janjić convection scheme. – *Quart. J. Roy. Meteor. Soc.* **142**, 989–1006, DOI: [10.1002/qj.2702](https://doi.org/10.1002/qj.2702).
- LEBLEBICI, E., I. TUNCER, 2015: Wind Power Estimations using OpenFoam Coupled with WRF. – In: 11th EAWE PhD Seminar on Wind Energy in Europe.
- LEBLEBICI, E., G. AHMET, I. TUNCER, 2014: CFD Coupled with WRF for Wind Power Prediction. – In: 10th PhD Seminar on Wind Energy in Europe. Orléans.
- LI, L., F. HU, J. JIANG, X. CHENG, 2007: An application of the RAMS/Fluent system on the multi-scale numerical simulation of the urban surface layer -A preliminary study. – *Adv. Atmos. Sci.* **24**, 271–280, DOI: [10.1007/s00376-007-0271-y](https://doi.org/10.1007/s00376-007-0271-y).
- LI, L., L. ZHANG, N. ZHANG, F. HU, Y. JIANG, C. XUAN, W. JIANG, 2010: Study on the Micro-scale simulation of wind field over complex terrain by RAMS / Fluent modeling system. – The Fifth International Symposium on Computational Wind Engineering (CWE2010) 2(5), 411–418, DOI: [10.3724/SP.J.1226.2010.00411](https://doi.org/10.3724/SP.J.1226.2010.00411).
- LIU, Y., T. WARNER, Y. LIU, C. VINCENT, W. WU, B. MAHONEY, S. SWERDLIN, K. PARKS, J. BOEHNERT, 2011: Simultaneous nested modeling from the synoptic scale to the LES scale for wind energy applications. – *J. Wind Enginer. Indust. Aerodyn.* **99**, 308–319, DOI: [10.1016/j.jweia.2011.01.013](https://doi.org/10.1016/j.jweia.2011.01.013).
- LIU, Y.S., S.G. MIAO, C.L. ZHANG, G.X. CUI, Z.S. ZHANG, 2012: Study on micro-atmospheric environment by coupling large eddy simulation with mesoscale model. – *J. Wind Enginer. Indust. Aerodyn.* **107**, 106–117, DOI: [10.1016/j.jweia.2012.03.033](https://doi.org/10.1016/j.jweia.2012.03.033).
- LO, J.C., Z. YANG, R.A. PIELKE, 2008: Assessment of three dynamical climate downscaling methods using the Weather Research and Forecasting (WRF) model. – *J. Geophys. Res.* **113**, D09112, DOI: [10.1029/2007JD009216](https://doi.org/10.1029/2007JD009216).
- LOVELAND, T.R., B.C. REED, J.F. BROWN, D.O. OHLEN, Z. ZHU, L. YANG, J.W. MERCHANT, 2000: Development of a global land cover characteristics database and IGBP DISCover from 1 km Avhrr data. – *Int. J. Remote Sens.* **21**, 1303–1330, DOI: [10.1080/014311600210191](https://doi.org/10.1080/014311600210191).
- LUNDQUIST, J.K., J.D. MIROCHA, B. KOSOVIC, 2008: Nesting large-eddy simulations within mesoscale simulations in WRF for wind energy applications. – In: AGU Fall Meeting Abstracts **6**.
- MEISSNER, C., A.R. GRAVDAHL, B. STEENSEN, 2009: Including Thermal Effects in CFD Wind Flow Simulations. – *J. Env. Sci. Int.* **18**, 833–839, DOI: [10.5322/JES.2009.18.8.833](https://doi.org/10.5322/JES.2009.18.8.833).
- MEISSNER, C., M. MANA, J. GENTLE, C.G. NUNALEE, 2015: Coupling of mesoscale and microscale models for wind resource assessment and wind power forecasting. – ????
- MIAO, Y., S. LIU, B. CHEN, B. ZHANG, S. WANG, S. LI, 2013: Simulating urban flow and dispersion in Beijing by coupling a CFD model with the WRF model. – *Adv. Atmos. Sci.* **30**, 1663–1678, DOI: [10.1007/s00376-013-2234-9](https://doi.org/10.1007/s00376-013-2234-9).
- MIROCHA, J., G. KIRKIL, 2010: Nested high-resolution mesoscale / large eddy simulations in WRF: challenges and opportunities. – In: The Fifth International Symposium on Computational Wind Engineering (CWE2010). Chapel Hill, North Carolina, USA.
- MIROCHA, J., G. KIRKIL, E. BOU-ZEID, F.K. CHOW, B. KOSOVIC, 2013: Transition and Equilibration of Neutral Atmospheric Boundary Layer Flow in One-Way Nested Large-Eddy Simulations Using the Weather Research and Forecasting Model. – *Mon. Wea. Rev.* **141**, 918–940, DOI: [10.1175/MWR-D-11-00263.1](https://doi.org/10.1175/MWR-D-11-00263.1).
- MIROCHA, J., B. KOSOVIC, G. KIRKIL, 2014: Resolved Turbulence Characteristics in Large-Eddy Simulations Nested within Mesoscale Simulations Using the Weather Research and Forecasting Model. – *Mon. Wea. Rev.* **142**, 806–831, DOI: [10.1175/MWR-D-13-00064.1](https://doi.org/10.1175/MWR-D-13-00064.1).
- MOENG, C., J. DUDHIA, J. KLEMP, P. SULLIVAN, 2007: Examining Two-Way Grid Nesting for Large Eddy Simulation of the PBL Using the WRF Model. – *Mon. Wea. Rev.* **135**, 2295–2311, DOI: [10.1175/MWR3406.1](https://doi.org/10.1175/MWR3406.1).
- MONIN, A.S., A.M. OBUKHOV, 1954: Basic laws of turbulent mixing in the surface layer of the atmosphere. – *Contrib. Geophys. Inst. Acad. Sci. USSR* **24**, 163–187.
- MUÑOZ-ESPARZA, D., B. KOSOVIC, J. MIROCHA, J. VAN BEECK, 2014: Bridging the Transition from Mesoscale to Microscale Turbulence in Numerical Weather Prediction Models. – *Bound.-Layer Meteor.* **153**, 409–440, DOI: [10.1007/s10546-014-9956-9](https://doi.org/10.1007/s10546-014-9956-9).
- MURAKAMI, S., A. MOCHIDA, S. KATO, 2003: Development of local area wind prediction system for selecting suitable site for windmill. – *J. Wind Enginer. Indust. Aerodyn.* **91**, 1759–1776, DOI: [10.1016/j.jweia.2003.09.040](https://doi.org/10.1016/j.jweia.2003.09.040).
- NAKANISHI, M., H. NIINO, 2004: An improved Mellor-Yamada Level-3 model with condensation physics: Its design and verification. – *Bound.-Layer Meteor.* **112**, 1–31, DOI: [10.1023/B:BOUN.0000020164.04146.98](https://doi.org/10.1023/B:BOUN.0000020164.04146.98).

- NAKANISHI, M., H. NIINO, 2006: An improved Mellor-Yamada Level-3 model: Its numerical stability and application to a regional prediction of advection fog. – *Bound Layer Meteor.* **119**, 397–407, DOI: [10.1007/s10546-005-9030-8](https://doi.org/10.1007/s10546-005-9030-8).
- NAKAYAMA, H., T. TAKEMI, H. NAGAI, 2011: Coupling of WRF and building-resolving urban CFD models for analysis of strong winds over an urban area. – In: 14th Conference on Mesoscale Processes.
- NOZU, T., T. KISHIDA, T. TAMURA, Y. OKUDA, H. UMAKAWA, 2009: LES of wind turbulence and heat environment around dense tall buildings. – In: *Eucwe* **5**, 1–10, Florence, Italy.
- SAHA, S., S. MOORTHY, H. PAN, X. WU, J. WANG, S. NADIGA, P. TRIPP, R. KISTLER, J. WOOLLEN, D. BEHRINGER, H. LIU, D. STOKES, R. GRUMBINE, G. GAYNO, J. WANG, Y. HOU, H. CHUANG, H. JUANG, J. SELA, M. IREDELL, R. TREADON, D. KLEIST, P. VAN DELST, D. KEYSER, J. DERBER, M. EK, J. MENG, H. WEI, R. YANG, S. LORD, H. VAN DEN DOOL, A. KUMAR, W. WANG, C. LONG, M. CHELLIAH, Y. XUE, B. HUANG, J. SCHEMM, W. EBISUZAKI, R. LIN, P. XIE, M. CHEN, S. ZHOU, W. HIGGINS, C. ZOU, Q. LIU, Y. CHEN, Y. HAN, L. CUCURULL, R.W. REYNOLDS, G. RUTLEDGE, M. GOLDBERG, 2010: The NCEP Climate Forecast System Reanalysis. – *Bull. Amer. Meteor. Soc.* **91**, 1015–1058, DOI: [10.1175/2010BAMS3001.1](https://doi.org/10.1175/2010BAMS3001.1).
- SANZ RODRIGO, J., B. GARCÍA, D. CABEZÓN, S. LOZANO, I. MARTÍ, 2010: Downscaling mesoscale simulations with CFD for high resolution regional wind mapping. – In: European Wind Energy Conference EWEC-2010, Warsaw.
- SANZ RODRIGO, J., R.A. CHÁVEZ ARROYO, P. MORIARTY, M. CHURCHFIELD, B. KOSOVIC, P.E. RÉTHORÉ, K. HANSEN, A. HAHMANN, J. MIROCHA, D. RIFE, 2017a: Mesoscale to microscale wind farm flow modeling and evaluation. – *Wiley Interdisciplinary Revs. Energy Env.* **6**, DOI: [10.1002/wene.214](https://doi.org/10.1002/wene.214).
- SANZ RODRIGO, J., M. CHURCHFIELD, B. KOSOVIC, 2017b: A methodology for the design and testing of atmospheric boundary layer models for wind energy applications. – *Wind Energy Sci.* **2**, 35–54, DOI: [10.5194/wes-2-35-2017](https://doi.org/10.5194/wes-2-35-2017).
- SCHNEIDERBAUER, S., S. PIRKER, 2010: Resolving unsteady micro-scale atmospheric flows by nesting a CFD simulation into wide range numerical weather prediction models. – *Int. J. Comput. Fluid Dyn.* **24**, 51–68, DOI: [10.1080/10618562.2010.483227](https://doi.org/10.1080/10618562.2010.483227).
- SITARAMAN, J., 2013: Simulation of Wind Turbine Performance and Loading Patterns using a Coupled Meso-scale/Microscale Flow Analysis Model. – Technical report, <https://e-reports-ext.llnl.gov/pdf/765731.pdf>
- SITARAMAN, J., H. GOPALAN, C. GUNDLING, J. MIROCHA, W. MILLER, 2013: Coupled Mesoscale Microscale Model for Wind Resource Estimation and Turbine Aerodynamics Using an Overset Grid Approach. – In: 51st AIAA Aerospace Sciences Meeting including the New Horizons Forum and Aerospace Exposition, 1–23, Reston, Virginia: American Institute of Aeronautics and Astronautics, DOI: [10.2514/6.2013-1209](https://doi.org/10.2514/6.2013-1209).
- SKAMAROCK, W.C., J.B. KLEMP, J. DUDHI, D.O. GILL, D.M. BARKER, M.G. DUDA, X. HUANG, W. WANG, J.G. POWERS, 2008: A Description of the Advanced Research WRF Version 3. – NCAR Technical Note NCAR/TN-468+STR, DOI: [10.5065/D6DZ069T](https://doi.org/10.5065/D6DZ069T).
- SOLAZZO, E., A. DUDEK, S. OXIZIDIS, R. BRITTER, T.E. NORDENG, 2006: From meso-scale to street-scale: a downscaling procedure using statistical and CFD models. The Lisbon case study. – In: 6th International Conference on Urban Climate. Göteborg.
- SUTTON, O.G., 1949: *Atmospheric Turbulence*. London, Methuen, 115 pp.
- TAKEMI, T., T. TAMURA, Y. TAKEI, Y. OKUDA, 2006: Microscale analysis of severe winds within the urban canopy during a period of explosive cyclogenesis by coupling large-eddy simulation and mesoscale meteorological models. – In: The Fourth International Symposium on Computational Wind Engineering, 16–19, Yokohama.
- TAO, W., J. SIMPSON, M. MCCUMBER, 1989: An Ice-Water Saturation Adjustment. – *Mon. Wea. Rev.*, published online, DOI: [10.1175/1520-0493\(1989\)117<0231:Aiwsa>2.0.CO;2](https://doi.org/10.1175/1520-0493(1989)117<0231:Aiwsa>2.0.CO;2).
- TEGEN, I., P. HOLLRIG, M. CHIN, I. FUNG, D. JACOB, J. PENNER, 1997: Contribution of different aerosol species to the global aerosol extinction optical thickness: Estimates from model results. – *J. Geophys. Res. Atmos.* **102**, D20, 23895–23915, DOI: [10.1029/97JD01864](https://doi.org/10.1029/97JD01864).
- VEIGA RODRIGUES, C., J.M.L.M. PALMA, 2014: Estimation of turbulence intensity and shear factor for diurnal and nocturnal periods with an Urans flow solver coupled with WRF. – *J. Physics: Conference Series* **524**, 012115, DOI: [10.1088/1742-6596/524/1/012115](https://doi.org/10.1088/1742-6596/524/1/012115).
- VEIGA RODRIGUES, C., M. SILVA SANTOS, J.M.L.M. PALMA, F.A. CASTRO, P.M.A. MIRANDA, A.H. RODRIGUES, 2008: Short-term Forecasting of a Wind Farm Output using CFD. – In: European Wind Energy Conference and Exhibition 2008, Brussels.
- VEIGA RODRIGUES, C., J.M.L.M. PALMA, Á.H. RODRIGUES, 2016: Atmospheric Flow over a Mountainous Region by a One-Way Coupled Approach Based on Reynolds-Averaged Turbulence Modelling. – *Bound.-Layer Meteor.* **159**, 407–437, DOI: [10.1007/s10546-015-0116-7](https://doi.org/10.1007/s10546-015-0116-7).
- WANG, J., R.M. FONSECA, K. RUTLEDGE, J. MARTÍN-TORRES, J. YU, 2019: Weather Simulation Uncertainty Estimation Using Bayesian Hierarchical Models. – *J. Appl. Meteor. Climatol.* **58**, 585–603, DOI: [10.1175/JAMC-D-18-0018.1](https://doi.org/10.1175/JAMC-D-18-0018.1).
- WHARTON, S., J.K. LUNDQUIST, 2012: Assessing atmospheric stability and its impacts on rotor-disk wind characteristics at an onshore wind farm. – *Wind Energy* **15**, 525–546, DOI: [10.1002/we.483](https://doi.org/10.1002/we.483).
- YAMAGUCHI, A., T. ISHIHARA, Y. FUJINO, 2002: Applicability of Linear and Nonlinear Wind Prediction Models To Wind Flow in Complex Terrain. – In: The World Wind Energy Conference and Exhibition, Berlin.
- YU, W., R. BENOIT, C. GIRARD, A. GLAZER, D. LEMARQUIS, J.R. SALMON, J.-P. PINARD, 2006: Wind Energy Simulation Toolkit (WEST): A Wind Mapping System for Use by the WindEnergy Industry. *Wind Engineer.* **30**, published online, DOI: [10.1260/030952406777641450](https://doi.org/10.1260/030952406777641450).
- ZHENG, Y., Y. MIAO, S. LIU, B. CHEN, H. ZHENG, S. WANG, 2015: Simulating flow and dispersion by using WRF-CFD coupled model in a built-up area of Shenyang, China. – *Adv. Meteor.* **2015**, 528618, DOI: [10.1155/2015/528618](https://doi.org/10.1155/2015/528618).

Paper II

RESEARCH ARTICLE

Automated classification of simulated wind field patterns from multiphysics ensemble forecasts

Pablo Durán^{1,2}  | Sukanta Basu³  | Cathérine Meißner² | Muyiwa S. Adaramola¹ 

¹Faculty of Environmental Sciences and Natural Resource Management, Norwegian University of Life Sciences, Ås, Norway

²Software Development, WindSim AS, Tønsberg, Norway

³Faculty of Civil Engineering and Geosciences, Delft University of Technology, Delft, The Netherlands

Correspondence

Pablo Durán, Faculty of Environmental Sciences and Natural Resource Management, Norwegian University of Life Sciences, Ås, Norway.

Email: paduran@nmbu.no

Abstract

In this study, we have proposed an automated classification approach to identify meaningful patterns in wind field data. Utilizing an extensive simulated wind database, we have demonstrated that the proposed approach can identify low-level jets, near-uniform profiles, and other patterns in a reliable manner. We have studied the dependence of these wind profile patterns on locations (eg, offshore vs onshore), seasons, and diurnal cycles. Furthermore, we have found that the probability distributions of some of the patterns depend on the underlying planetary boundary layer schemes in a significant way. The future potential of the proposed approach in wind resource assessment and, more generally, in mesoscale model parameterization improvement is touched upon in this paper.

KEYWORDS

low-level jets, mesoscale modeling, neural networks, planetary boundary layer, self-organizing maps, vertical wind profile

1 | INTRODUCTION

The state-of-the-art wind energy resource assessment and short-term wind forecasting primarily rely on computer-aided simulations of atmospheric flows.^{1,2} The so-called mesoscale meteorological models (MMMs) are typically utilized for such simulations.^{3,4} These models numerically solve the conservation equations for mass and momentum (known as the Navier-Stokes equations). They also solve the thermodynamic energy equation and the conservation equations for various phases of water (eg, water vapor and cloud water). Most of the relevant physical processes (eg, turbulence, radiation, microphysics, and land-atmosphere interactions) are parameterized in MMMs.⁵ Most of these parameterization schemes interact nonlinearly with one another. Depending on the applications, the MMMs make use of either global model-generated forecasts (eg, Global Forecast System) or reanalysis data (eg, ERA-5) as the initial and (time-dependent) boundary conditions.

From the time of the publication of Lorenz's seminal paper,⁶ it became known that all the numerical weather prediction (NWP) models, including MMMs, are intrinsically sensitive to the errors in the initial and boundary conditions⁷ in addition to the imperfections in the numerical schemes and parameterizations. All these errors impose stringent limits to the overall predictability.⁸ To account for such sensitivities, over the years, the NWP modeling community has developed different types of ensemble forecasting frameworks.^{9,10} By perturbing the initial/boundary conditions and/or by selecting different parameterization schemes, a suite of model forecasts (aka ensemble forecasts) are generated. Then, based on the (dis)agreements among various members of the ensemble, the uncertainty of the simulations or forecasts is quantified in a rigorous manner.

In the recent years, the wind energy community has become well aware of the MMM sensitivity issue, and a large number of papers have been published. From a wind modeling perspective, especially under calm synoptic conditions, the planetary boundary layer (PBL) parameterization is the most important factor. Thus, it is not surprising that most of the sensitivity studies in the wind energy literature focused on the PBL aspect.¹¹⁻¹⁵ In contrast, only a handful of studies focused on the sensitivities with respect to other physical parameterizations,¹⁶ initial/boundary conditions,¹⁷ horizontal resolution,¹⁸ vertical resolution,¹⁹ spin-up times,¹⁴ etc.

In wind energy literature, the MMM-based results are traditionally validated against observational data from a few isolated stations (eg, met-masts and lidars). Verification statistics like bias, root-mean-square error (RMSE), mean absolute error, correlation coefficient, and threat score^{20,21} are utilized. However, due to the aforementioned sensitivity issues, the MMM-simulated fields are always displaced in space and/or time from their observed counterparts, and the standard verification metrics can lead to wrong conclusions. A case in point is the recent study

by Lorenz and Barstad,²² who dynamically downscaled the ERA-interim dataset (grid-size of 79 km) by the Weather Research and Forecasting (WRF) model (grid-size of 3 km). They reported that, in terms of RMSE, the WRF-based simulated wind fields were significantly inferior to the corresponding ERA-interim fields. Below, we quote the authors as they have correctly identified the root of the problem:

"[...] the finer horizontal grid spacing will generally produce better defined mesoscale features of the atmospheric flow, while timing errors in the synchronization between the model and the actual flow are likely to be amplified and then heavily penalized in terms of RMSE."²²

Broadly speaking, there are two competing strategies to confront the challenging issue of forecast verification. In the first strategy, one makes use of advanced verification metrics that account for both magnitude and displacement errors.^{23,24} In this respect, the wind energy community can greatly benefit from the existing literature on quantitative precipitation forecast (QPF) verification (please refer to Gilleland et al²⁵ and the references therein). The second strategy would be to utilize certain statistics (eg, probability density function [pdf] and energy spectra), which are not modulated by the spatio-temporal displacement errors. For illustrative examples, please refer to Skamarock,²⁶ Skamarock et al,²⁷ and Borsche et al.²⁸

In this study, we also employ the second strategy. However, instead of spectra or pdf, we focus on the "patterns" or "shapes" of wind profiles in the lowest 1 km of our atmosphere. We propose a fully automated classification approach that can extract the dominant patterns from either an observed or a simulated wind database. In turn, this approach can identify if specific settings (eg, resolution and PBL parameterization) of an MMM have higher tendency to produce certain canonical patterns (eg, well-mixed profiles or low-level jets [LLJs]). Such findings are tremendously valuable for the model developers. In addition, the classified wind profile patterns can be readily utilized to quantify diversity in any multimodel or multiphysics ensemble framework.

The workhorse behind our proposed classification approach is the so-called self-organizing map (SOM) methodology. Even though SOMs have been extensively used in a wide range of disciplines like signal processing, operational research, artificial intelligence, data mining, automatic control, robotics, telecommunications, chemistry, and medicine,²⁹ their application in the wind energy literature is rather limited.³⁰⁻³⁴ Thence, we provide an in-depth technical background of SOMs in Section 2.

In order to avoid spatio-temporal data gaps and other quality-control issues, which are omnipresent in any observed database, we decided to make use of a simulated wind database in this proof-of-concept study. A popular MMM, the WRF model,³⁵ was utilized to generate this database with a focus on the North Sea and its surrounding regions. Our WRF modeling approach, as well as the proposed automated classification approach, is described in Section 3. The classified wind patterns are illustrated and described in Section 4; in this section, we have also elaborated on the dependence of these patterns on geographical locations, diurnal cycle, seasonality, and PBL parameterizations. In Section 5, we have reported a qualitative comparison between our model-based results and findings from an observational study. Lastly, concluding remarks and further applications of the proposed methodology are mentioned in Section 6.

2 | SELF-ORGANIZING MAPS

A SOM is a type of artificial neural network introduced by Kohonen,²⁹ used in data visualization, dimensionality reduction, and classification problems. Compared with alternative methods utilized for the same kind of problems, SOMs have shown superior capabilities. For example, it has been demonstrated that unlike principal component analysis (PCA),¹⁰ SOMs are able to identify nonlinear relationships in the data.³⁶⁻⁴⁰ Particularly, for classification problems, SOMs determine class membership more accurately than the well-known *k*-means clustering algorithm.⁴¹⁻⁴³

SOMs have been used in various meteorological applications since its introduction into the discipline by Hewitson and Crane.⁴⁴ Sheridan and Lee⁴⁵ and Liu and Weisberg⁴⁶ provide comprehensive reviews. Some of the papers by Cassano, Nigro, and their collaborators deserve special mention because they inspired our current study. These authors primarily focused on the near-surface layer (up to 30 m) over the Ross Ice Shelf in the Antarctic. Nigro et al⁴⁷ used SOM to characterize seasonal variability of near-surface wind speeds. Cassano et al⁴⁸ used a similar approach to extract patterns of near-surface temperature inversion and diagnosed their relationships with observed surface wind speeds and simulated sea-level pressure. In a follow-up work, Nigro et al⁴⁹ systematically utilized the SOM approach to validate the WRF model-based Antarctic Mesoscale Prediction System (AMPS) against the observational dataset. Further analysis using SOMs has been conducted by Katurji et al.⁵⁰ They analyzed the temporal evolution of remote sensing-based boundary layer (up to 500 m) wind speed and temperature profiles and quantified transitional probabilities among different atmospheric states.

The present study sets itself apart from the existing literature on several fronts. First of all, it focuses on the characterization of tall (approximately 1 km) wind profiles, which are of great interest to the wind energy community, including the emergent field of airborne wind energy. Second, we employed an ensemble modeling approach, which enabled us to investigate the dependencies of simulated wind patterns on the PBL schemes for the first time. Last, our proposed approach is much more automated (ie, less subjective) in comparison with most published SOM-based articles in meteorology.

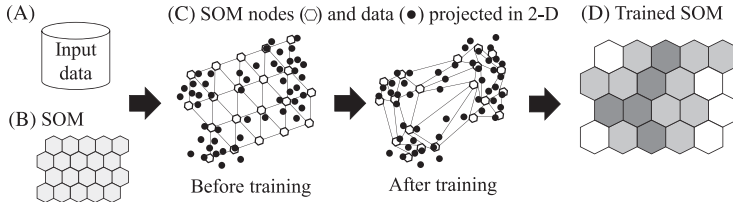


FIGURE 1 Example of the SOM training procedure with a dataset with 20 nodes and three clusters. Darker (lighter) shading in the SOM before (B) and after (D) training represents longer (shorter) distances between the node and its neighbors

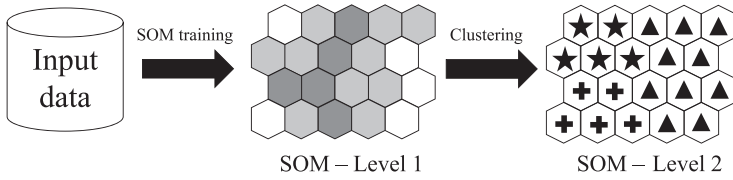


FIGURE 2 Graphical representation of the two-level SOM clustering (SOM2L) approach for the example with three clusters previously shown in Figure 1. Symbols in the SOM indicates cluster membership

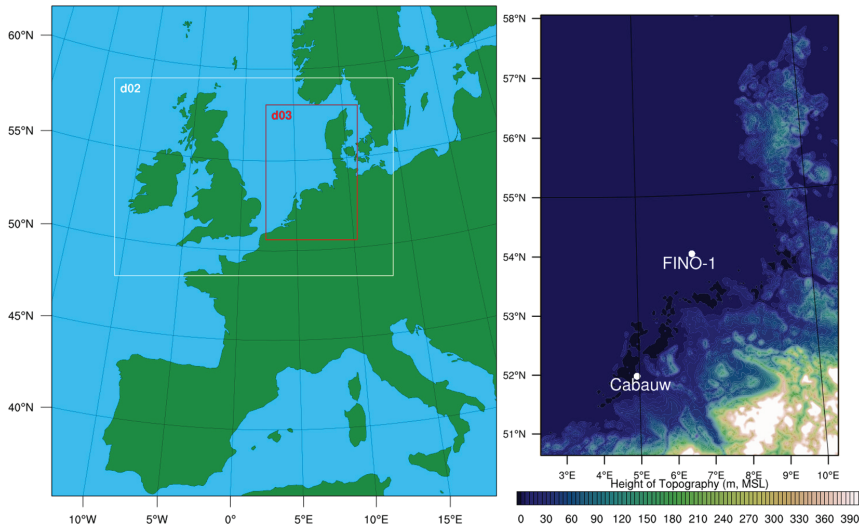


FIGURE 3 Left panel: the WRF computational domains. The outermost domain has a grid size of 27 km. The inner domains utilize grid sizes of 9 km (d02) and 3 km (d03), respectively. Right panel: the topographic map of domain d03. The locations of FINO-1 and Cabauw are marked with white circles

2.1 | SOM structure and learning algorithm

As mentioned earlier, we have created a WRF model-generated dataset consisting of large samples of wind speed profiles; we wish to classify these samples into few patterns that represent the diversity of the whole dataset. Let us assume that in this dataset, we have N samples of wind speed profiles, where the total number of vertical levels of each profile is M . For a given sample n , the wind speed value at a level m will be denoted as U_n^m , where $m \in [1, M]$ and $n \in [1, N]$. When we refer to a specific wind profile, we will simply drop the superscript and use the notation U_n . A map with K nodes (also referred as to neurons) is placed in the data-space. These nodes are connected in such a way that they form a grid (Figure 1B), which corresponds to the SOM. This grid could be composed of hexagons or squares. The position in the SOM of each node k is (x_k, y_k) , where $x_k \in [1, X]$ and $y_k \in [1, Y]$, giving a total number of SOM nodes $K = X \times Y$. The position of each node in the data-space is described by its weight w_k , with $k \in [1, K]$. The idea is that those weights are modified in such manner that nodes are transferred closer to where the data are located and further away from data-sparse areas. In other words, we desire to compress the map in presence of data and to stretch it at the areas where there are no data (Figure 1C). To achieve this, the weights of the neurons are iteratively calculated through an unsupervised training algorithm that periodically adjusts them. By plotting the distance among nodes, it is possible to visualize the clustering structures in the data (Figure 1D).

In a nutshell, this is how the SOM approach works. In the following paragraphs and subsections, we will elaborate on various technical details.

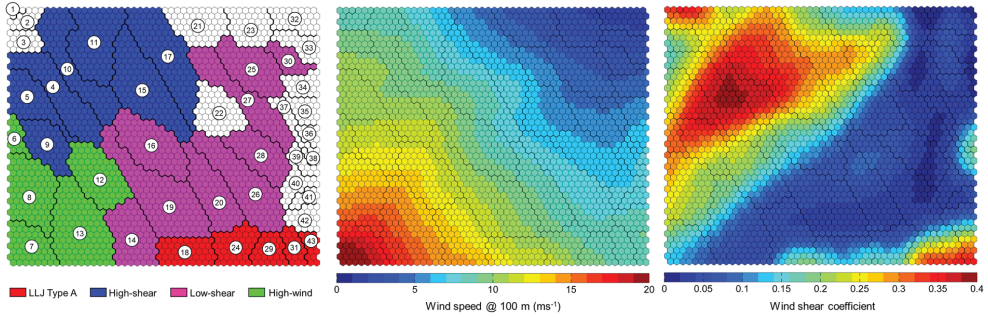


FIGURE 4 Left panel: converged solution of the trained SOM with a map dimension of 46×50 . The numbers in the white circles indicate the cluster membership of the nodes, and the bold lines indicate the boundaries of the clusters. Some clusters are colored according to the superclusters defined in Section 4. Middle and right panels: representative wind speed at 100 m and wind shear coefficient of the nodes of the SOM, respectively. The wind shear is calculated using the power-law between the heights of 70 m and 100 m above surface

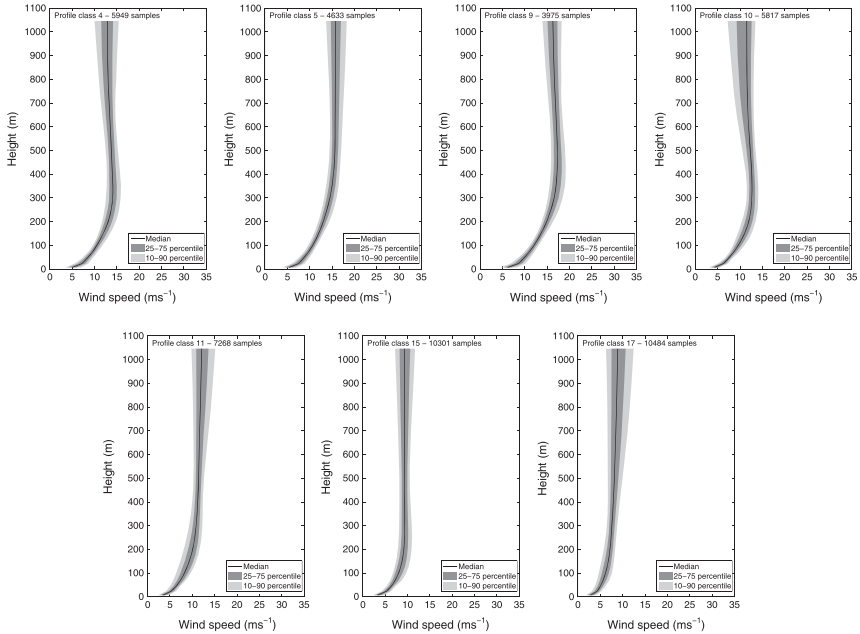


FIGURE 5 Members of the high-shear supercluster obtained by the SOM2L approach. The solid black lines, dark gray shaded areas, and the light gray areas correspond to the medians, 25th-75th percentile ranges, and 10th-90th percentile ranges of all the samples, respectively. The sample size is indicated at the top of each panel

2.1.1 | Initialization

Before the training procedure, the weights of the neurons are typically initialized using one of the following options: random samples or linear initialization.²⁹ When random samples are used, each component n of the initial weights is randomly chosen from a uniform distribution in the range $[\min(U_n^m), \max(U_n^m)]$. For the linear initialization, PCA⁵¹ is performed over the data. The weights are then located in the hyperplane formed by the two first principal components. Given its faster convergence and robustness, linear initialization is preferred⁵² and therefore is used in the present study.

2.1.2 | Learning algorithm

The SOM is trained using an unsupervised learning algorithm. There are two training algorithms commonly used in the literature: sequential training and batch training.²⁹ In this study, the batch approach is used since it is faster and more robust than the sequential one.⁵² At each iteration of the batch training (also called epoch), the data are partitioned into K Voronoi regions $V_k = \{U_n \mid \|U_n - w_k\| < \|U_n - w_j\|, \forall j \neq k\}$. Each

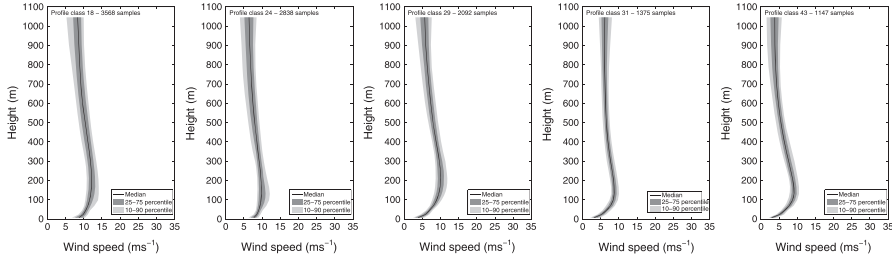


FIGURE 6 Members of the LLJ type A supercluster obtained by the SOM2L approach. The solid black lines, dark gray shaded areas, and the light gray areas correspond to the medians, 25th-75th percentile ranges, and 10th-90th percentile ranges of all the samples, respectively. The sample size is indicated at the top of each panel

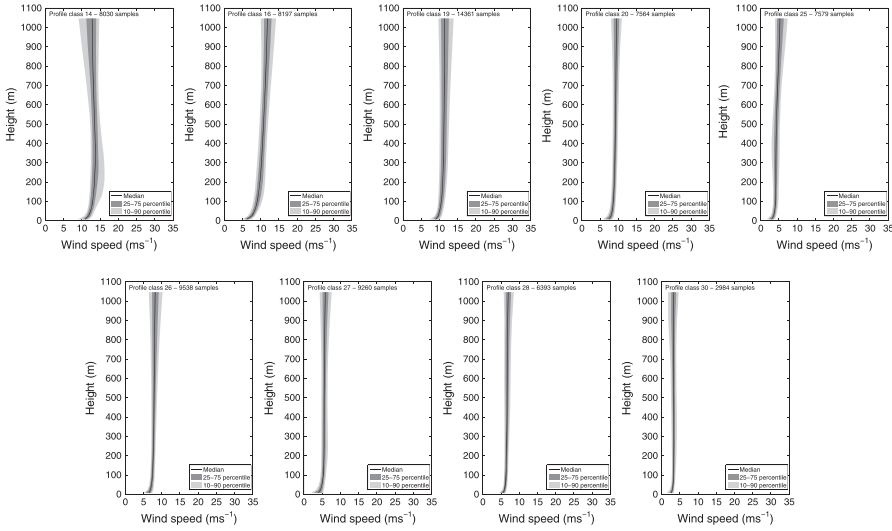


FIGURE 7 Members of the low-shear supercluster obtained by the SOM2L approach. The solid black lines, dark gray shaded areas, and the light gray areas correspond to the medians, 25th-75th percentile ranges, and 10th-90th percentile ranges of all the samples, respectively. The sample size is indicated at the top of each panel

Voronoi region can contain multiple samples of U_n . In a particular V_k , we have N_{V_k} samples of U_n . If N_{V_k} is nonzero, we compute the sum of samples in corresponding Voronoi region:

$$S_k = \sum_{n \in V_k} U_n. \tag{1}$$

A neighborhood function $H_{k,p}$ is calculated as

$$H_{k,p} = \exp\left(-\frac{|X_k - X_p|^2 + |Y_k - Y_p|^2}{2\sigma(i)^2}\right), \tag{2}$$

where $\sigma(i)$ is the effective radius of the neighborhood. Finally, the weight at node k is updated according to⁵³

$$w_k(i+1) = \frac{\sum_{p=1}^K H_{k,p}(i) S_p(i)}{\sum_{p=1}^K N_{V_p}(i) H_{k,p}(i)}, \forall k \in [1, K]. \tag{3}$$

After each iteration i , the Voronoi regions are updated. Thus, N_{V_p} , S_p , and $H_{k,p}$ are also recomputed, giving a new value of w_k .

2.1.3 | Effective neighborhood radius

Equation (3) indicates that the weight of node k is calculated depending on the data associated with its neighboring nodes. The magnitude of influence is calculated in Equation (2) depending on the distance to the neighbor and on the parameter $\sigma(i)$. Higher values of $\sigma(i)$ correspond to a

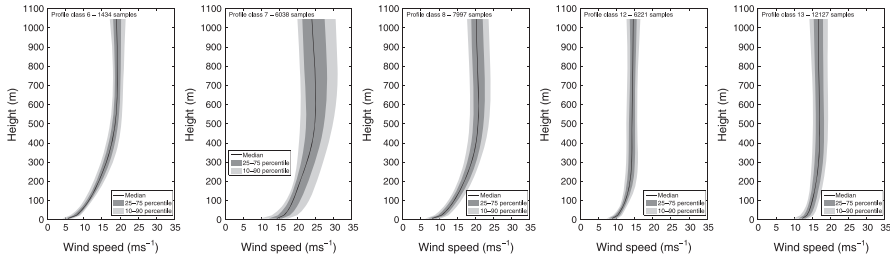


FIGURE 8 Members of the high-wind supercluster obtained by the SOM2L approach. The solid black lines, dark gray shaded areas, and the light gray areas correspond to the medians, 25th-75th percentile ranges, and 10th-90th percentile ranges of all the samples, respectively. The sample size is indicated at the top of each panel

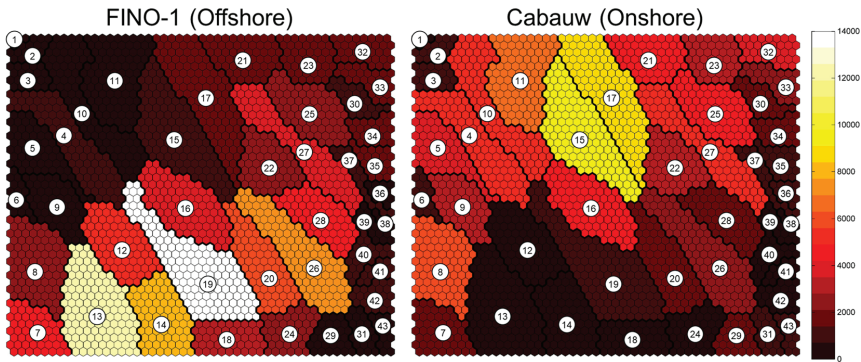


FIGURE 9 Frequency distributions of the profile clusters obtained by the SOM2L approach for FINO-1 (left panel) and Cabauw (right panel) locations. The coloring scale corresponds to the number of samples in each class. Please refer to Figure 4 for other technical and graphical details

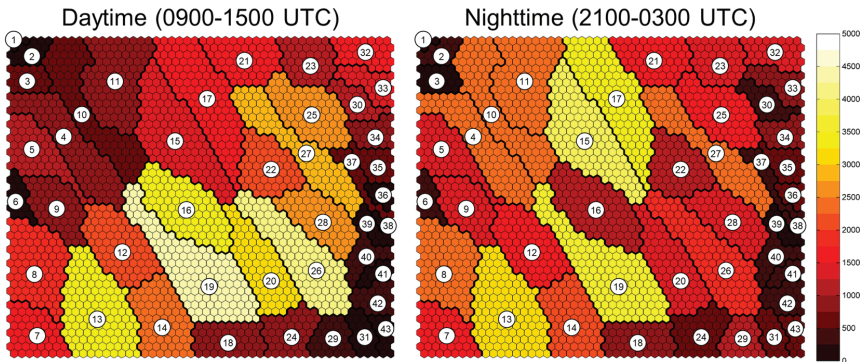


FIGURE 10 Frequency distributions of the profile clusters obtained by the SOM2L approach for daytime (left panel) and nighttime (right panel) periods. The coloring scale corresponds to the number of samples in each class. Please refer to Figure 4 for other technical and graphical details

stronger influence from its neighbors. Visually, this corresponds to bigger areas of the SOM being simultaneously moved towards the data after each iteration. For this reason, training stages in which big radii are used are referred to as rough training, whereas for small values, it is called fine training. It is a common practice in the literature to train a SOM with one rough and one fine phase. If linear initialization is utilized, the coarser training can be skipped.⁵³

2.1.4 | Structure of SOM

The selection of the proper number of nodes in the SOM is a common concern that is addressed by Kohonen.⁵² He emphasized that the purpose of SOMs is to visualize the underlying data and its clustering structures in a 2-D plane. Therefore, the capability of a SOM to distinguish among

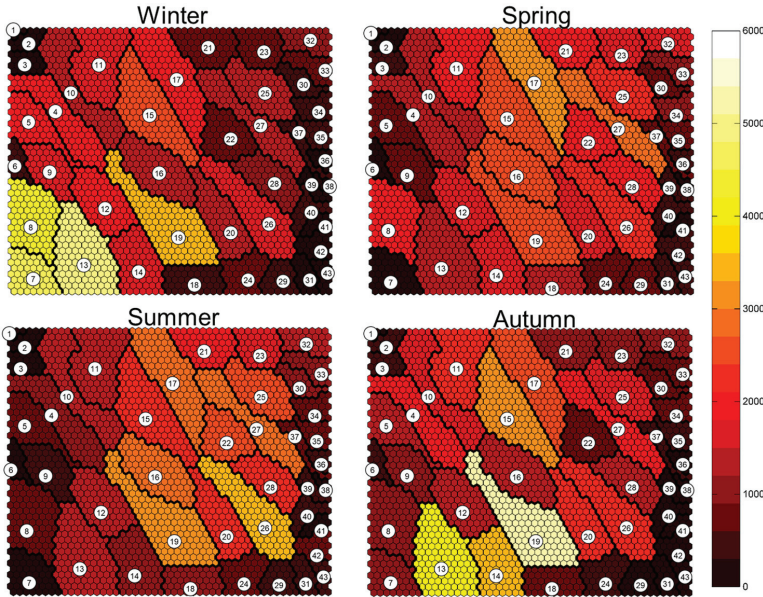


FIGURE 11 Frequency distributions of the profile clusters obtained by the SOM2L approach for winter (top-left panel), spring (top-right panel), summer (bottom-left panel) and autumn (bottom-right panel) seasons. The coloring scale corresponds to the number of samples in each class. Please refer to Figure 4 for other technical and graphical details

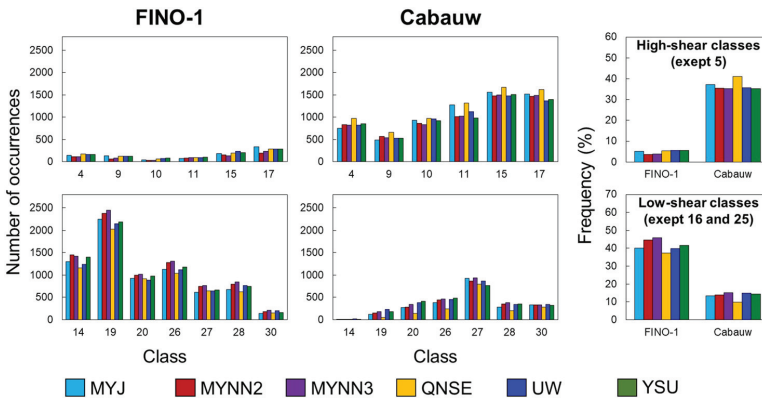


FIGURE 12 Frequency distribution of the members of the high-shear (except 5) and low-shear (except 16 and 25) superclusters at FINO-1 (left) and Cabauw (center). The frequency distribution of the each group is displayed in the right panels

different data clusters will be limited by the number of nodes in the map, which can be interpreted as the “resolution” of the map. The higher the number of expected clusters, the more nodes the grid should have. Then in principle, when the purpose is to cluster the data, one may use an array as large as feasible given the constraint of computational power. To avoid ad hoc prescription, a rule-of-thumb estimate was proposed by Vesanto and Alhoniemi⁵⁴: $K \approx 5\sqrt{N}$. Following the literature,^{55–57} we have also adopted this estimate in this study. As previously mentioned, a SOM can be arranged in hexagonal or square grids. In this study, we select a hexagonal grid shape since it produces a smoother distance map, which is advantageous for the application of the clustering methodology explained in the next subsection.

2.2 | Two-level SOM clustering

In the meteorology literature at large, the partition given by the Voronoi regions of the SOM nodes is directly used to cluster the data. Since the main purpose of SOMs is to visualize the clustering structures of the underlying data, such practice is inappropriate as alluded by Wu and Chow.⁵⁸ First of all, the properties of the neighboring nodes are quite similar (illustrative examples are provided later in Section 4); thus, they contain redundant information and the cluster size should be reduced in a systematic manner.⁵⁹ In addition, given the 2-D grid structure of a SOM, the total number of clusters are somewhat constrained as they have to be nonprime numbers. Thus, as a viable alternative, a two-level approach^{53,60} (henceforth SOM2L) is utilized in this study (see Figure 2). In SOM2L clustering, the nodes of the trained SOM are treated as “proto-clusters” and correspond to the first-level of the clustering process. These nodes are then in turn clustered using another cluster technique (eg, *k*-means and linkage). The cluster solution of this latter step is referred to as the second level. It has been shown⁵⁸ that SOM2L approaches performed

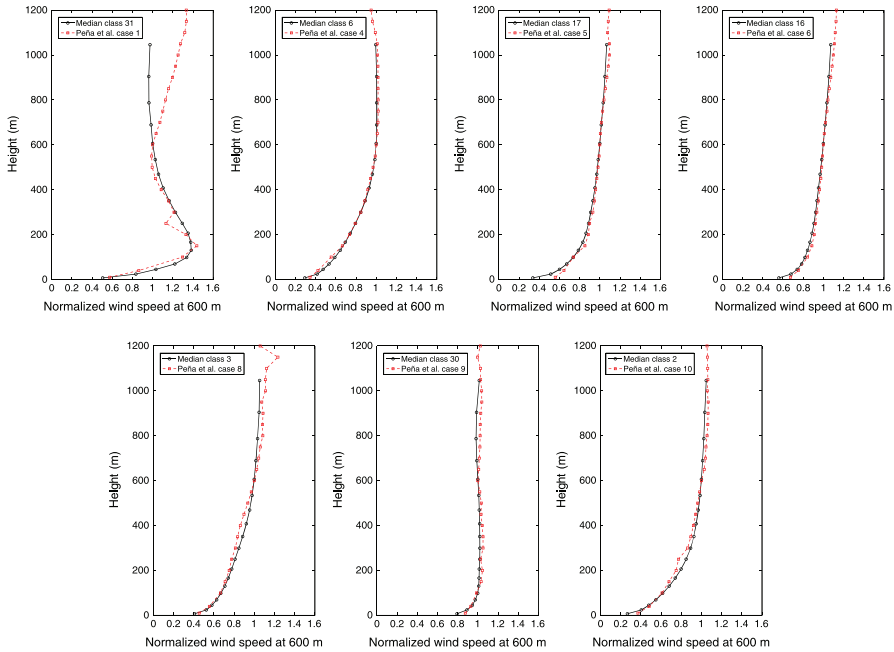


FIGURE 13 Comparison of a few wind speed vertical profiles reported by Peña et al.⁸³ against the SOM2L-based results. The profile class and the observed case are indicated in the upper-left corner of each panel. All the profiles are normalized by the wind speed at 600 m

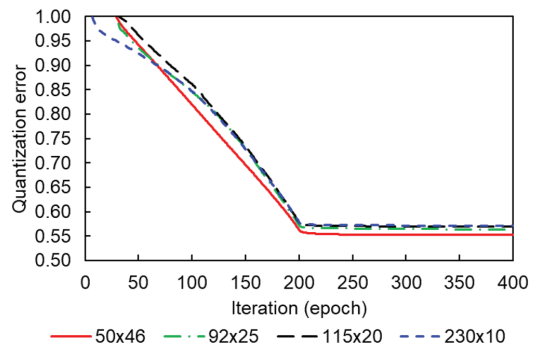


FIGURE 14 Quantization error of different SOM grids with a total of 2300 nodes

much better than the sole application of the clustering method used in the second level (ie, without the initial SOM step). Despite this stellar performance, we are aware of only two publications in meteorology,^{61,62} which leveraged on the SOM2L approach.

In this study, the trained SOM is clustered using the distances between its nodes. The number of clusters (K^*) is defined by the number of local minima of the distances between the K nodes.⁵⁹ The nodes corresponding to the local minima are used as the initial clusters. Then, unassigned nodes in the surroundings of the local minima are aggregated to the initial clusters following Ward's criterion.⁶³ Some of the local minima might occur simply due to the random variations in the data and not due to any specific cluster structure.⁵⁹ It is expected that this problem is reduced when using hexagonal grid tiles, since each local minimum is then surrounded by six nodes instead of four nodes (as in square grids). Nodes that do not have data associated are referred to as "interpolating map units."⁵³ These nodes represent the border between the clusters in the data, and therefore, they are not assigned to a cluster.

The local minima-based procedure assures a relative independence between the number of nodes in a SOM and the final number of clusters in SOM2L as long as there are enough nodes.⁵⁴ Furthermore, the total number of final clusters (could be primes or nonprimes) are determined in a completely automated manner; no ad hoc prescription is needed. This automation makes the proposed methodology more advantageous compared with the previous application of SOMs to identify patterns in near-surface or boundary layer wind data.⁴⁷⁻⁵⁰

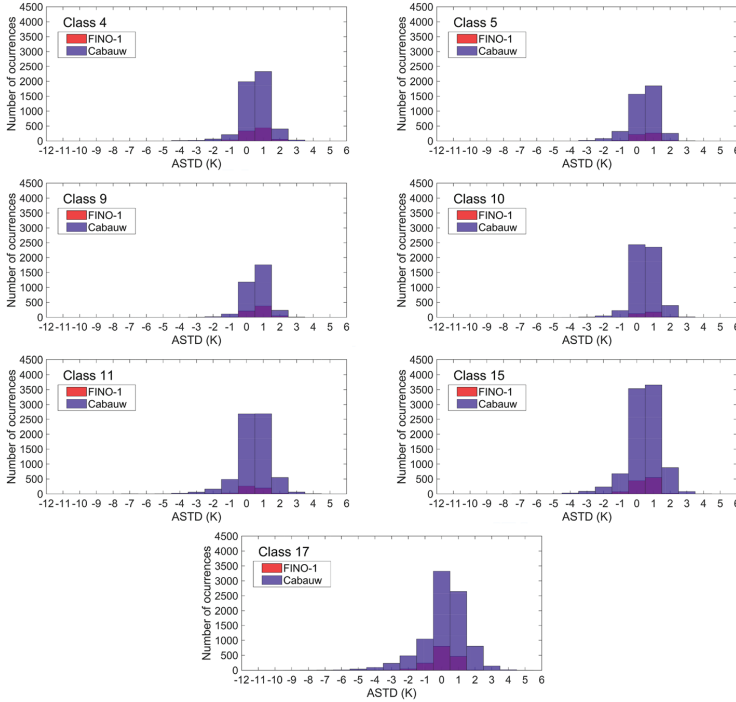


FIGURE 15 Frequency distribution of ASTD for the members of the high-shear supercluster

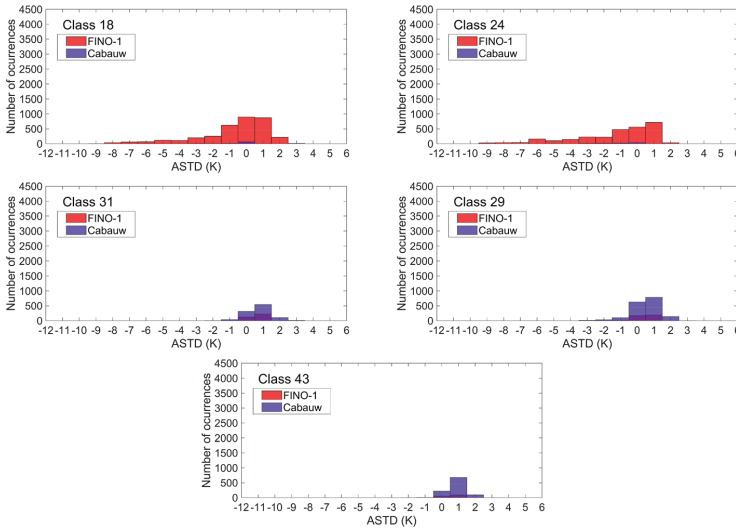


FIGURE 16 Frequency distribution of ASTD for the members of the LLJ type A supercluster

3 | METHODOLOGY

In this section, we first describe our WRF modeling approach. Then, we discuss the application of the SOM2L approach for the WRF model-generated wind profiles.

3.1 | WRF modeling

In the present study, version 3.6.1 of the WRF model is employed to generate the wind profile database. Three nested domains with one-way coupling are used in the simulation. The outer domain (d01) employs a horizontal grid size of 27 km × 27 km, the middle domain (d02) uses a grid

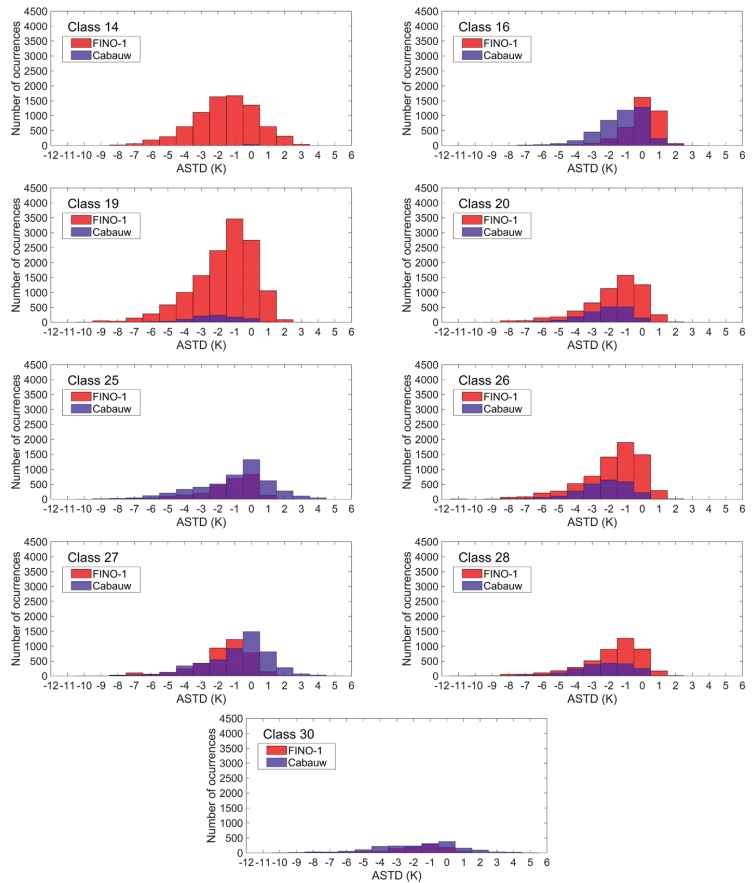


FIGURE 17 Frequency distribution of ASTD for the members of the low-shear supercluster

size of $9 \text{ km} \times 9 \text{ km}$, whereas the innermost domain (d03) uses a grid size of $3 \text{ km} \times 3 \text{ km}$ (refer to Figure 3). In all the domains, 51 nonuniformly stretched vertical levels are used. The lowest model level is at approximately 8 m above ground level (AGL); the top of the domain is close to 16 000 m AGL. Approximately 18 vertical levels are below 1 km AGL.

The total simulation period was the year of 2012. We performed several continuous month-long WRF simulations forced by the ERA-Interim reanalysis dataset.⁶⁴ In order to keep the large-scale flows in sync with the high-resolution WRF simulations, grid nudging is activated for model levels above approximately 2 km (specifically, at vertical grid level of 23). The integration time steps are 90, 45, and 15 seconds for the d01, d02, and d03 domains, respectively.

The following physics parameterizations are utilized in all the simulations: (a) land surface: Noah scheme⁶⁵; (b) shortwave and longwave radiation: Rapid Radiative Transfer Model for Global Climate Models (RRTMG) scheme^{66,67}; (c) microphysics: WRF Single-Moment 5-class scheme⁶⁸; and (d) cumulus: modified Kain-Fritsch scheme⁶⁹ (only for d01 and d02 domains). Most of these parameterization schemes are discussed in great detail by Stensrud.⁵ In order to create a multiphysics ensemble dataset, a different PBL parameterization (and corresponding surface layer parameterization) is invoked for each model run. All in all, the following PBL schemes are utilized: Mellor-Yamada-Janjić⁷⁰ (MYJ), Mellor-Yamada-Nakanishi-Niino^{71,72} level 2.5 (MYNN2) and level 3 (MYNN3), Quasi-Normal Scale Elimination⁷³ (QNSE), University of Washington⁷⁴ (UW), and Yonsei University scheme^{75,76} (YSU).

From all the model runs, wind data are extracted from two locations: the grid points closest to the FINO-1 offshore platform over the North Sea (54.01N, 6.59E) and the Cabauw tower in the Netherlands (51.97N, 4.93E). The so-called tlist option is used in the WRF model to extract “virtual tower” data with a high sampling rate of 15 seconds. These data are averaged over 30 minutes to avoid random fluctuations. The total number of samples in our simulated database is $N = 210816 (= 2 \times 8784 \text{ hours} \times 2 \text{ locations} \times 6 \text{ PBL schemes})$.

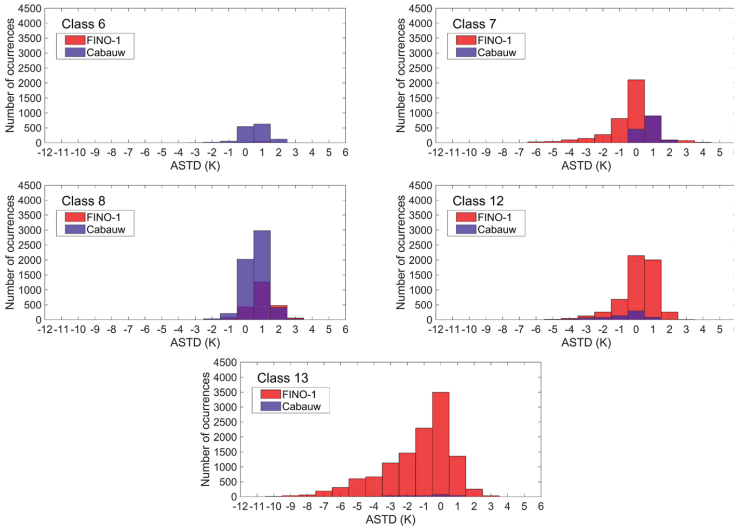


FIGURE 18 Frequency distribution of ASTD for the members of the high-wind supercluster

3.2 | SOM2L-based wind profile classification

Each simulated wind profile (U_n) has a total of $M = 19$ vertical levels, spanning up to ≈ 1050 m above the land/sea surface. For the SOM training procedure, the normalized profiles U'_n are used instead of U_n (see Equation 5). Such normalization prevents higher values, like wind speeds at higher heights, to unduly dominate the SOM learning process.

$$\bar{U} = \frac{\sum_{n=1}^N U_n}{N}, \quad (4)$$

$$U'_n = \frac{U_n - \bar{U}}{\sqrt{\frac{\sum_{n=1}^N (U_n - \bar{U})^2}{N-1}}}. \quad (5)$$

According to the rule-of-thumb estimate mentioned in Section 2.1, a SOM of approximately $K = 5\sqrt{210816} \approx 2295$ nodes should be used for a sample size of 210816; so, we selected 2300 nodes in this study. The dimensions of the SOM grid are selected as $X = 46$ and $Y = 50$ following a sensitivity analysis performed in Appendix A. The map weights w_k are prescribed using linear initialization and trained using the batch algorithm in two phases (see Section 2.1). In the first phase, σ is linearly decreased from 10 to 2 in 200 iterations. In the second phase, σ is kept equal to 2 for 200 iterations. This procedure is in line with the recommendations of Vesanto.^{53,54} The SOM training was conducted using the public-domain MATLAB SOM toolbox.⁵³ After training, the SOM is clustered using the local minima of the distance among nodes and the Ward's criteria noted in Section 2.2. The final cluster solution has a total of $K^* = 43$ classes. Please note that in the rest of the paper, we will use the words “class” and “cluster” interchangeably.

4 | RESULTS

The profile classes obtained from the application of the SOM2L approach, presented in Section 3.2, exhibit a variety of patterns and wind speed magnitudes. Some of them correspond to the well-studied patterns like the LLJ, power-law, or near-uniform (mixed layer) profiles, while other profiles classes do not have any well-known shape. In Figure 4, the cluster solution of the SOM is shown. Each of these clusters correspond to a particular profile shape. Given the spatial properties of SOMs, we know that the classes that are adjacent to one another in the map share certain characteristics (in this case, wind speed, wind shear, or shape). Furthermore, certain characteristics of the wind profile classes change with respect to a direction in the map. For example, the wind speeds of the classes increase towards the bottom-right portion of the SOM, whereas the classes with the lowest wind speeds are located at the upper-left portion of the map (see middle panel of Figure 4). Another example is shown in the right panel of Figure 4, which portrays a coherent spatial distribution of wind shear coefficient within the SOM.

The spatial ordering feature of a SOM allows one to combine similar (ie, neighboring) classes into a handful of superclusters. Such mergers do facilitate generalization of the wealth of results generated by a SOM2L approach. In this study, selected classes were merged into four broad

superclusters (see Figure 4) as follows: (a) LLJ type A (classes 18, 24, 29, 31, and 43), (b) high-shear (classes 4, 5, 9, 10, 11, 15, and 17), (c) low-shear (classes 14, 16, 19, 20, 25, 26, 27, 28, and 30), and (d) high-wind (classes 6, 7, 8, 12, and 13). The range of the wind speeds and wind shear for each of the superclusters are shown in Table 1. These superclusters were defined given their importance in the wind energy literature and their relevance for the analysis carried out in the following subsections. It was not possible to group the other classes in a meaningful way.

The high-shear supercluster consists of profiles that present a relatively high increase of the wind speed with height (close to a linear relation) up to 250 m (Figure 5). Classes 4, 9, and 10 present a clear LLJ signature, and therefore, this subset of the high-shear supercluster is hereafter referred to as LLJ type B. This name is used to differentiate them from the LLB type A supercluster classes discussed in the next paragraph. As expected, high-shear profiles mostly occur when the air-surface temperature differences (ASTD) are positive—ie, near-neutral to strongly stratified conditions (see Figure 14).

LLJ type A and type B (henceforth LLJ A and LLJ B) classes include profiles with wind speed maxima below 1000 m (Figures 6 and 5, respectively). All these LLJ profiles have distinctly different jet heights, peak wind speed, and wind shear above the jet—also called falloff⁷⁷ (see Table 2). The main difference between the LLJ A and LLJ B classes is that the first have a relatively small sample size, but they have a well-defined LLJ shape. The opposite is true for the LLJ B. As it is expected for LLJs, these classes mostly occur in stably stratified conditions (see Table 2 and Figures 15 and 16).

The low-shear supercluster consists of classes that present a near-uniform wind speeds above 100 m (Figure 7). The main difference among these classes is the magnitude of wind speeds (Table 3). From the corresponding ASTD distributions (Table 3 and Figure 17), it can be inferred that the near-uniform profiles are primarily present during unstable (convective) conditions.

The last group defined is the high-wind supercluster and corresponds to profiles with winds type 7 (ie, 13.9–17.1 m s⁻¹; near gale) or higher in the Beaufort scale at 100 m (Figure 8). The Beaufort scale is defined for heights z_{scale} between 10 and 20 m.⁷⁸ To compare the wind speeds at 100 m, we scaled them by a factor equals to $(100/z_{scale})^{1/7}$, following the 1/7th power law. The ASTD distributions for this supercluster are shown in Figure 18. In the literature, it is generally assumed that for high-wind conditions, one can neglect the buoyancy effects. At Cabauw, we do see that the magnitudes of the ASTD values are not far from zero. Interestingly, at FINO-1, one finds a wide range of ASTD values associated with high-wind conditions. In other words, one cannot neglect the buoyancy effects for strong offshore wind conditions. Our results are in complete agreement with a recent study by Baas et al.⁷⁹

In the following subsections, we document how the frequency distribution of some of the classes discussed in this section depend on location, diurnal cycle, seasonality, and PBL scheme.

4.1 | Dependence on locations

The frequency distributions of the profile classes are very different for FINO-1 and Cabauw (Figure 9). The clusters in the lower-center and lower-left of the SOM grid have a higher predominance for FINO-1, which mostly correspond to low-shear and high-wind speed superclusters. On the other hand, clusters at the upper part of the SOM are more frequent in Cabauw, which correspond to high-shear profiles with moderate wind speed, including LLJs. Most clusters at the right of the map appear to be more evenly distributed among the two locations, which correspond to profiles with low wind speed and/or low overall frequency. The left part of the LLJ A supercluster (classes 18 and 24) is prevalent in FINO-1 while the right part (classes 29, 31, and 43) is more common at Cabauw. In contrast, the entire LLJ B supercluster is frequently observed only at Cabauw.

Classes 13 (high-wind), 14 (low-shear), and 19 (low-shear) mostly occur at FINO-1 location. All these classes are located nearby on the SOM (see Figure 9). We would like to note that class 32 shares the traits of both high-wind (see Figure 8) and low-shear (see Figure 7) profiles. From their shape and simulated ASTD, it appears that these types of profile occur in unstable as well as near-neutral conditions (see Figures 17 and 18).

At Cabauw, classes 15 and 17 are the most dominant ones. These classes correspond to the high-shear supercluster (Figure 5). They are also located adjacent to one another on the SOM (see Figure 4).

4.2 | Dependence on diurnal cycles

Some profile classes are more predominant at certain times of the day (Figure 10). Most of the variability is found between the daytime and the nighttime periods. Morning and evening transitional periods did not portray any discriminatory patterns; therefore, they are not discussed. Interestingly, the lower-left and the upper-right parts of the SOM do not differ much between the daytime and nighttime periods; in other words, very low or high-wind speeds do not follow any diurnal cycles. They are likely modulated by the synoptic and/or mesoscale motions.

Significant differences between the daytime and nighttime periods are found in most classes of the high-shear supercluster (specifically, classes 4, 10, 11, 15, and 17) located in the upper-center portion of the SOM. These classes mostly occur at Cabauw during nighttime. Classes 4 and 10 (LLJ B group) correspond to nocturnal LLJs, which have been widely reported in the boundary-layer meteorology literature and have been well studied at Cabauw based on observational data.⁸⁰

Classes 16, 20, and 26 (Figure 7) are considerably more frequent during daytime compared with other periods of the day. Both classes belong to the low-shear supercluster. Such well-mixed conditions are quite common over land during unstable (convective) conditions as supported by Figure 17.

Supercluster	Sample Size	Wind Speed at 100 m (ms^{-1})			Wind Shear Coefficient			Frequency (%)	
		P10	P50	P90	P10	P50	P90	FINO1	Cabauw
LLJ type A	11020 (5.2%)	8.0	9.8	12.4	0.018	0.160	0.431	65	35
High-shear	48427 (23.0%)	5.9	8.8	11.4	0.113	0.279	0.471	12	88
Low-shear	73906 (35.1%)	4.1	8.1	12.0	0.011	0.044	0.185	68	32
High-wind	33817 (16.0%)	11.9	14.6	18.4	0.044	0.133	0.287	72	28

TABLE 1 Characteristics of the superclusters obtained by the SOM2L approach

Note. PXX stands for XX percentile. The wind shear is calculated using the power-law between the heights of 70 and 100 m above surface.

4.3 | Dependence on seasons

The frequency distribution of some classes depend very much on the seasons (Figure 11). In general terms, classes 29 to 43 (the right part of the SOM) are slightly more (less) frequent during warm (cold) seasons. In winter, classes 7 and 8 are very common. These classes are part of the high-wind supercluster; wind speeds above 500 m range 20 to 30 m s^{-1} and 18 to 24 m s^{-1} , respectively. By analyzing observational data from the Ijmuiden tower over the North Sea (85 km from the Dutch coastline), Kalverla et al^{B1} reported that the wintertime wind speeds are stronger than the summertime by approximately 5 m s^{-1} ; qualitatively, our results are consistent with their findings.

Classes 25, 26, 27, and 28 are more (less) frequent in warm (cold) seasons. This effect is more noticeable in winter or summer rather than spring or autumn. These four classes belong to the low-shear supercluster, which is partly correlated with unstable conditions (Figure 17). Therefore, their higher presence in warmer seasons are physically expected due to strong insolation. Sathe et al^{B2} analyzed observation data from (a) a 116-m-tall meteorological mast near the Egmond aan Zee offshore wind farm (OWEZ), the Netherlands, and (b) a 62-m-tall tower near Horns Rev wind farm, Denmark. Even though their analysis was limited to a directional sector (225–315), Sathe et al also noticed marked increase of unstable conditions during the summer months.

4.4 | Dependence on PBL schemes

The frequency distribution of individual classes is less dependent on the PBL schemes than locations or seasons. Despite these low variations, they are quite similar for some groups that share certain profile characteristics. These groups correspond to most members of the previously defined high-shear supercluster (classes 4, 9, 10, 11, 15, and 17) and low-shear supercluster (classes 14, 19, 20, 26, 27, 28, and 30). In Figure 12, the frequency distribution of these classes are displayed for six WRF simulations using different PBL schemes.

The occurrence of classes of the high-shear supercluster do not have important differences among PBL schemes at FINO-1, whereas at Cabauw, they are high. At this site, simulations using the QNSE scheme generated a total amount of LLJ B profiles that is 5.29% (464 hours) more than the amount reproduced on average by the other PBL schemes. The PBL schemes that produced the least LLJ profiles are MYNN3 and YSU, with a value of 1.64% (144 hours) and 1.69% (148 hours) less than the other PBL schemes, respectively.

In the case of the classes from the low-shear supercluster, the QNSE, MYNN2, and MYNN3 schemes are the ones with the highest differences. At FINO-1, the number of such profiles generated by the QNSE scheme is 5.04% (442 hours) less compared with the overall average by the other PBL schemes. At Cabauw, this difference is 4.53% (398 hours). In contrast to QNSE, the simulations using the MYNN2 and MYNN3 schemes generated more profiles belonging to the low-shear supercluster. Simulated profiles at FINO-1 using these schemes are, respectively, 3.67% (322 hours) and 5.07% (446 hours) more than the average of the other PBL schemes. At Cabauw, there are no significant differences among the PBL schemes.

5 | COMPARISON AGAINST AN OBSERVATIONAL STUDY

In the previous section, we have demonstrated that the proposed SOM2L approach allows one to identify and classify different profile shapes (eg, LLJs and low-shear) from a wind database. A few years ago, Peña et al^{B3} also tried to identify canonical tall-wind profiles measured at a coastal onshore location in Denmark (Høvsøre), about 300 and 540 km from FINO-1 and Cabauw, respectively. Based on visual inspection, they identified ten cases from an extensive observational database composed of sonic anemometers and lidar measurements. Some of these cases are shown in Figure 13. On these plots, we have overlaid qualitatively “similar” classes from the SOM2L-based results. To enable direct comparison, we have normalized all the profiles by the corresponding wind speeds at the height of 600 m. It is quite clear that the SOM2L approach, an automated (completely unsupervised) technique, can pose a serious competition to a more arduous manual approach. Thus, we believe that our SOM2L approach can be easily extended to other geographical and climatological conditions to characterize unknown wind patterns in a relatively efficient and cost-effective manner.

TABLE 2 Characteristics of the members of both LLJ superclusters obtained by the SOM2L approach

Class	Sample Size	Jet height (m)	Falloff ^a (ms ⁻¹)	Wind Speed at LLJ Peak (ms ⁻¹)			ASTD (K)			Frequency (%)	
				P10	P50	P90	P10	P50	P90	FINO-1	Cabauw
4	5949 (2.8%)	350	1.2	12.7	14.1	15.9	-0.21	0.57	1.38	15	85
9	3975 (1.9%)	470	1	15.9	17.3	19.1	-0.02	0.63	1.34	17	83
10	5817 (2.8%)	350	1.2	11.5	12.7	14.1	-0.18	0.52	1.34	6	94
18	3568 (1.7%)	200	3.9	10.8	12.2	14.1	-3.90	-0.10	1.27	97	3
24	2838 (1.4%)	170	3.4	8.7	9.8	11.9	-5.27	-0.61	0.99	97	3
29	2092 (1.0%)	200	4.4	8.7	10.1	11.9	-0.33	0.59	1.04	19	81
31	1375 (0.7%)	130	2.6	7.9	8.7	10.0	-0.09	0.70	1.41	27	73
43	1147 (0.5%)	130	5.3	7.9	9.1	10.5	0.12	0.83	1.44	13	87

Note. PXX stands for XX percentile. Falloff corresponds to the difference between the P50 wind speeds at the LLJ-peak and and the highest vertical level (approximately 1050 m).

TABLE 3 Characteristics of the members of the low-shear supercluster obtained by the SOM2L approach

Class	Sample Size	Wind Speed at 200 m (ms ⁻¹)			ASTD (K)			Frequency (%)	
		P10	P50	P90	P10	P50	P90	FINO1	Cabauw
14	8030 (3.8%)	12.3	13.5	16.2	-4.06	-1.47	0.82	99	1
16	8197 (3.9%)	8.6	9.8	11.2	-2.59	-0.37	0.77	47	53
19	14361 (6.8%)	9.9	10.9	12.0	-4.16	-1.34	0.36	94	6
20	7564 (3.6%)	8.3	8.9	9.6	-4.03	-1.50	0.02	76	24
25	7579 (3.6%)	3.4	4.2	5.0	-4.10	-0.73	1.04	35	65
26	9538 (4.5%)	7.1	7.7	8.3	-4.35	-1.62	-0.06	74	26
27	9260 (4.4%)	4.7	5.5	6.5	-3.82	-0.96	0.87	44	56
28	6393 (3.0%)	5.9	6.5	7.1	-4.42	-1.62	-0.02	70	30
30	2984 (1.4%)	2.8	3.4	4.1	-4.83	-1.42	0.72	35	65

Note. PXX stands for XX percentile.

6 | CONCLUDING REMARKS

In this study, we have proposed a two-level SOM clustering approach, named SOM2L, for the characterization of wind profiles from observed or simulated databases. This approach does not require any a priori prescription of cluster size; it also precludes generation of exceedingly large number of clusters and, in turn, reduces any redundancy in information. In an objective manner, SOM2L extracts the dominant profile patterns with characteristic shapes and magnitudes. By analyzing how these patterns evolve with respect to time and space, it is possible to associate them with underlying atmospheric phenomena or processes. For example, we demonstrated that the SOM2L approach was able to correlate the near-uniform profiles (prevalent in unstable conditions) and low-level jets (frequently occurs under stably stratified conditions) to the circadian cycle. Furthermore, it detected that the high-winds (gales or stronger) were more frequent in winter months than the summer months. Several other nontrivial cases were discussed earlier and will not be repeated here for brevity.

The SOM2L approach has demonstrated its potential to discriminate among various PBL schemes. Simulations utilizing the QNSE, MYNN2, and MYNN3 schemes showed statistically significant differences in generating some of the canonical wind profiles. The QNSE scheme produced lesser number of low-shear profiles and more low-level jets, whereas the opposite is true for the MYNN2 and MYNN3 schemes. This type of information, in contrast to the commonly used metrics (eg, RMSE), is valuable for model developers; we sincerely hope that the SOM2L approach will play an important role in the further development and rigorous assessment of the next-generation PBL schemes (eg, the gray-zone parameterizations).

The SOM2L approach (and its potential variants) can be used in many other arenas of wind power meteorology. Quantifying the diversity of wind fields generated via an ensemble framework being one of them. One could also borrow some ideas from the field of symbolic dynamics and probe the evolution of certain wind patterns. Yet another application arena of SOM2L is in the coupling of a mesoscale model (eg, WRF) with a microscale model (eg, WindSim); we are currently working in this arena. We are expanding our newly proposed wind profile (1-D) classification approach to wind fields (3-D) and exploring its usage for wind resource assessment and micrositing.

ACKNOWLEDGEMENT

This research was supported by a grant from The Norwegian Research Council, project number 271080.

ORCID

Pablo Durán  <https://orcid.org/0000-0001-7354-6897>

Sukanta Basu  <https://orcid.org/0000-0002-0507-5349>

Muyiwa S. Adaramola  <https://orcid.org/0000-0003-1998-687X>

REFERENCES

1. Brower MC. *Wind Resource Assessment: a Practical Guide to Developing a Wind Project*. Hoboken: John Wiley & Sons; 2012:296.
2. Lange M, Focken U. *Physical Approach to Short-term Wind Power Prediction*. Springer; 2006. 208.
3. Pielke Sr. R. A. *Mesoscale Meteorological Modeling*. Academic press; 2 ed.2002. 676 pp.
4. Warner TT. *Numerical Weather and Climate Prediction*. Cambridge: Cambridge University Press. 2010;526.
5. Stensrud DJ. *Parameterization Schemes: Keys to Understanding Numerical Weather Prediction Models*. Cambridge: Cambridge University Press. 2007;459.
6. Lorenz EN. Deterministic nonperiodic flow. *Journal of the Atmospheric Sciences*. 1963;20:130-141.
7. Chu PC. Two kinds of predictability in the Lorenz system. *Journal of the Atmospheric Sciences*. 1999;56:1427-1432.
8. Palmer T. *Hagedorn R, eds. Predictability of Weather and Climate*: Cambridge University Press; 2006:702.
9. Sivillo JK, Ahlquist JE, Toth Z. An ensemble forecasting primer. *Weather and Forecasting*. 1997;12:809-818.
10. Kalnay E. *Atmospheric Modeling. Data Assimilation and Predictability*: Cambridge University Press; 2003:341.
11. Draxl C, Hahmann AN, Peña A, Giebel G. Evaluating winds and vertical wind shear from Weather Research and Forecasting model forecasts using seven planetary boundary layer schemes. *Wind Energy*. 2014;17:39-55.
12. Nunalee CG, Basu S. Mesoscale modeling of coastal low-level jets: implications for offshore wind resource estimation. *Wind Energy*. 2014;17:1199-1216.
13. Carvalho D, Rocha A, Gómez-Gesteira M, Silva SC. Offshore wind energy resource simulation forced by different reanalyses: comparison with observed data in the Iberian Peninsula. *Applied Energy*. 2014;134:57-64.
14. Hahmann AN, Vincent CL, Peña A, Lange J, Hasager CB. Wind climate estimation using WRF model output: method and model sensitivities over the sea. *International Journal of Climatology*. 2015;35:3422-3439.
15. Krogseter O, Reuder J. Validation of boundary layer parameterization schemes in the Weather Research and Forecasting model under the aspect of offshore wind energy applications – Part I: Average wind speed and wind shear. *Wind Energy*. 2015;18:769-782.
16. Hawbecker P, Basu S, Manuel L. Realistic simulations of the July 1, 2011 severe wind event over the Buffalo Ridge Wind Farm. *Wind Energy*. 2017;20:1803-1822.
17. Carvalho D, Rocha A, Gómez-Gesteira M, Silva SC. Sensitivity of the WRF model wind simulation and wind energy production estimates to planetary boundary layer parameterizations for onshore and offshore areas in the Iberian Peninsula. *Applied Energy*. 2014;135:234-246.
18. Liu Y, Warner T, Liu Y, et al. Simultaneous nested modeling from the synoptic scale to the LES scale for wind energy applications. 2011;99:308-319.
19. Bernier NB, Bélair S. High horizontal and vertical resolution limited-area model: Near-surface and wind energy forecast applications. 2012;51:1061-1078.
20. Jolliffe IT, Stephenson DB. *Forecast Verification: a Practitioner's Guide in Atmospheric Science*. Hoboken: John Wiley & Sons; 2012 274 pp.
21. Koh TY, Wang S, Bhatt BC. A diagnostic suite to assess NWP performance. *Journal of Geophysical Research, [Atmospheres]*. 2012;117:1-20.
22. Lorenz T, Barstad I. A dynamical downscaling of ERA-Interim in the North Sea using WRF with a 3 km grid—for wind resource applications. *Wind Energy*. 2016;19:1945-1959.
23. Venugopal V, Basu S, Foufoula-Georgiou E. A new metric for comparing precipitation patterns with an application to ensemble forecasts. 2005;110:D08111.
24. Wang Y, Basu S. Utilizing the Kantorovich metric for the validation of optical turbulence predictions. 2016;41:4008-4011.
25. Gilleland E, Ahijevych D, Brown BG, Casati B, Ebert EE. Intercomparison of spatial forecast verification methods. *Weather and Forecasting*. 2009;24:1416-1430.
26. Skamarock WC. Evaluating mesoscale NWP models using kinetic energy spectra. 2004;132:3019-3032.
27. Skamarock WC, Park SH, Klemp JB, Snyder C. Atmospheric kinetic energy spectra from global high-resolution nonhydrostatic simulations. 2014;71:4369-4381.
28. Borsche M, Kaiser-Weiss AK, Kaspar F. Wind speed variability between 10 and 116 m height from the regional reanalysis COSMO-REA6 compared to wind mast measurements over Northern Germany and the Netherlands. *Advances in Science and Research*. 2016;13:151-161.
29. Kohonen T. *Self-Organizing Maps*. New York: Springer-Verlag; 3 ed.2001.
30. Wijayasekara D, Linda O, Manic M. CAVE-SOM: Immersive visual data mining using 3D self-organizing maps. In: :2471–2478; 2011.
31. You X, Zhang W. Fault diagnosis of frequency converter in wind power system based on SOM neural network. *Procedia Engineering*. 2012;29:3132-3136.
32. Kramer O, Gieseke F, Satzger B. Wind energy prediction and monitoring with neural computation. *Neurocomputing*. 2013;109:84-93.
33. Gnana Sheela K, Deepa SN. Neural network based hybrid computing model for wind speed prediction. *Neurocomputing*. 2013;122:425-429.
34. Chávez-Arroyo R, Lozano-Galiana S, Sanz-Rodrigo J, Probst O. Statistical-dynamical downscaling of wind fields using self-organizing maps. *Applied Thermal Engineering*. 2015;75:1201-1209.
35. Skamarock W C, Klemp J B, Dudhia J, et al. Description of the Advanced Research WRF version 3. NCAR/TN-475+STR: National Center for Atmospheric Research; 2008.
36. Liu Y, Weisberg RH. Patterns of ocean current variability on the West Florida Shelf using the self-organizing map. *Journal of Geophysical Research, Oceans*. 2005;110:1-12.
37. Reusch DB, Alley RB, Hewitson BC. Relative performance of self-organizing maps and principal component analysis in pattern extraction from synthetic climatological data. *Polar Geography*. 2005;29:188-212.
38. Liu Y, Weisberg RH, Mooers CNK. Performance evaluation of the self-organizing map for feature extraction. *Journal of Geophysical Research, Oceans*. 2006;111:1-14.
39. Annas S, Kanai T, Koyama S. Principal component analysis and self-organizing map for visualizing and classifying fire risks in forest regions. *Agricultural Information Research*. 2007;16:44-51.
40. Astel A, Tsakovski S, Barbieri P, Simeonov V. Comparison of self-organizing maps classification approach with cluster and principal components analysis for large environmental data sets. *Water Research*. 2007;41:4566-4578.

41. Bação F, Lobo V, Painho M. *Self-organizing Maps as Substitutes for K-Means Clustering*. Atlanta: Springer Berlin Heidelberg; 2005:476-483.
42. Lin GF, Chen LH. Identification of homogeneous regions for regional frequency analysis using the self-organizing map. *Journal of Hydrology*. 2006;324:1-9.
43. Lobo VJAS. *Application of self-organizing maps to the maritime environment*. In: *Lecture Notes in Geoinformation and Cartography*. Berlin, Heidelberg: Springer Berlin Heidelberg; 2009:19-36.
44. Hewitson BC, Crane RG. Self-organizing maps: applications to synoptic climatology. *Climate Research*. 2002;22:13-26.
45. Sheridan SC, Lee CC. The self-organizing map in synoptic climatological research. *Progress in Physical Geography: Earth and Environment*. 2011;35:109-119.
46. Liu Y, Weisberg RH. A review of self-organizing map applications in meteorology and oceanography, self organizing maps. In: Mwasiagi JI, *Self Organizing Maps - Applications and Novel Algorithm Design*. London: InTechOpen; 2011:702.
47. Nigro MA, Cassano JJ. Identification of surface wind patterns over the Ross ice shelf, Antarctica, using self-organizing maps. *Monthly Weather Review*. 2014;142:2361-2378.
48. Cassano JJ, Nigro MA, Lazzara MA. Characteristics of the near-surface atmosphere over the Ross ice shelf, Antarctica. *Journal of Geophysical Research - Atmospheres*. 2016;121:3339-3362.
49. Nigro MA, Cassano JJ, Wille J, Bromwich DH, Lazzara MA. A self-organizing-map-based evaluation of the Antarctic Mesoscale Prediction System using observations from a 30-m instrumented tower on the Ross ice shelf, Antarctica. *Weather and Forecasting*. 2017;32:223-242.
50. Katurji M, Noonan B, Zawar-Reza P, Schulmann T, Sturman A. Characteristics of the springtime alpine valley atmospheric boundary layer using self-organizing maps. *Journal of Applied Meteorology and Climatology*. 2015;54:2077-2085.
51. Jolliffe I. *Principal Component Analysis*. In: Springer; 2002 (pp. 1094-1096).
52. Kohonen T. Essentials of the self-organizing map. *Neural Networks*. 2013;37:52-65.
53. Vesanto J, Alhoniemi E. Clustering of the self-organizing map. *IEEE Transactions on Neural Networks*. 2000;11:586-600.
54. Vesanto J, Himberg J, Alhoniemi E, Parhankangas J. SOM Toolbox for Matlab 5. *Technical Report A57*. 2000;2(0):59.
55. Tian J, Azarian M H, Pecht M. Anomaly detection using self-organizing maps-based K-nearest neighbor algorithm. In: :1-9; 2014.
56. Wendel J, Buttenfield BP. Formalizing guidelines for building meaningful self-organizing maps. In: *Sixth International Conference on Geographic Information Science*. 2010; 6.
57. Peiró-Verlet C, Valencia-Peris A, González LM, García-Massó X, Serra-Añó P, Devis-Devis J. Screen media usage, sleep time and academic performance in adolescents: Clustering a self-organizing maps analysis. *PLoS ONE*. 2014;9:e99478.
58. Wu S, Chow TWS. Clustering of the self-organizing map using a clustering validity index based on inter-cluster and intra-cluster density. *Pattern Recognition*. 2004;37:175-188.
59. Vesanto J, Sulkava M. *Distance matrix based clustering of the self-organizing map*. Berlin, Heidelberg: Springer; 2002:951-956.
60. Lampinen J, Oja E. Clustering properties of hierarchical self-organizing maps. *Journal of Mathematical Imaging and Vision*. 1992;2:261-272.
61. Hsu KC, Li ST. Clustering spatial-temporal precipitation data using wavelet transform and self-organizing map neural network. *Advances in Water Resources*. 2010;33:190-200.
62. Nourani V, Baghanam AH, Adamowski J, Gebremichael M. Using self-organizing maps and wavelet transforms for space-time pre-processing of satellite precipitation and runoff data in neural network based rainfall-runoff modeling. *Journal of Hydrology*. 2013;476:228-243.
63. Everitt B, Hothorn T. *An Introduction to Applied Multivariate Analysis with R*. Berlin: Springer Science & Business Media; 2011.
64. Dee DP, Uppala SM, Simmons AJ, et al. The ERA-Interim reanalysis: Configuration and performance of the data assimilation system. *Quarterly Journal of the Royal Meteorological Society*. 2011;137:553-597.
65. Chen F, Dudhia J. Coupling an advanced land surface-hydrology model with the Penn State-NCAR MM5 modeling system. Part I: Model implementation and sensitivity. *Monthly Weather Review*. 2001;129:569-585.
66. Mlawer EJ, Taubman SJ, Brown PD, Iacono MJ, Clough SA. Radiative transfer for inhomogeneous atmospheres: RRTM, a validated correlated-k model for the longwave. *Journal of Geophysical Research - Atmospheres*. 1997;102:16663-16682.
67. Iacono MJ, Delamere JS, Mlawer EJ, Shephard MW, Clough SA, Collins WD. Radiative forcing by long-lived greenhouse gases: Calculations with the AER radiative transfer models. *Journal of Geophysical Research - Atmospheres*. 2008;113(D13). <https://doi.org/10.1029/2008JD009944>
68. Hong S-Y, Dudhia J, Chen S-H. A revised approach to ice microphysical processes for the bulk parameterization of clouds and precipitation. *Monthly Weather Review*. 2004;132:103-120.
69. Kain JS. The Kain-Fritsch convective parameterization: an update. *Journal of Applied Meteorology*. 2004;43:170-181.
70. Janjić ZI. The step-mountain Eta coordinate model: Further developments of the convection, viscous sublayer, and turbulence closure schemes. *Monthly Weather Review*. 1994;122:927-945.
71. Nakanishi M, Niino H. An improved Mellor-Yamada Level-3 model: Its numerical stability and application to a regional prediction of advection fog. *Boundary-Layer Meteorology*. 2006;119:397-407.
72. Nakanishi M, Niino H. Development of an improved turbulence closure model for the atmospheric boundary layer. *Journal of the Meteorological Society of Japan*. 2009;87:895-912.
73. Sukoriansky S, Galperin B, Perov V. Application of a new spectral theory of stably stratified turbulence to the atmospheric boundary layer over sea ice. *Boundary-Layer Meteorology*. 2005;117:231-257.
74. Bretherton CS, Park S. A new moist turbulence parameterization in the Community Atmosphere Model. *Journal of Climate*. 2009;22:3422-3448.
75. Hong S-Y, Noh Y, Dudhia J. A new vertical diffusion package with an explicit treatment of entrainment processes. *Monthly Weather Review*. 2006;134:2318-2341.
76. Hong S-Y. A new stable boundary-layer mixing scheme and its impact on the simulated East Asian summer monsoon. *Quarterly Journal of the Royal Meteorological Society*. 2010;136:1481-1496.
77. Bonner WD. Climatology of the low level jet. *Monthly Weather Review*. 1968;96:833-850.
78. Kent EC, Taylor PK. Choice of a Beaufort equivalent scale. *Journal of Atmospheric and Oceanic Technology*. 1997;14:228-242.

79. Baas P, Bosveld FC, Burgers G. The impact of atmospheric stability on the near-surface wind over sea in storm conditions. *Wind Energy*. 2016;19:187-198.
80. Baas P, Bosveld FC, Baltink HK, Holtslag AAM. A climatology of nocturnal low-level jets at Cabauw. *Journal of Applied Meteorology and Climatology*. 2009;48:1627-1642.
81. Kalverla PC, Steeneveld G-J, Ronda RJ, Holtslag AAM. An observational climatology of anomalous wind events at offshore meteorological mast Umuind (North Sea). *Journal of Wind Engineering and Industrial Aerodynamics*. 2017;165:86-99.
82. Sathe A, Gryning S-E, Peña A. Comparison of the atmospheric stability and wind profiles at two wind farm sites over a long marine fetch in the North Sea. *Wind Energy*. 2011;14:767-780.
83. Peña A, Floors R, Gryning S-E. The Høvsøre tall wind-profile experiment: A description of wind profile observations in the atmospheric boundary layer. *Boundary-Layer Meteorology*. 2014;150:69-89.

How to cite this article: Durán P, Basu S, Meißner C, Adaramola M S. Automated classification of simulated wind field patterns from multi-physics ensemble forecasts. *Wind Energy*. 2020. <https://doi.org/10.1002/we.2462>

APPENDIX A : SOM SENSITIVITY ANALYSIS

In order to determine the optimal structure of the SOM, a sensitivity analysis is conducted in which the dimensions X and Y are systematically varied. The other training parameters are kept the same as the ones used in Section 3.2. Four grid dimensions were tested (with different aspect ratios): (a) 230×10 , (b) 115×20 , (c) 92×25 , and (d) 50×46 nodes. The different SOM solutions were compared with respect to the quantization error (QE) defined in Equation (A1).

$$QE = \frac{\sum_{n=1}^N \min_k \|U_n - w_k\|}{N}. \quad (A1)$$

From Figure 14, it is clear that the grid with dimensions 50×46 leads to the lowest quantization error. Furthermore, in this case, the error decays more rapidly than others after 70 iterations. Based on these findings, we opted to use this SOM structure in the present study.

APPENDIX B : FREQUENCY DISTRIBUTIONS OF AIR-SURFACE TEMPERATURE DIFFERENCE

Atmospheric stability depends on both buoyancy and wind shear. Buoyancy effects can be quantified by the (potential) temperature difference between air and the underlying surface (called air-surface temperature difference or ASTD). With weak to moderate wind speeds, positive (negative) ASTD leads to stable (unstable) condition. Under unstable conditions, both shear and buoyancy effects cause turbulent mixing. In contrast, during stable conditions, turbulence is generated by shear and destroyed by (negative) buoyancy. This competition leads to significantly reduced turbulent mixing under stable conditions. As a matter of fact, for very stable (aka strongly stratified) conditions, the flow becomes quasi-laminar in nature. An atmospheric layer is called neutrally stratified (or simply neutral) when the buoyancy effects can be neglected. Such stability conditions are not very common; albeit, they can arise under two scenarios: (a) very windy conditions (ie, shear generation completely dominates over buoyancy effects) and (b) $ASTD \approx 0$ (ie, virtually negligible buoyancy effects).

In this study, we have computed ASTD based on the WRF model-generated 2 m temperature (T_2) and skin temperature (T_s):

$$ASTD = T_2 - T_s. \quad (B1)$$

For this case, the surface layer is stable (unstable) if ASTD is more (less) than 0.0196 K. In Figures 15-18, the frequency distributions of ASTD for the members of various superclusters are presented. These figures allow us to investigate if certain clusters have any propensity to occur under stable, unstable, or neutral conditions. Please refer to Section 4 for our findings in this regard.

Paper III

A new meso-microscale coupled modelling framework for wind resource assessment: A validation study

Pablo Durán ^{a, b, *}, Cathérine Meißner ^c, Pau Casso ^d

^a Norwegian University of Life Sciences, Universitetstunet 3, Ås, Norway

^b WindSim AS, Fjordgaten 13B, Tønsberg, Norway

^c Wattsight AS, Christian Kroghs gate 16, Oslo

^d Vortex SL, Carrer Marie Curie 14, Barcelona, Spain

* Corresponding author. E-mail address: paduran@nmbu.no

Abstract

In this work the simulation results of a newly developed meso-microscale coupling methodology suited for steady-state computational fluid dynamic models (CFD) are compared with mesoscale and standalone microscale simulations at 5 sites. The coupling methodology uses averaged fields of wind speed and potential temperature simulated by the Weather Research and Forecasting model as boundary and initial conditions for the CFD model. In complex terrain, the coupled model reproduces the measured vertical profiles of horizontal wind speed better than the standalone microscale model or the mesoscale model. The coupled model also performs better in the horizontal extrapolation of measurements in complex terrain. In simpler terrain, it is beneficial to use the coupled model when the focus is on areas located downstream of even small terrain features. Otherwise, the mesoscale simulations perform as good or better than the coupled model.

Keywords: RANS, WRF, Boundary conditions, Mesoscale models, WindSim, Atmospheric stability.

1. Introduction

The main goal of wind resource assessment (WRA) is to find the windiest places within an area of interest. The industry does this by carrying out measurements at different locations in the area and at different heights. Since it is not possible to measure the wind at each point of an area, measurements are required to be extrapolated. Such extrapolation is typically conducted by means of numerical wind flow models, which are designed to predict the spatial changes in the wind due to the orography. Among the wind flow models used for this purpose in the wind industry, the steady-state Reynolds-averaged Navier–Stokes (RANS) models are currently one of the most advanced.¹ RANS models are computational fluid dynamics (CFD) models, which have proven to be more accurate than other popular WRA models as for example linear models, especially in complex terrain.² Despite the existence of more advanced microscale CFD

models, like unsteady RANS or large eddy simulations, steady-state RANS models are still preferred in the wind industry due to their reasonable use of computational resources.³

RANS models consist of a set of governing equations which are derived from time-averaging the fundamental equations that describe the motion of fluids. The steady-state version of RANS provides a description of how the wind changes in space, but not in time, which is sufficient for WRA. The model provides a flow solution for a given set of boundary conditions. A common practice in the wind industry is to use 12 to 36 different boundary conditions, each with a different wind direction. These boundary conditions are commonly computed according to analytical formulas derived from the Monin-Obukhov similarity theory (MOST).⁴ Despite that this has generally been a successful approach, it has important limitations in areas with presence of complex weather systems or mesoscale wind flow circulations, where the wind conditions do not follow this analytical formulation. These shortcomings are commonly addressed with the use of mesoscale meteorological models (MMM). MMM are capable of reproducing mesoscale flow patterns that are relevant for the assessment of the wind resource, like low-level jets, land-sea breeze or mountain-plain circulation systems. Because of the physical assumptions made in MMM, they can only obtain horizontal resolutions down to approximately 1 km. This resolution is insufficient for wind farm design, especially in sites of high terrain complexity, which are becoming increasingly more common as most flat sites are already developed.

The limitations that MMM present for WRA in complex terrain has motivated the coupling of these models with microscale models. In the literature this approach is referred to as mesoscale-to-microscale coupling (MMC). As discussed by Durán et al. (2019),⁵ MMC models are widely studied for planetary boundary layer modelling, wind energy and urban wind flow applications. Nevertheless, little focus has been given to the coupling of steady-state microscale models. Of the few studies that used a steady-state microscale model and that are focused on wind energy, most use analytical boundary conditions and then scale the simulated wind flow by mesoscale wind speed values.^{6,7} This approach can be used for having a first idea about the site conditions if measurements are not available. Therefore, it does not replace the typical WRA scenario in which at least one measurement point is available. In addition, the simulated flow does not include mesoscale features nor the atmospheric stability conditions in the mesoscale simulation. The presented coupling approach contributes in filling this gap by transferring the

wind and temperature conditions simulated by the MMM as boundary conditions (also referred to as direct MMC⁸) to a steady-state microscale model for WRA purposes.

Direct MMC between transient simulations (like MMM) and a steady-state microscale model has to be conducted by running the latter with certain mesoscale fields obtained from the transient simulation. In principle, one should utilize sufficient mesoscale fields to represent the most frequent states of the atmosphere. Therefore, the problem resides in the procedure utilized to carry out this selection. The work of Duraisamy et al. (2014)⁹ deals with this by clustering the mesoscale fields using k-means, obtaining 64 fields. This number of mesoscale fields (and therefore microscale simulations) is still computationally too demanding for the context of wind energy consultancy. In the present paper, we use a much simpler procedure which results in less microscale simulations per site. The procedure is validated for 5 different sites presented in Section 2. The direct MMC methodology used in this study continues the work of Durán et al (2019),⁵ introducing certain corrections for the coupling of the potential temperature. Further details of the MMC approach are given in Section 3. Finally, the simulation results are discussed in Section 4, and the achievements and limitations of the methodology is summarized in Section 5.

2. Experimental set-up

In the following subsections, the validation sites as well as their corresponding datasets are presented. For each site, three types of datasets are available: 1) Onsite wind measurements used to validate the microscale model results, 2) time series of 3-D mesoscale fields, and 3) elevation, forest and roughness maps used to build the digital microscale model. In addition, details about the mesoscale and the microscale simulations are provided. At the end of the section, the validation metric used to compare the results is explained.

2.1. Validation sites

A total of five sites are used in the validation study (see Table 1). These sites belong to commercial wind energy generation projects and therefore details about their name, coordinates and wind speed values are not disclosed. Of the five sites, two are slightly complex with a marked diurnal cycle of wind and temperature (CL and CK), two are flat with stable atmospheric conditions (CA and PL) and one has very complex terrain (CM).

Table 1. Characteristics of the validation sites used in this study.

Name	Location	Terrain	Meteorological conditions	Wind measurements
CM	Southern Cone	Very complex, forested	Near-neutral to atmospheric stable conditions	3 meteorological masts
CA	North America	Flat	Very stable atmospheric conditions	6 meteorological masts
CL	Southern Cone	Semi-complex	Strong day-night cycle	1 meteorological mast 3 LiDAR
CK	Southern Cone	Flat ramp	Strong day-night cycle	2 meteorological masts 3 LiDAR
PS	Southern Cone	Flat, forested	Near-neutral to stable atmospheric conditions	2 meteorological mast

Wind conditions at the sites have been monitored through cup anemometers mounted on meteorological masts and/or Light Detection and Ranging (LiDAR) systems (See Table A1 in the Appendix for detailed monitoring information per site). For the monitored time periods, ten-minute averages of horizontal wind speed and wind direction are available. In Figure 1, the wind rose for one of the instruments at one selected height is presented for each site. Most of the sites used in this study have one to three very dominant wind directions. The only exception is CA, which has a more spread distribution.

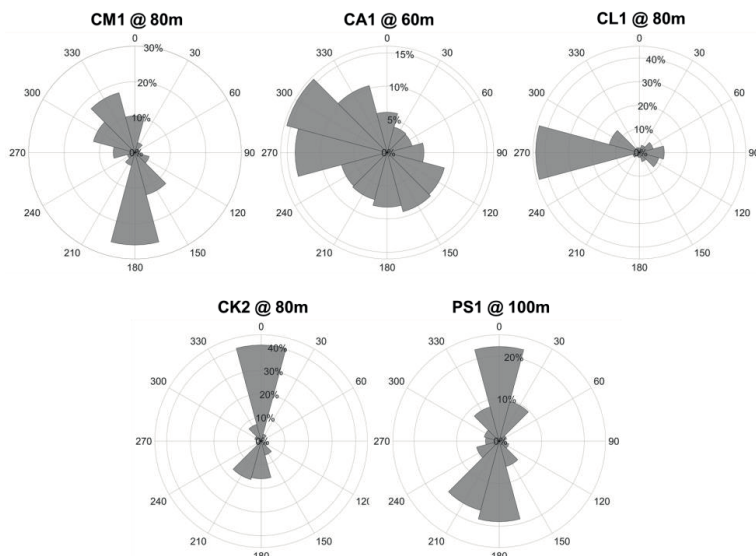


Figure 1. Wind roses at the studied sites. At the top of each panel, the name of the instrument and the height used to compute the wind rose is displayed.

2.2. WRF simulations

In this study, WRF version 3.7.1¹⁰ is forced with the ERA-5 reanalysis dataset with a model spin-up time of 12 hours. One-year worth of data is produced for each site. The simulated timespan was selected in order to cover the longest concurrent measured period among all measurements in the site (Table 2). Four nested domains with one-way coupling are used in the simulation. Domains 1, 2, 3 and 4 employ a horizontal resolution of 27 km, 9 km, 3 km and 1 km, respectively. Grid nudging is activated for model levels above the vertical level 23 (≈ 2 km). The integration time-steps are 180 s, 90 s, 45 s, and 15 s for domains 1, 2, 3 and 4, respectively. In all the domains, 51 vertical levels are used, with the highest resolution towards the ground. The lowest model level is at ~ 8 m above ground level (a.g.l.) and approximately 6 vertical levels are below 140 m a.g.l. The output is stored every hour for the domain 4.

Table 2. Timespan of the WRF simulations conducted for each site.

Site	Simulated period (month/year)
CM	01/2014 – 12/2014
CA	04/2016 – 03/2017
CL	12/2015 – 12/2016
CK	10/2013 – 10/2014
PS	10/2015 – 10/2016

The following physics parameterizations are utilized: (i) land surface: Noah scheme;¹¹ (ii) shortwave and longwave radiation: Rapid Radiative Transfer Model for Global Climate Models scheme;¹² (iii) microphysics: WRF Single-Moment 5-class scheme¹³; (iv) cumulus: modified Kain-Fritsch scheme (only for domains 1 and 2)¹⁴; and (v) planetary boundary layer (PBL) scheme: Mellor-Yamada-Nakanishi-Niino level 2.5¹⁵.

2.3. Microscale steady-state CFD model

The WindSim software is used to simulate the wind flow in the microscale model domain. WindSim's CFD model is based on RANS equations for momentum, turbulence and temperature, assuming steady-state and incompressible flow.^{16,17} The standard $k-\varepsilon$ model¹⁸ is used as a turbulence closure. Forest is modelled as formulated by Sanz (2003).¹⁹ Thermal effects are taken into account in both the momentum and the turbulence equations of the model. In the latter, a source/sink term is added, which corresponds to the buoyant turbulence production P_b and is calculated as follows:

$$P_b = -\frac{v_T}{\sigma_\theta \theta_0} g \frac{\partial \theta}{\partial z} \quad (1)$$

For very stable conditions ($\frac{\partial \theta}{\partial z} \gg 0$), Equation (1) prevents sufficient generation of turbulence in the model. For this reason, P_b is in this study limited by $P_b = \max(Rf_c \times P_k, P_b)$ in the turbulent kinetic energy (TKE) equation and by $P_b = \max(0, P_b)$ in the TKE dissipation rate (EDR) equation.^{20,21} Here P_k is the shear production of turbulence and $Rf_c = 0.25$ for the model constants used in WindSim.¹⁶

Details of the microscale digital terrain models of the validation sites are presented in Table 3. For some sites, a variable horizontal resolution was used, with a coarser resolution towards the boundaries of the domain and finer resolution towards the area of interest. The extent of the domain and its grid resolution were chosen following the recommendations of the software provider. In general terms, the horizontal resolution was set according to the complexity of the terrain and the vertical extent of the grid is chosen to prevent blocking effects that could artificially accelerate the wind flow. The vertical resolution of the grid is refined towards the ground, having more than 8 levels within the first 100 m.

Table 3. Details of the terrain digital model used for the microscale simulation for each studied site.

Site	Domain extent (km)	Horizontal resolution (m)	Vertical extent (m)	Vertical levels	Dataset	
					Elevation	Land cover
CM	18.7 x 12.1	20 – 128	4000	50	LiDAR campaign, commercial source, SRTM	GLC30
CA	22 x 23	50	1000	22	CDED1	NLCD 2001
CL	13.6 x 10.2	40	2000	60	LiDAR campaign, WorldDEM™, SRTM	Constant value
CK	11 x 20	40 – 170	4000	60	SRTM	Constant value
PS	16 x 16	40 – 160	1000	60	LiDAR campaign, WorldDEM™, SRTM	WorldDEM™

Data about the elevation of the sites was obtained from the Shuttle Radar Topography Mission (SRTM)²² or the Canadian Digital Elevation Data Level 1 (CDED1)²³ databases. For most sites, the SRTM dataset was combined with commercial digital terrain models and aerial LiDAR surveys. The roughness length and forest model were prescribed according to the land cover data obtained from the GlobeLand30 (GLC30) dataset,²⁴ the US National Land Cover Database (NLCD) 2001,²⁵ commercial sources or a combination of these. In some cases, a constant

roughness value was used across the domain. The roughness maps of the sites were adjusted by visual inspection from satellite imagery and/or visits in terrain.

2.4. Validation metric

Steady-state wind flow models are used in WRA to extrapolate observational data to potential locations of wind turbines. This extrapolation is conducted by multiplying the measured wind speeds at the observational point by a factor, the so-called speed-up ratio (SU). The SU is predicted by the model and is calculated as:

$$SU(R, T) = \frac{u_T}{u_R} \quad (2)$$

Here u_R and u_T correspond to the simulated wind speed at a reference (R) and a target (T) location, respectively. When conducting wind energy estimations, R corresponds to a measurement point and T to a potential wind turbine location. Since real terrain is typically asymmetric, the SU values are dependent on the direction of the wind. Therefore, one SU is obtained per simulated wind direction which is denoted as $SU_\alpha(R, T)$, where α is the direction of the wind. In practice, the wind direction at R will not be the same as at the inlet of the simulation domain. Therefore, for each timestep the SU is calculated by interpolating the $SU_\alpha(R, T)$ of the two simulated directional sectors that have wind directions at R that are closest to the measured one. It is assumed that the speed up ratios are independent of the wind speed values, which holds true for most operational conditions of wind turbine generators.^{26,27}

To evaluate the ability of the models to accurately extrapolate observations, the crosscheck prediction error XPE is utilized, which is defined as:

$$XPE_\alpha(R, T) = \frac{\overline{SU_\alpha(R, T)} \times \overline{u_{R\alpha}} - \overline{u_{T\alpha}}}{\overline{u_{T\alpha}}} \quad (3)$$

In this case, R and T correspond to a reference and a target measurement, respectively. One value of $XPE_\alpha(R, T)$ is obtained per pair of measurements and per wind direction. In order to facilitate the analysis of the XPE s, their absolute values are averaged per directional sector, obtaining the absolute crosscheck prediction errors:

$$AXPE_\alpha = \frac{\sum_{R, T \in M; R \neq T} |XPE_\alpha(R, T)|}{N_M} \quad (4)$$

Here M is the set of observational points used to compute the errors and N_M is the total number of observational points.

3. Boundary conditions of CFD simulations

For WindSim's CFD model, boundary conditions for wind velocity components (U_x, U_y, U_z), potential temperature θ , TKE and EDR have to be prescribed for each of the selected wind directions. Simulations in which analytical formulations of these boundary conditions are used, will hereafter be referred to as "standalone" simulations. For the coupled simulations, these boundary conditions will instead be prescribed according to the output obtained from the mesoscale model. In the following subsections, details of how these boundary conditions are prescribed for each case are provided.


3.1. Standalone boundary conditions

For standalone simulations, analytical formulations are used to compute the boundary conditions, assuming a certain wind direction for the wind velocity vector. These formulations correspond to vertical profiles that are derived from the Monin-Obukhov similarity theory⁴ and from the work of Han et al. (2000).²⁸ The calculation of horizontal wind speed $u (= \sqrt{U_x^2 + U_y^2})$ is used to then prescribe $U_x = u \cos(\beta)$ and $U_y = u \sin(\beta)$, with $\beta = \arctan \frac{U_y}{U_x}$. The vertical component is simply prescribed as $U_z = 0$. Further details of the equations for u , θ , TKE and EDR are presented in Durán et al. (2019).⁵

The boundary conditions of standalone simulations take into account the atmospheric stability by the Monin-Obukhov length L . Varying L changes the shape of the vertical profile of u , θ , TKE and EDR. For $|L| \geq 1000$ the atmospheric stability is considered to be neutral. Outside of this range, $L > 0$ ($L < 0$) correspond to stable (unstable) conditions. In Table 4, the values of L used for the standalone simulations for each of the studied sites are presented. Another variable that has an important effect on the prescribed vertical profiles is the PBL height h (Table 5). It is known that L and h are correlated, where stable (unstable) values of L correspond to smaller (higher) values of h . The values of Tables 4 and 5 were chosen according to the observed conditions at each site.

Table 4. Values of L used to compute the boundary conditions of the standalone microscale simulations.

Site	Directional sector											
	0°	30°	60°	90°	120°	150°	180°	210°	240°	270°	300°	330°
CM	200	200	100	100	200	200	200	∞	∞	∞	∞	∞
CA	400	400	400	∞	400	200	400	200	200	200	∞	∞
CL	∞	400	150	50	50	150	150	-200	-200	-200	-200	-50
CK	-1000	-50	-50	-50	-50	-50	-20	-20	-20	-20	-20	-50
PS	80	60	60	100	100	100	120	60	80	100	150	120



Very unstable Unstable Neutral Stable Very stable

Table 5. Values of h used to compute the boundary conditions of the standalone microscale simulations. Higher values are colored darker.

Site	Directional sector											
	0°	30°	60°	90°	120°	150°	180°	210°	240°	270°	300°	330°
CM	500	500	500	500	500	500	500	500	500	500	500	500
CA	400	400	400	500	400	400	400	400	400	400	500	500
CL	500	500	300	200	200	300	300	600	600	600	600	1000
CK	500	1000	1000	1000	1000	1000	1000	1000	1000	1000	1000	1000
PS	200	100	100	200	200	200	200	100	200	200	200	200

3.2. Meso-to-microscale coupling simulations

The procedure to generate boundary conditions for the coupled simulations consists of two steps. First, the mesoscale timesteps are averaged by their wind direction. Secondly, the averaged mesoscale fields (one per selected wind direction) are transferred to the microscale model. Further details for both procedures are provided in the following subsections.

3.2.1 Computation of representative atmospheric conditions

Representative atmospheric conditions are generated by averaging the mesoscale fields for each of the selected wind directions. It is expected that such an approach can capture the mean or most predominant wind condition, like wind shear, wind veer and atmospheric stability, at the site for a given wind direction. First, all the mesoscale timesteps are filtered out for which the average wind speed is below 3 m/s for all grid points within the microscale domain and between 75 and 100 meters a.g.l. With this criterion it is possible to disregard timesteps which are not of interest for the wind energy generation. After the filtering, the remaining timesteps of the mesoscale simulation are classified according to their wind direction (Figure 2a). Given that within a mesoscale field the wind may have different directions at different locations, there is not a unique way to classify the timestep. In this study, the wind direction of the mesoscale

field corresponds to the average wind direction of all mesoscale grid points that are closest to the inlet of the microscale domain and that are between 60 and 160 meters a.g.l.

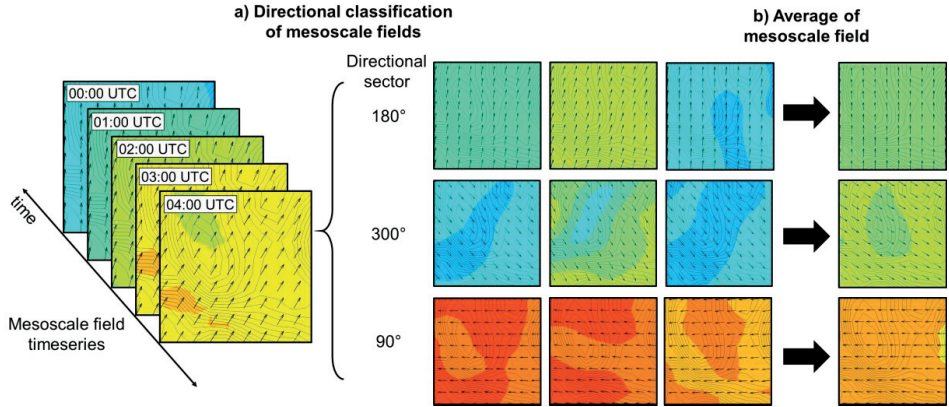


Figure 2. Averaging procedure to generate representative mesoscale fields per wind direction.

Mesoscale fields corresponding to the same directional sector are averaged to produce one mesoscale field per wind direction (Figure 2b). The variables of the mesoscale field that are of interest for the coupling procedure are U_x , U_y , U_z , θ and h . The variables U_x and U_y are not directly averaged. Instead u and β are separately averaged to then compute the average horizontal components of the wind as $\bar{U}_x = \bar{u} \cos(\bar{\beta})$ and $\bar{U}_y = \bar{u} \sin(\bar{\beta})$. This is to prevent the wind from being misrepresented due to the variability in the wind direction between the timesteps. In the case of the potential temperature, the values of $\Delta\theta = \theta - \theta_0$ and θ_0 are averaged, where θ_0 corresponds to θ at the lowest vertical level. Then, the average potential temperature field is computed as $\bar{\theta} = \overline{\Delta\theta} + \bar{\theta}_0$. This way, the information about the atmospheric stability (contained in $\Delta\theta$) is not distorted by the absolute temperatures. U_z and h are directly averaged.

The proposed procedure works well for not too stable atmospheric conditions. When the atmosphere is very stable the obtained averaged potential temperature gradient in the lowest few hundred meters can be quite high (Figure 3). That leads to very low TKE values in the CFD model and unrealistic low mixing between the atmospheric layers. In a real observed stable boundary layer that would not occur as there is still some sporadic and patchy mixing.²⁹ This is a transient phenomenon that a steady-state CFD model cannot reproduce. Therefore, to

obtain a higher vertical mixing in the CFD model, a filtering strategy to the WRF temperature fields with stably stratification is proposed in order to average only some of the $\Delta\theta$ fields. The filtering of each averaged mesoscale field is conducted as follows:

1. The Monin-Obukhov length of each mesoscale timestep $L(t)$ is calculated at the middle of the microscale domain by means of the gradient method³⁰ using the two lowest vertical levels.
2. The mean Monin-Obukhov length per directional sector is calculated as:

$$L_m = \left(\frac{\sum_{t \in T_\alpha} \left(\frac{1}{L(t)} \right)}{N_\alpha} \right)^{-1}$$

Here T_α corresponds to the set of mesoscale timesteps with wind direction, where N_α is the number of timesteps at sector α .

3. Using L_m and the average mesoscale wind speed at the two lowest vertical levels (typically @ 10 and 30 m) in the middle of the domain in the MOST equations, a value of the mean potential temperature gradient $\Delta\theta_{th}$ is calculated for each sector.
4. Mesoscale timesteps of $\Delta\theta$ fields are averaged in such a way that the averaged field has a potential temperature at the middle of the microscale domain $\Delta\theta_{mid}$ which is close to $\Delta\theta_{th}$. The selection of the $\Delta\theta$ fields starts from $\Delta\theta_{mid}(z)$ values closer to zero to higher values. z is selected in such way that there is a good agreement close to the ground between an analytical profile and the averaged vertical profile of potential temperature (Figure 3).

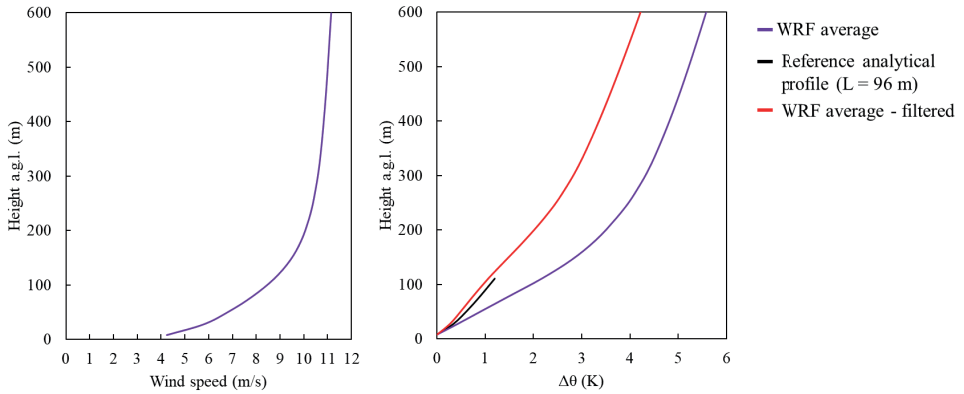


Figure 3. Vertical profiles of wind speed and $\Delta\theta$ at the middle of the microscale domain at the CA site for sector 270°.

3.2.2 Coupled boundary conditions

After representative mesoscale fields are computed for each directional sector, they are transferred to the microscale model as boundary conditions. This is done by interpolating the 3-D mesoscale fields of U_x , U_y , U_z and θ onto the microscale grid. Cubic spline, and after that, bilinear interpolation is utilized for vertical and horizontal directions. Cubic spline interpolations for U_x , U_y , U_z are conducted with respect to the height a.g.l, while for θ the interpolations are conducted with respect to the height a.s.l. instead. TKE and EDR are prescribed using the same analytical formulations as for the standalone model using the values of L that are obtained by the gradient method³⁰ with the two lowest vertical levels of the mesoscale field and the interpolated h . For some grid points of the mesoscale field, it may not be possible to calculate L with this method.³¹ In these cases, L is computed from the inverse of the average $1/L$ of the surrounding grid points.

A few grid cells of the microscale domain may be located under the lowest vertical level of the mesoscale field. For these grid points, the values are vertically extrapolated using the MOST equations and horizontally interpolated with the bilinear method. Similarly to Veiga et al. (2016),³² mass conservation is enforced by correcting the normal velocities at the boundaries of the domain. Further details of the equations used in this subsection are provided by Durán et al. (2019).⁵

4. Results

Five different modeling set-ups are compared, which are defined in Table 6. Twelve equidistant directional sectors are simulated for each set-up. An advantage of the coupled simulations compared to the standalone simulations is that there is no need for assumptions made about the boundary conditions. This is an advantage for modelers as the proper setting of the physical parameters of analytical boundary conditions may require a tuning phase, which can be difficult in sites with complex weather patterns. Furthermore, in coupled simulations it is possible to prescribe atmospheric stability, wind shear and wind veer that varies within the microscale domain.

Table 6. Different model set-ups for all sites.

Result name	Description
WRF-Av	Directionally averaged WRF simulations
WS	Standalone WindSim simulations
CPL-NT	Coupled simulations without thermal effects
CPL	Coupled simulations
CPL-FT	Coupled simulations with filtered temperature

The directionally averaged WRF results (WRF-Av) correspond to the mesoscale data without downscaling. They are used as reference case to decide if there is an improvement when downscaling these averaged fields with the CFD model. The standalone WindSim results (WS) are used to judge if the coupled approaches are better than the common way steady-state RANS models are run for WRA. Three coupled approaches are compared, one with neutral atmospheric conditions (CPL-NT) and two with temperature coupling (CPL and CPL-FT). The CPL approach uses the θ fields directly, while the CPL-FT approach uses a filtered θ field, as described in subsection 3.2.1.

4.1. Downscaling of mesoscale wind flow patterns

A major motivation for using coupled models is the interest in downscaling mesoscale weather patterns. In this study, the ability to downscale three wind patterns are investigated: horizontal wind speed patterns, strong horizontal wind turning and low-level jets (LLJ). These patterns were reproduced by the mesoscale model and then downscaled in the coupled simulations.

4.1.1 Horizontal wind field patterns

In Figure 4, the horizontal planes of wind speed are presented for each of the model set-ups in Table 6. For the directional sector 150° , the WRF-Av result shows a wind speed pattern with a low wind area in the southern part of the CM site and a high wind speed area at the northern part of the site. This wind speed pattern is sustained in the CPL and CPL-FT results, which modify the WRF-Av pattern by simulating more detailed flow features caused by the more detailed orography. The CLP-NT simulation sustains the WRF-Av pattern only close to the western boundary of the domain, but it is not kept at most of the site. This suggests that the inclusion of atmospheric stability effects in the CFD model is necessary in complex terrain to properly downscale the mesoscale pattern. By comparing the coupled simulations with the WS simulation, it is clear that the wind speed patterns in the CPL simulations are produced by the

information provided by the mesoscale. At the southern part of the domain, the WS simulation has much higher wind speeds in the southern part than the WRF-Av and CPL simulations.

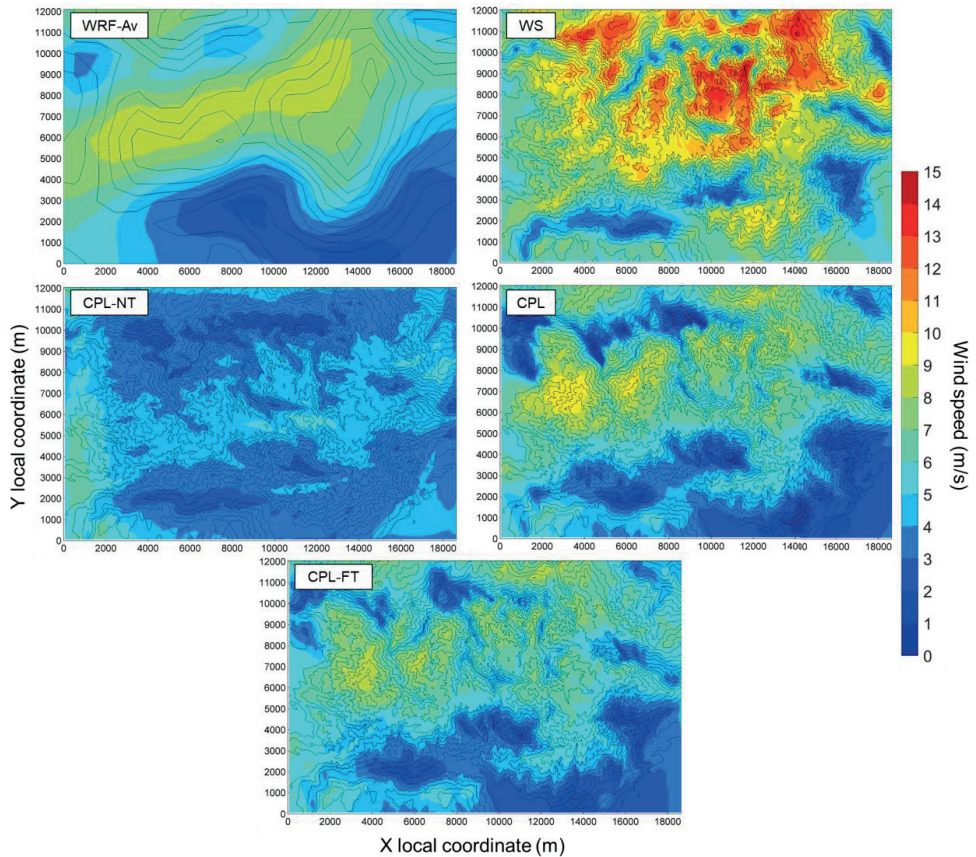


Figure 4. Horizontal planes of wind speed @ ~100 m from sector 150° at the CM site for the model set-ups in Table 6. The black lines in the map correspond to the contour lines of terrain elevation for every 50 m.

4.1.2 Horizontal wind turning

Mesoscale models are capable of reproducing horizontal wind turning that is caused by a combination of factors like atmospheric stability, Coriolis force, horizontal pressure gradients and/or baroclinity effects. The coupled models can downscale these wind direction shifts into the microscale flow field (Figure 5). Without coupling, microscale models are only capable of reproducing wind turning induced by the complexity of the terrain and by atmospheric stability. This limits the wind turning that can be modelled by standalone microscale models compared

to mesoscale models. Therefore, it is important that the coupled model is capable of properly downscaling the wind turning simulated in the mesoscale model.

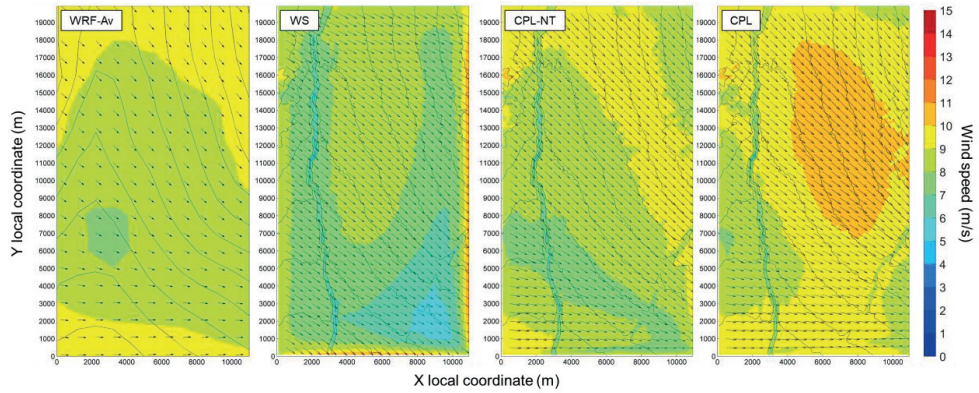


Figure 5. Horizontal planes of wind speed @ ~100 m from sector 300° at the CK site for the model set-ups in Table 6. The black arrows indicate the direction of the wind. The black lines in the map correspond to the contour lines of terrain elevation for every 50 m. The result CPL-FT is not displayed as it is identical to CPL.

In Figure 5, the wind turning is downscaled by the CPL-NT and CPL results. Since there are not any complex terrain features at the site, the WS result is not capable to produce wind turning at all. In the case of CPL-NT, the wind turning is similar to the WRF-Av pattern except at the southern part of the site, where no turning is produced. The CPL wind turning pattern is very similar to the one produced by the mesoscale model. This indicates that the coupling of potential temperature is important to reproduce the wind turning simulated by the mesoscale model in the microscale model.

4.1.3 Low-level jets

LLJs cause strong changes in wind shear over small parts of the lower atmospheric boundary layer which translates into high loads on the wind turbines. It has been reported that the WRF model can reproduce LLJs.^{33,34} The coupled models that consider thermal effects are able to downscale the LLJ shape produced by the WRF for the CK site (Figure 6). The LLJ pattern cannot be simulated using the analytical boundary conditions, as shown in the WS result. In the case of CPL-NT, the LLJ shape is barely visible, which confirms the importance of thermal effects in order to reproduce LLJs. For CPL the LLJ appears to be wider and more elongated than in WRF-Av.

From the above results, assuming that the mesoscale model can reproduce the height and shape of the LLJ properly, it is expected that the performance of the coupled model would be better for vertical wind speed extrapolation than a standalone approach. It has been shown that despite that WRF models can reproduce the location and time of LLJs, they typically fail in reproducing the height and jet speed.³³ Here a coupled model might improve the results. For this study, the measured heights at CK are not high enough to validate the LLJ.

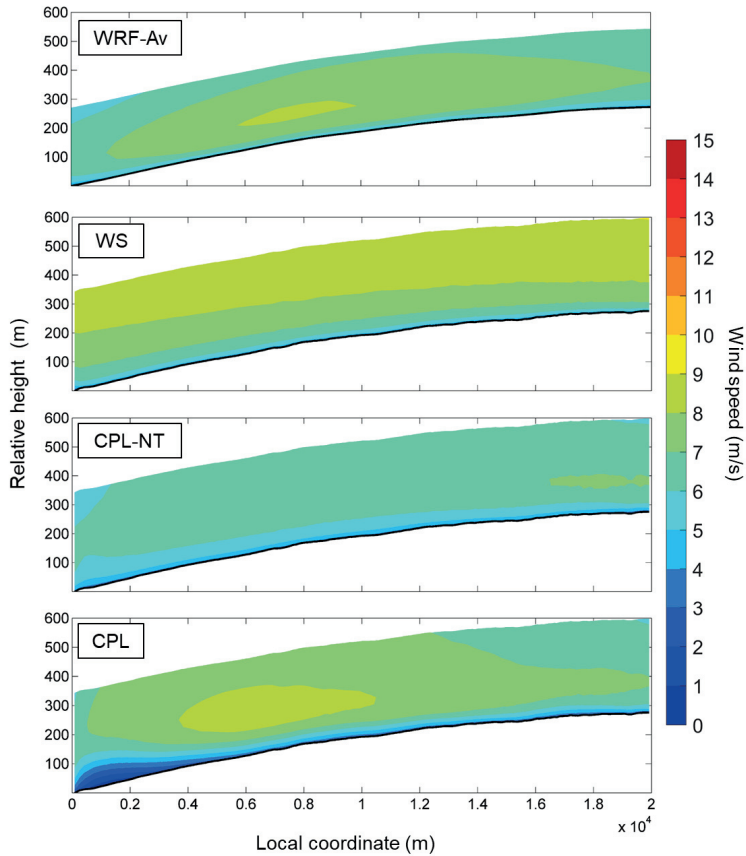


Figure 6. Vertical planes of wind speed from sector 0° at the CK site for the model set-ups in Table 6. The black line corresponds to the terrain height of their corresponding digital terrain model. The vertical plane is located approximately at the middle of the domain and spans from north to south. The CPL-FT result is not displayed as it is identical to CPL.

4.2. Validation results

The accuracy of the model set-ups to extrapolate the measurements in the horizontal and vertical direction are evaluated by means of calculating the $AXPE_\alpha$ values explained in section

2.4. In general, the vertical extrapolation results of the WRF simulations (WRF-Av) are improved when they are downscaled by a coupled model (Figure 7). This improvement is very consistent for complex (e.g. CM) and semi-complex sites (e.g. CK and CL). For CA, which is very flat and very stably stratified, the WRF-Av result performs better, but nevertheless with small differences compared with coupled results. In the case of horizontal extrapolation, the coupled models perform better for complex terrain. However, for the rest of the sites the performance of the results depends on the site. As expected, the performance of the coupled models depends on the performance of the mesoscale simulation. This means that the improvements that a coupled model can provide will necessarily depend on the quality of the WRF modelling. This is especially important to consider for directional sectors with low occurrence. As shown in Figure 7, sectors with low frequency ($< \sim 10\%$) tend to have higher crosscheck prediction errors.

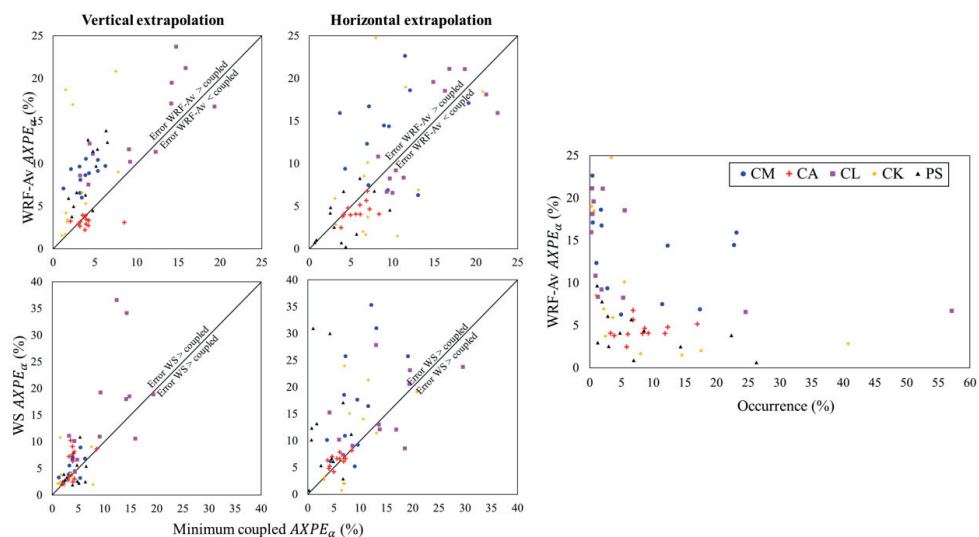


Figure 7. Left and center panels: comparison of crosscheck error prediction errors between coupled, WRF-Av and WS simulations. Right panel: dependence of horizontal errors with the occurrence of the directional sector for WRF-Av simulations.

Differences between coupled and standalone simulations for vertical extrapolations are relatively small, as the latter uses analytical profiles whose parameters were adapted to the observed profiles. In some sectors, the WS simulations is not able to reproduce the non-analytical shapes observed, like for example very high wind shears at CA or very low shear profiles observed at CL. In the case of horizontal extrapolations, the coupled models perform

better than the WS simulation for most sectors. Depending on the sector, these differences are product of improper atmospheric stability conditions in the standalone model (due to limited information) or due to the influence of mesoscale patterns that are very different to the analytical formulations. Further details of the simulation results are discussed in the following subsections. In order to facilitate the discussion, only directional sectors with a frequency higher than 5% are discussed.

4.2.1 Horizontal extrapolation errors

The average of the absolute values of the horizontal crosscheck prediction errors ($AXPE_{\alpha}$) for the main wind directions are shown in Figure 8. The error calculation is conducted using all the available measurements at the selected height. This height is chosen to be the highest common measurement height for all the measurement locations at the site.

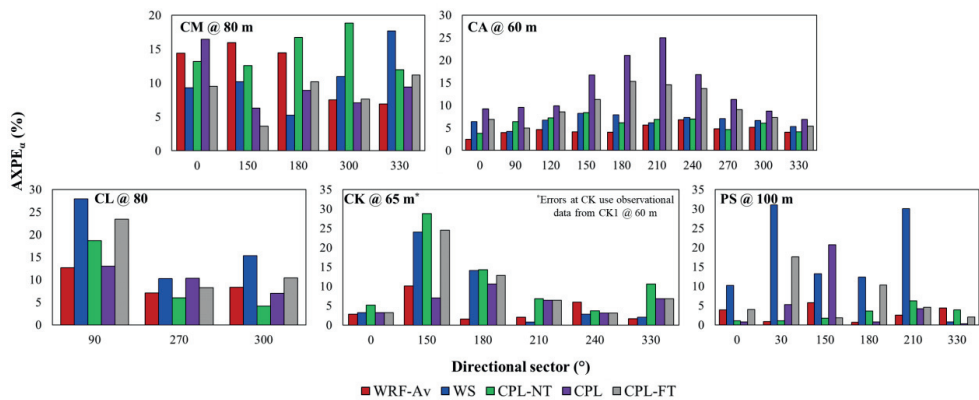


Figure 8. Horizontal crosscheck prediction errors for the main wind direction sectors at the studied sites. The site and the height a.g.l. used to compute the errors is indicated in the top-left corner of each panel.

For most sectors in CM, the results of the coupled simulations are as good or better than the WRF-Av, showing the benefits of using a model with higher resolution in complex terrain. The only exception is the CPL-NT simulation, which is expected as thermal effects influence the wind flow in complex terrain and under stable atmospheric conditions. For the sectors 150° , 180° and 300° (23%, 22% and 11% of occurrence, respectively) the CPL and CPL-FT simulations seem to successfully downscale the mesoscale pattern, as previously presented in Figure 4. CPL-FT also performs well in sector 0° , while CPL does not. Most of the error of the CPL results at 0° is due to underestimated wind speeds at the flat area in the center of the domain compared to the wind speed modeled at the top of the ridges located at ~ 6 km and ~ 13

km east of the flat area, where measurements are located (Figure 9). Despite that the errors in sectors 300° and 330° are similar for WRF-Av and CPL, the latter has the advantage of including finer features in the wind flow (Figure 9). WS results also present finer features and better performance in most of the main sectors compared to WRF-Av. Nevertheless, it is not as good as the CLP and CPL-FT results, which highlights the importance of the mesoscale effects at this site.

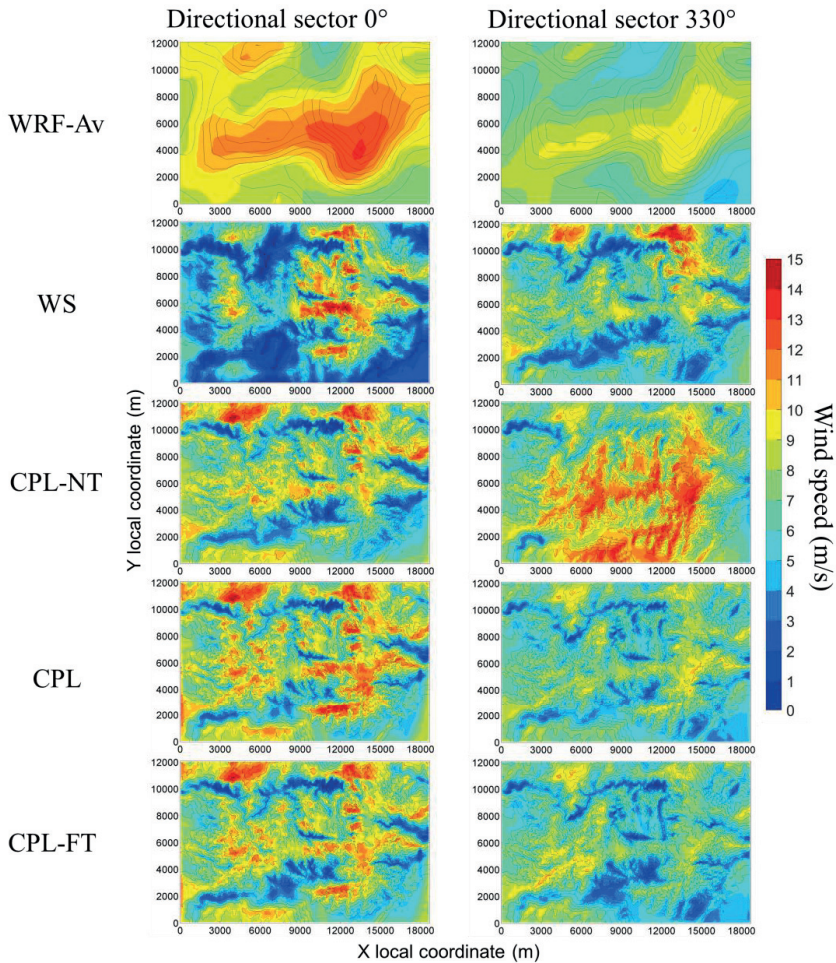


Figure 9. Horizontal planes of wind speed @ 80 m from sectors 0° (left panels) and 330° (right panels) at the CM site for the results in Table 6. The black lines in the map correspond to the contour lines of terrain elevation for every 50 m.

At the CA site, the WRF-Av results have in general the best performance, while the CPL results have the worst performance. The bad performance of the CPL results is caused by very stable atmospheric conditions that are transferred from the mesoscale. As a consequence, turbulence is too low in the microscale model (Figure 10), preventing the transfer of momentum downwards and causing a decrease of wind speed close to the ground inside the domain (Figure 11). This problem is slightly compensated when using the filtered potential temperature field in the CPL-FT results. By completely ignoring the potential temperature, as in CPL-NT, this problem disappears. For some sectors, like 150° , the WRF-Av reproduces a complex wind pattern which is not maintained by neither the CPL nor the CPL-FT model (Figure 11). It is also not possible to reproduce these kinds of patterns with analytical boundary conditions as in WS.

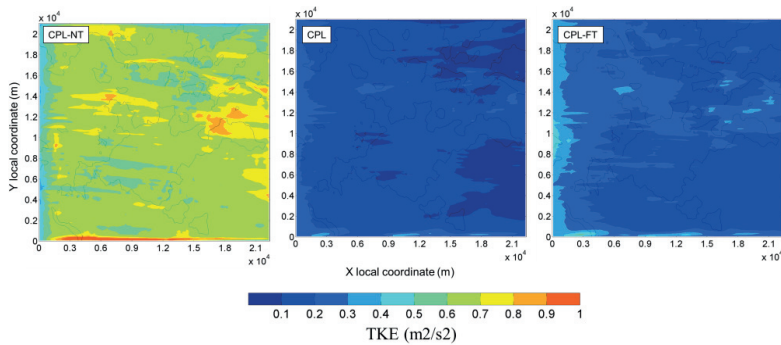


Figure 10. Horizontal planes of TKE @ 60 m from sector 270° (bottom panels) at the CA site for the coupled results. The black lines in the map correspond to the contour lines of terrain elevation for every 50 m.

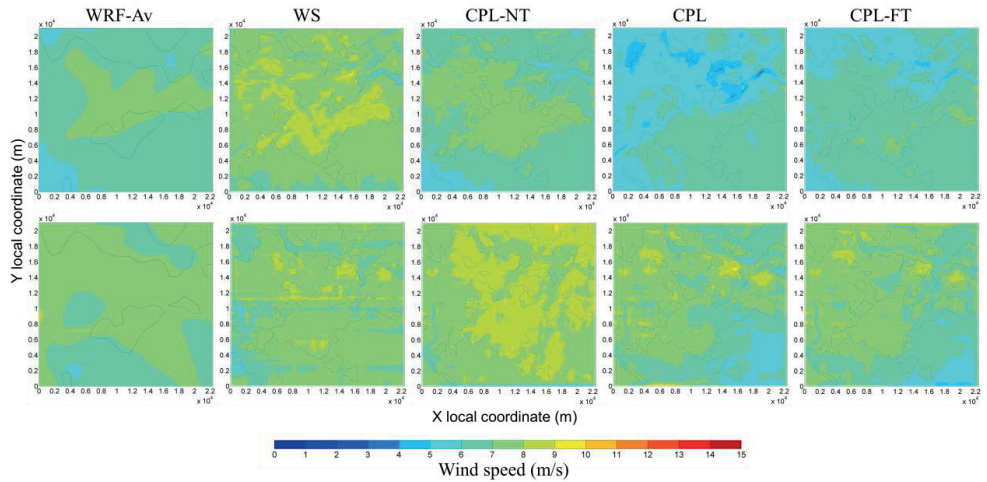


Figure 11. Horizontal planes of wind speed @ 60 m from sectors 150° (top panels) and 270° (bottom panels) at the CA site for the set-ups in Table 6. The black lines in the map correspond to the contour lines of terrain elevation for every 50 m.

In the CL site the horizontal patterns of wind speed vary significantly between the WRF-Av results and the other results that use the microscale model. Even for the coupled results, the wind field is considerably modified in the northeast part of the site, where an area of relatively high wind speeds in the WRF-Av is not reproduced by the other models. These differences are due to the fact that the microscale model is only able to maintain mesoscale patterns which are enforced from the inlets of the domain. Mesoscale patterns which are only visible inside the microscale domain or at the outflow boundaries are difficult to maintain in the CFD model. In addition, the wake of the hill at the center of the domain, modifies the microscale wind pattern for sectors 270° and 330° (58% and 25% of occurrence, respectively) at the eastern part of the domain compared to the WRF results. Despite that different wind flow patterns in CL are produced by the different models, their performance in terms of crosscheck prediction error is very similar, as the wind speed does not vary a considerable between the models in the area where measurements are available.

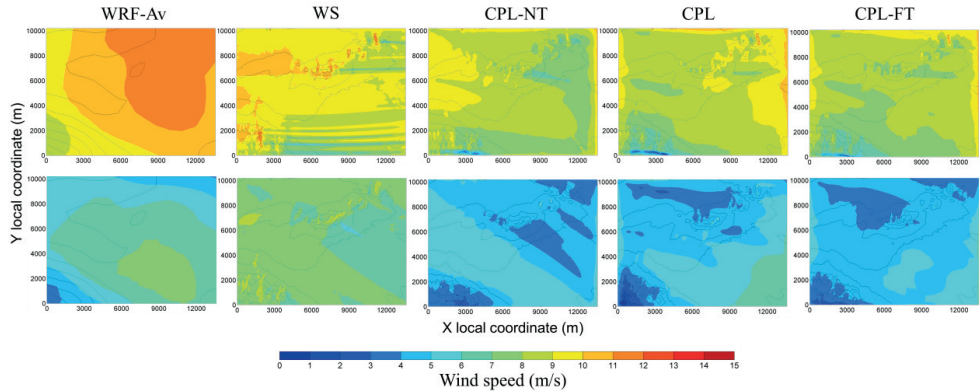


Figure 12. Horizontal planes of wind speed @ 80 m from sectors 270° (top panels) and 300° (bottom panels) at the CL site for the set-ups in Table 6. The black lines in the map correspond to the contour lines of terrain elevation for every 50 m.

In the sector 0° at CK (40% of occurrence) the different models have similar performances. Despite that their wind speed patterns have important differences, all of them present near-constant wind speed values within the middle part of the domain, where measurements are available (top row of Figure 13). The CPL-NT simulation has the highest error, which is caused by a stronger wind speed gradient over this part of the domain. Similar to the CM site, this confirms the importance of transferring the potential temperature when stable conditions are present at non-flat sites. For the sectors 180°, 210°, 240° and 330° the WRF-Av fields at CK present complex mesoscale circulations with strong wind direction changes (like in Figure 5), while also obtaining the lowest horizontal extrapolation errors (except for sector 240°). For these sectors the coupled models were not capable of maintaining the mesoscale features in the wind flow. In the case of sector 240°, the results using the microscale model have the best performance since they take into account the effect of the river located in the western part of the site (bottom row of Figure 13).

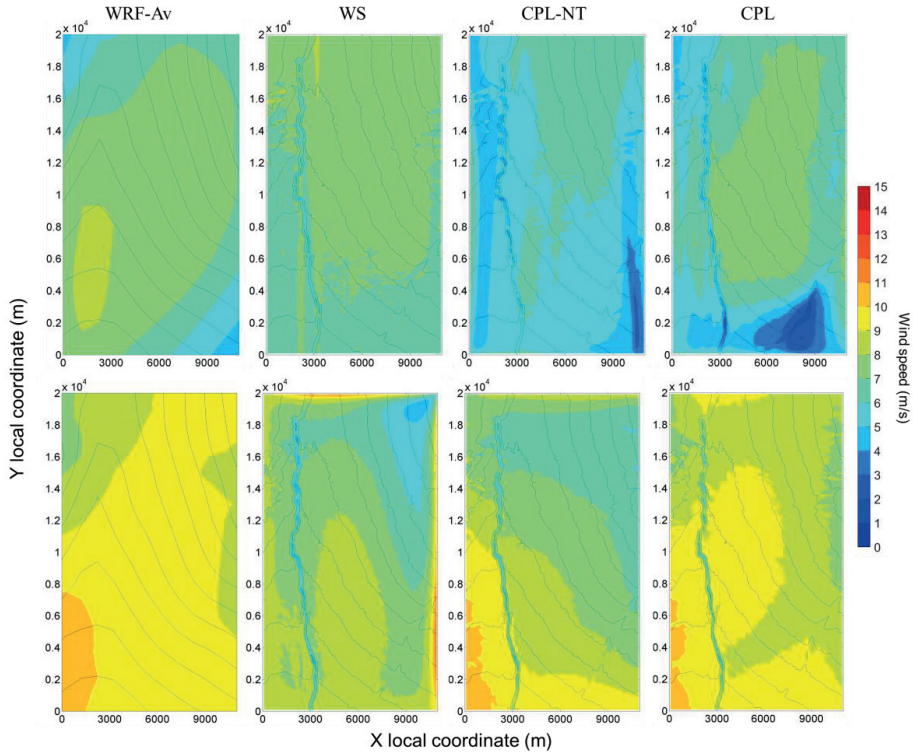


Figure 13. Horizontal planes of wind speed @ 65 m from sectors 0° (top panels) and 240° (bottom panels) at the CK site for the set-up in Table 6. The black lines in the map correspond to the contour lines of terrain elevation for every 50 m. The CPL-FT results are not displayed as they are identical to CPL.

At most simulated sectors of PS, the errors are relatively small for all models, except for WS. This suggests that this site is significantly influenced by mesoscale effects. For sector 0° (22 % of occurrence) the downscaled models have small crosscheck prediction errors, with CPL and CPL-NT having the smallest errors. These models perform better than the others as they produce near-constant wind speed in the center and center-left part of the domain. In the case of CPL, the wind pattern is influenced by the blocking effect produced by the ridge that extends from the south to the east part of the site. In the case of CPL-NT the pattern looks similar to the WRF-Av result, but with more detailed features of the terrain. For sector 150° (6 % of occurrence) the modelled effect of the same ridge determines the performance of each model. In this sector, the simulations that consider atmospheric conditions closest to neutral (CPL-NT and CPL-FT) have very small errors. The opposite is true for the WS and CPL results.

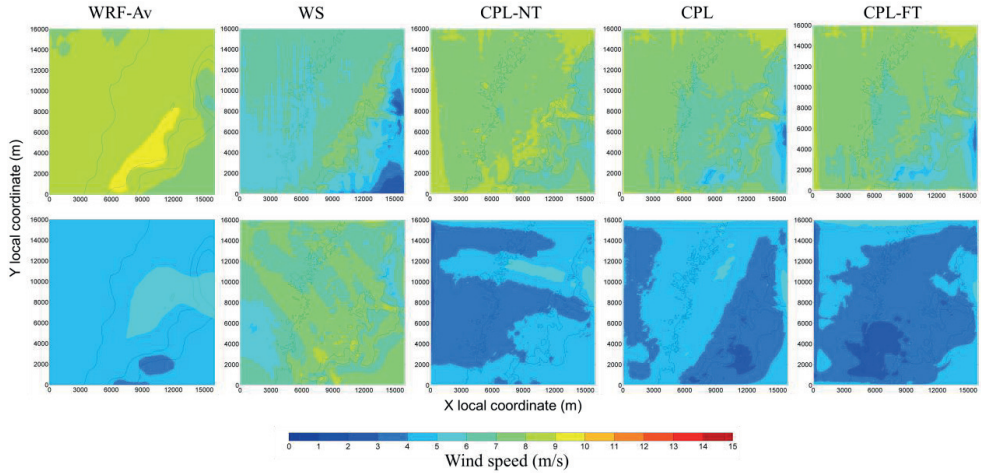


Figure 14. Horizontal planes of wind speed @ 100 m from sectors 0° (top panels) and 150° (bottom panels) at the PS site for the set-ups in Table 6. The black lines in the map correspond to the contour lines of terrain elevation for every 50 m.

4.3.1 Vertical extrapolation errors

Vertical crosscheck prediction errors are calculated to evaluate the vertical extrapolation of the models. These values provide a quantitative metric of the similarity between the measured and modelled vertical profiles. The validation results are presented in Figure 15. In addition to the crosscheck prediction errors, some of the vertical profiles of wind speed are shown in Figure 16.

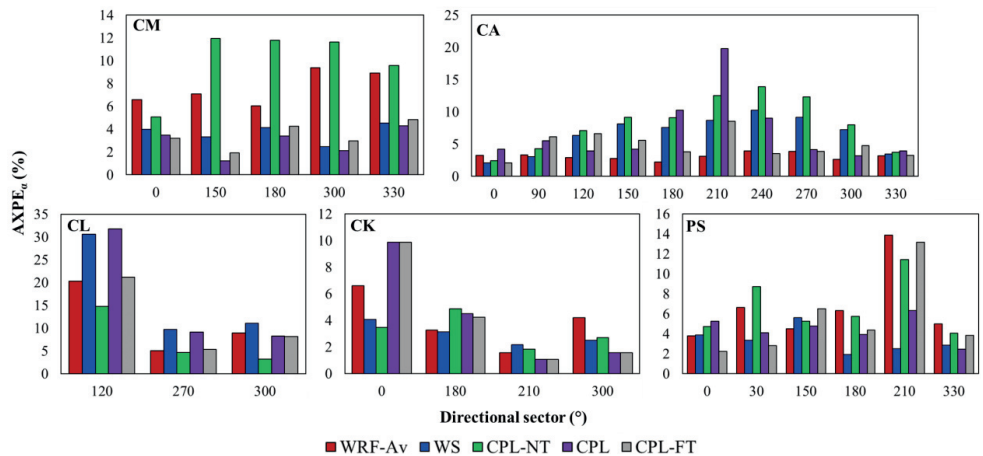


Figure 15. Vertical crossprediction errors of the main sectors at the studied sites. The name of the site is indicated in the top-left corner of each panel.

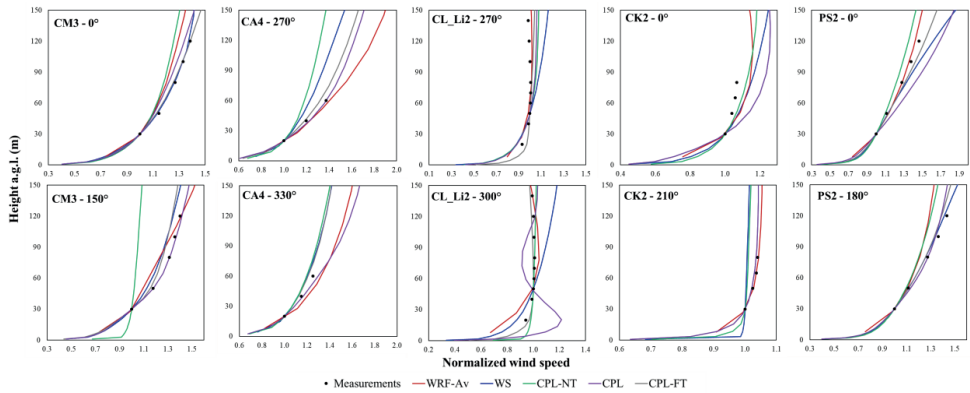


Figure 16. Measured and simulated vertical profiles of wind speed. The name of the measurement instrument and the wind direction sector are indicated at the upper-left corner of each panel.

For the CM site (complex terrain), the results that use the microscale model have the best performance, except for CPL-NT. As expected for neutral simulations, CPL-NT produces wind profiles with too low shear compared with the simulations which consider non-neutral conditions. This underlines that in order to better reproduce the wind shear under these conditions it is not sufficient to use a finer grid resolution but also to have proper atmospheric stability conditions in the model. The CPL and CPL-FT results perform even better than the WS model, thus suggesting that the inclusion of mesoscale forcing enhances the model. The CPL and CPL-FT model are even able to correct the incorrect shear from the WRF model (see CM in Figure 16).

CA (flat terrain) is the only site where the WRF-Av performs consistently better than the other models in terms of the vertical crosscheck prediction error. Depending on the atmospheric stability of the sector, the other models have slight error differences. The WRF-Av results reproduce well the shear at heights above 30 m. Nevertheless, below this height, the shear is overpredicted. It is expected that the WRF-Av result is worse at lower heights, where the influence of the terrain is higher. Similar as in CM, the wind profiles of the CPL-NT underpredicts the simulated shear, while the models that use the downscaled potential temperature (CPL) perform better. The CPL-FT result, which is in between CPL-NT and CPL in terms of atmospheric stability, is also in between those in terms of vertical extrapolation errors.

At CL, the CPL-NT vertical cross-prediction results are consistently better than the other modeling approaches. This site has a combination of unstable and stable atmospheric conditions because of a marked diurnal cycle. The coupled models that account for stability (CPL and CPL-FT) are slightly worse compared with the WRF-Av results. This indicates that the potential temperature fields in the microscale model might not be adequate due to the averaging of very different atmospheric conditions. The WS results are not capable of reproducing the wind speed vertical profiles for sectors where the shear does not follow an analytical shape. As shown in Figure 16, the measured profile in CL appears to have high shear below 20 m and then a constant speed up to 100 m. Above this height the wind has a negative shear. This kind of complex shapes are only possible to obtain with a mesoscale or a coupled model.

At CK the vertical cross prediction errors are relatively low for the most frequent sectors independent of the model. For the westerly directional sectors, the microscale models are performing slightly better than the mesoscale model. As discussed in subsection 4.2.1, this is probably a consequence of the explicit modeling of the terrain features around the river by the microscale model. The CPL and CPL-FT results have the worst performance for sector 0° , while the CPL-NT has the best of all models. This sector is the most frequent one which again implies that the averaging of varying atmospheric stability conditions yields an improper potential temperature field. It must be noted that the WS results do not have very realistic conditions towards the ground for some sectors, e.g. 210° (see CK in Figure 16). The reason is that the only way to produce a shear as low as the measured one is to use very unstable atmospheric stability values. This produces a low shear at higher heights, which is consistent with the measurements. Nevertheless, it produces unrealistic behavior towards the ground. This problem does not exist in coupled models as they are capable of using boundary conditions that have a low wind shear but with not so unstable atmospheric conditions.

For the south and southeast directional sectors the result using the microscale model and thermal effects (WS, CPL and CPL-FT) have the best performance at PS (like sector 180° in Figure 16). The site has a small ridge located at the southeast, in addition to stable atmospheric conditions. This indicates that the inclusion of atmospheric conditions is relevant to properly model the shear if the flow is perturbed by the terrain features. Furthermore, for directional sectors where the flow is not disturbed (like 0°) the difference among the models is rather small. For some sectors (e.g. 180° in Figure 16) the WRF-Av result underpredicts the shear

considerably. Despite that the coupled models are able to correct this shear, the WS simulations better reproduce it for heights higher than 100 m as the profiles follow an analytical shape.

5. Conclusions

A meso-microscale coupling model was validated using three different approaches regarding thermal effects: i) using neutral stratification (CPL-NT), ii) directly downscaling the averaged mesoscale temperature field (CPL) and iii) downscaling a filtered potential temperature field (CPL-FT). These different coupling approaches yield different wind flow patterns and wind speed profiles in spite of utilizing the same boundary conditions for wind speed. This highlights the importance of an appropriate transfer of temperature fields from the mesoscale to the microscale model when designing coupling strategies. Therefore, any future improvement of the discussed modeling approaches should focus on the downscaling of the potential temperature and to deliver a temperature field which is in balance with the wind field.

For wind resource assessment studies which want to use this new coupling framework, it is recommended to use a combination of the presented coupling set-ups. The choice of the set-up will depend on whether the focus is on horizontal or vertical extrapolations of the available measurements and on the complexity of the site with regards to orography and atmospheric stability conditions of the modelled sector. For vertical extrapolations the coupled simulations are in most cases better than the standalone (WS) or mesoscale simulations. For horizontal extrapolations at very flat and stable sites, it is better not to couple the potential temperature and run with neutral stratification instead (like CPL-NT). For more complex terrain, the use of atmospheric stability (like in CPL and CPL-FT) enhances the wind flow simulation for most cases. For sites with relatively simple terrain and strong thermal effects, the averaged WRF (WRF-Av) performs slightly better than the microscale models. Nevertheless, it has to be noted that the mesoscale model cannot model the effect of small terrain features like small valleys, rivers, ridges and small hills. This limits the extrapolation capabilities when using mesoscale models in practice. In this study there were no measurements sufficiently close to this type of geographical features and therefore the validation study might be biased towards “obstacle free” locations.

The weakness of the coupled model is clearly in sites where the average atmospheric stability is very stable and therefore the turbulence level is too low in the microscale model to maintain

a realistic wind flow pattern. Here the wind has a quasi-laminar behavior, while turbulence models like the $k - \varepsilon$ standard model are designed for turbulent flow. A possibility is to introduce some forcing terms in order to strengthen the mesoscale influence. This may include the nudging of the microscale simulations with the mesoscale field, in a similar way as it is done for nested WRF models.

The coupling procedure works well for sites where not too many different flow patterns and/or atmospheric stability conditions occur in the same wind direction sector. Therefore, sites with only few main wind directions can be challenging. Even at directional sectors with equal occurrence of stable and unstable conditions, the averaged temperature field will tend to have a stable stratification since it is more likely to have big positive values of $\Delta\theta$ than big negative ones. The filtering procedure introduced in this study partially deals with this problem, showing improved results in flat areas with marked stable conditions. A more robust solution would be to split the mesoscale fields according to wind direction and stability conditions. The authors of this study are currently investigating the use of machine learning techniques to obtain the relevant combinations of wind direction and atmospheric stability present at a site in an automated manner.

Acknowledgments

This research was supported by a grant from The Norwegian Research Council, project number 271080. The authors thank Mainstream Renewable Power and RWE Renewables Americas LLC for granting access to onsite measurements and mesoscale datasets. A special thanks to Romains Molins from Mainstream Renewable Power for his valuable effort in granting this study with datasets for four of the studied sites.

Appendix

A1 | Details about instruments to measure wind conditions

In Table A1, detailed information about the instruments utilized to measure the wind conditions at the studied sites is presented. For each site, the type of instrument, measured height and recorded period, is presented. Each instrument is named according to its site in order to facilitate their reference in the study. If the instrument corresponds to a LiDAR, the name

contains the characters “Li”. If it corresponds to a meteorological mast, no extra characters were added.

Table A1. Characteristic of the instruments used for monitoring at each validation site.

Site	Instrument name	Type of instrument	Measured Heights a.g.l. (m)	Recorded period (month/year)
CA	CA1	Meteorological mast	20, 40, 60	12/2015 – 05/2018
	CA2	Meteorological mast	20, 40, 60	11/2015 – 05/2018
	CA3	Meteorological mast	20, 60	04/2015 – 05/2018
	CA4	Meteorological mast	20, 40, 60	02/2016 – 04/2018
	CA5	Meteorological mast	20, 40, 60	02/2016 – 05/2018
	CA6	Meteorological mast	20, 40, 60	02/2016 – 05/2018
	CA_Li1	LiDAR	40, 50, 60, 70, 80, 91, 100, 110, 120, 130, 150, 180	04/2016 – 01/2017
CM	CM1	Meteorological mast	30, 50, 66, 80	04/2014 – 11/2019
	CM2	Meteorological mast	30, 50, 80, 100, 120	12/2017 – 11/2019
	CM3	Meteorological mast	30, 50, 80, 100, 120	10/2018 – 11/2019
CL	CL1	Meteorological mast	20, 30, 50, 65, 80	01/2014 – 03/2019
	CL_Li1	LiDAR	20, 40, 50, 60, 70, 80, 100, 120, 140, 180, 200	01/2015 – 09/2016
	CL_Li2	LiDAR	20, 40, 50, 60, 70, 80, 100, 120, 140, 180, 200	09/2016 – 10/2017
CK	CK1	Meteorological mast	10, 20, 30, 40, 50, 60	04/2010 – 10/2018
	CK2	Meteorological mast	30, 50, 65, 80	10/2011 – 10/2018
PS	PS1	Meteorological mast	40, 60, 80, 100	12/2014 – 11/2019
	PS2	Meteorological mast	30, 50, 80, 100, 120	11/2018 – 10/2019

References

1. Murthy KSR, Rahi OP. A comprehensive review of wind resource assessment. *Renew Sustain Energy Rev.* 2017;72(July):1320-1342. doi:10.1016/j.rser.2016.10.038
2. Hristov Y, Oxley G, Žagar M. Improvement of AEP Predictions Using Diurnal CFD Modelling with Site-Specific Stability Weightings Provided from Mesoscale Simulation. *J Phys Conf Ser.* 2014;524(Torque):012116. doi:10.1088/1742-6596/524/1/012116
3. Duraisamy VJ. Downscaling wind energy resource from mesoscale to local scale by nesting and data assimilation with a CFD model. PhD Thesis. 2014.
4. Monin AS, Obukhov AM. Basic laws of turbulent mixing in the surface layer of the atmosphere. *Contrib Geophys Inst Acad Sci USSR.* 1954;24(151):163-187.
5. Durán P, Meißner C, Rutledge K, Fonseca R, Martin-Torres J, Adaramola MS. Meso-

- microscale coupling for wind resource assessment using averaged atmospheric stability conditions. *Meteorol Zeitschrift*. 2019;28(4):273-291. doi:10.1127/metz/2019/0937
6. Sanz Rodrigo J, García B, Cabezón D, Lozano S, Martí I. Downscaling mesoscale simulations with CFD for high resolution regional wind mapping. In: *European Wind Energy Conference EWEC-2010*. Warsaw; 2010.
 7. Bilal M, Birkelund Y, Homola M, Virk M. Wind over complex terrain – Microscale modelling with two types of mesoscale winds at Nygårdstjell. *Renew Energy*. 2016;99:647-653. doi:10.1016/j.renene.2016.07.042
 8. Sanz Rodrigo J, Chávez Arroyo RA, Moriarty P, et al. Mesoscale to microscale wind farm flow modeling and evaluation. *Wiley Interdiscip Rev Energy Environ*. 2017;6(2). doi:10.1002/wene.214
 9. Duraisamy VJ, Dupont E, Carissimo B. Downscaling wind energy resource from mesoscale to microscale model and data assimilating field measurements. *J Phys Conf Ser*. 2014;555(555):012031. doi:10.1088/1742-6596/555/1/012031
 10. Skamarock WC, Klemp JB, Dudhi J, et al. A Description of the Advanced Research WRF Version 3. *Tech Rep*. 2008;(June):113. doi:10.5065/D6DZ069T
 11. Niu G-Y, Yang Z-L, Mitchell KE, et al. The community Noah land surface model with multiparameterization options (Noah-MP): 1. Model description and evaluation with local-scale measurements. *J Geophys Res*. 2011;116(D12):D12109. doi:10.1029/2010JD015139
 12. Mlawer EJ, Taubman SJ, Brown PD, Iacono MJ, Clough SA. Radiative transfer for inhomogeneous atmospheres: RRTM, a validated correlated-k model for the longwave. *J Geophys Res Atmos*. 1997;102(D14):16663-16682. doi:10.1029/97JD00237
 13. Hong S-Y, Jeong-Ock JL. The WRF single-moment 6-class microphysics scheme (WSM6). *J Korean Meteorol Soc*. 2006;42(2):129-151. http://www.mmm.ucar.edu/wrf/users/docs/WSM6-hong_and_lim_JKMS.pdf5Cnhttp://search.koreanstudies.net/journal/thesis_name.asp?pname=kiss2002&key=2525908.
 14. Kain JS. The Kain–Fritsch Convective Parameterization: An Update. *J Appl Meteorol*. 2004;43(1):170-181. doi:10.1175/1520-0450(2004)043<0170:TKCPAU>2.0.CO;2
 15. Nakanishi M, Niino H. An improved Mellor-Yamada Level-3 model with condensation

- physics: Its design and verification. *Boundary-Layer Meteorol.* 2004;112(1):1-31. doi:10.1023/B:BOUN.0000020164.04146.98
16. Gravdahl AR. Meso Scale Modeling with a Reynolds Averaged Navier - Stokes Solver Assessment of wind resources along the Norwegian coast. In: *31st IEA Experts Meeting State of the Art on Wind Resource Estimation*. Risø, Denmark; 1998:1-14.
 17. Meissner C, Gravdahl AR, Steensen B. Including Thermal Effects in CFD Wind Flow Simulations. *J Environ Sci Int.* 2009;18(8):833-839. doi:10.5322/JES.2009.18.8.833
 18. Launder BE, Spalding DB. The numerical computation of turbulent flows. *Comput Methods Appl Mech Eng.* 1974;3(2):269-289. doi:10.1016/0045-7825(74)90029-2
 19. Sanz C. A Note on $k - \epsilon$ Modelling of Vegetation Canopy Air-Flows. *Boundary-Layer Meteorol.* 2003;108(1):191-197. doi:10.1023/A:1023066012766
 20. Duynkerke PG, Driedonks AGM. A Model for the Turbulent Structure of the Stratocumulus-Topped Atmospheric Boundary Layer. *J Atmos Sci.* 1987;44(1):43-64. doi:10.1175/1520-0469(1987)044<0043:AMFTTS>2.0.CO;2
 21. Duynkerke PG. Application of the $E - \epsilon$ Turbulence Closure Model to the Neutral and Stable Atmospheric Boundary Layer. *J Atmos Sci.* 1988;45(5):865-880. doi:10.1175/1520-0469(1988)045<0865:AOTTCM>2.0.CO;2
 22. Farr TG, Rosen PA, Caro E, et al. The Shuttle Radar Topography Mission. *Rev Geophys.* 2007;45(2):RG2004. doi:10.1029/2005RG000183
 23. Canadian Digital Elevation Model. <https://open.canada.ca/data/en/dataset/7f245e4d-76c2-4caa-951a-45d1d2051333>. Accessed December 4, 2019.
 24. Jun C, Ban Y, Li S. Open access to Earth land-cover map. *Nature.* 2014;514(7523):434-434. doi:10.1038/514434c
 25. Wickham J, Homer C, Vogelmann J, et al. The Multi-Resolution Land Characteristics (MRLC) Consortium — 20 Years of Development and Integration of USA National Land Cover Data. *Remote Sens.* 2014;6(8):7424-7441. doi:10.3390/rs6087424
 26. Bachant P, Wosnik M. Effects of Reynolds Number on the Energy Conversion and Near-Wake Dynamics of a High Solidity Vertical-Axis Cross-Flow Turbine. *Energies.* 2016;9(2):73. doi:10.3390/en9020073
 27. Berg J, Mann J, Bechmann A, Courtney MS, Jørgensen HE. The Bolund Experiment, Part I: Flow Over a Steep, Three-Dimensional Hill. *Boundary-Layer Meteorol.*

- 2011;141(2):219-243. doi:10.1007/s10546-011-9636-y
28. Han J, Arya SP, Shen S, Lin Y-L. *An Estimation and Energy Atmospheric Theory of Turbulent Dissipation Boundary Kinetic Energy Rate Based on Layer Similarity*. NASA Technical Report. Hampton, Virginia; 2000.
 29. Stull RB. *An Introduction to Boundary Layer Meteorology*. (Stull RB, ed.). Dordrecht: Springer Netherlands; 1988. doi:10.1007/978-94-009-3027-8
 30. Arya SP. *Introduction to Micrometeorology*. 2nd ed. San Diego: Academic Press; 1998.
 31. Berkowicz R, Prahm LP. Evaluation of the profile method for estimation of surface fluxes of momentum and heat. *Atmos Environ*. 1982;16(12):2809-2819. doi:10.1016/0004-6981(82)90032-4
 32. Veiga Rodrigues C, Palma JMLM, Rodrigues ÁH. Atmospheric Flow over a Mountainous Region by a One-Way Coupled Approach Based on Reynolds-Averaged Turbulence Modelling. *Boundary-Layer Meteorol*. 2016;159(2):407-437. doi:10.1007/s10546-015-0116-7
 33. Storm B, Dudhia J, Basu S, Swift A, Giammanco I. Evaluation of the weather research and forecasting model on forecasting low-level jets: Implications for wind energy. *Wind Energy*. 2009;12(1):81-90. doi:10.1002/we.288
 34. Nunalee CG, Basu S. Mesoscale modeling of coastal low-level jets: implications for offshore wind resource estimation. *Wind Energy*. 2014;17(8):1199-1216. doi:10.1002/we.1628

Paper IV

Wind resource assessment using a novel meso-microscale coupling framework based on two-level self-organized maps clustering: A preliminary study

Pablo Durán^{a, b, *}

^a Norwegian University of Life Sciences, Universitetstunet 3, Ås, Norway

^b WindSim AS, Fjordgaten 13B, Tønsberg, Norway

* E-mail address: paduran@nmbu.no

Abstract

Utilizing a fully automated classification approach, predominant weather patterns are extracted from a simulated mesoscale data. The dependence of these patterns on atmospheric stability, wind speed and wind direction are studied. It is shown that the probability distributions of these patterns depend on seasons as well as on diurnal cycles. The patterns are downscaled using a steady-state computational fluid dynamic model. The simulated wind speeds of the mesoscale and downscaled patterns are validated against onsite measurements. The future potential of the proposed approach in wind resource assessment and in particular for wake modelling, is discussed in this paper

Keywords: RANS, WRF, CFD, Diurnal cycle, Mesoscale models, clustering.

1. Introduction

Current evaluation of wind energy projects heavily relies on the use of steady-state wind flow models to estimate the energy production. An assumption widely made in the wind energy industry when utilizing these models is that the ratio of the horizontal wind speed between two points is the same for a given wind direction, independent of the wind speed scale. This ratio, referred hereafter to as speed-up (SU), is typically utilized to extrapolate wind speeds from a reference point u_R (usually measurements) to a target point u_T (usually wind turbines) using $SU = \frac{u_T}{u_R}$. The assumption that SU values are only dependent on the wind direction allows to lower the use of computational resources without losing significant performance. As shown in the example of Figure 1, this is a reasonable assumption for relatively high wind speeds. Nevertheless, at lower wind speeds (but still well above 3 m/s), this assumption does not always hold true. Furthermore, at lower these speeds there is non-linear dependence between the observed SU values and the observed atmospheric stability, as shown in the example of Figure 1.

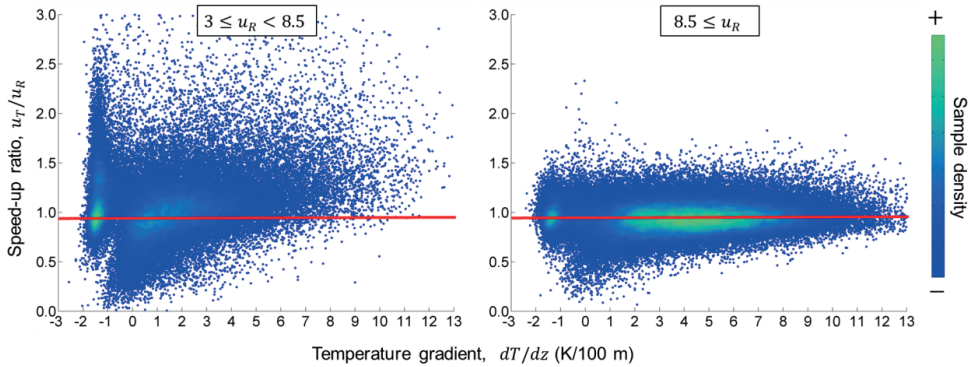


Figure 1. Example of measured speed-up ratios for the directional sector 0° . The considered values of u_R (m/s) are indicated at the top of each panel. The red line indicates a $SU = 0.95$.

At best, a steady-state model would calculate for the example in Figure 1, a SU value of ~ 0.95 . Such a value would be wrong at low wind speeds if important thermal effects occur at the site. A possible approach to deal with this limitation is to simulate different atmospheric stability conditions per wind direction. Even assuming the minimum possible number of atmospheric stability classes (unstable, neutral and stable), the total number of simulations would triple. Furthermore, some combinations of wind direction and stability will probably have very low or no occurrence at the modelled site, wasting computational resources. Another option to obtain SU values that vary with u_R is to use a transient model instead of a steady-state one, avoiding the assumption of wind speed independent SU values at all. Nevertheless, this type of computational fluid dynamic (CFD) models are computationally expensive for most of the industry.

In this work, we propose a meso-microscale coupling approach that obtains one SU value per predominant wind condition (wind speed, wind veer, wind shear and atmospheric stability) at the site. The most predominant site-specific patterns are extracted in an automated manner from mesoscale simulations using the same methodology as in Durán et al. (2019).¹ The patterns are then downscaled utilizing a steady-state CFD model. Details about the classification methodology and the data treatment are explained in Section 2. The obtained wind conditions are transferred to the microscale model as boundary conditions of the steady-state CFD model. Further details of this transferring as well as of the datasets used to model and validate the simulations are presented in Section 3. In Section 4, we present the obtained patterns and their downscaling. Further discussion and conclusions of this exercise are presented in Section 5.

2. Studied site and data sets

The validation study is carried out using a site hereafter referred to as CK. This site belongs to a commercial wind energy generation project and therefore information regarding the real name, exact location and absolute wind speeds are not disclosed. The site is located in the Southern Cone of South America in a desert area. The wind conditions at the site are strongly influenced by the diurnal cycle, with unstable atmospheric conditions during the daytime and stable atmospheric conditions during the dawn-morning time. Three type of datasets are used in this study: i) terrain data, ii) onsite measurements and iii) mesoscale simulations. A summary of the terrain and onsite measurement data is presented in Figure 2. Further details of the datasets of the site are presented in the following subsections.

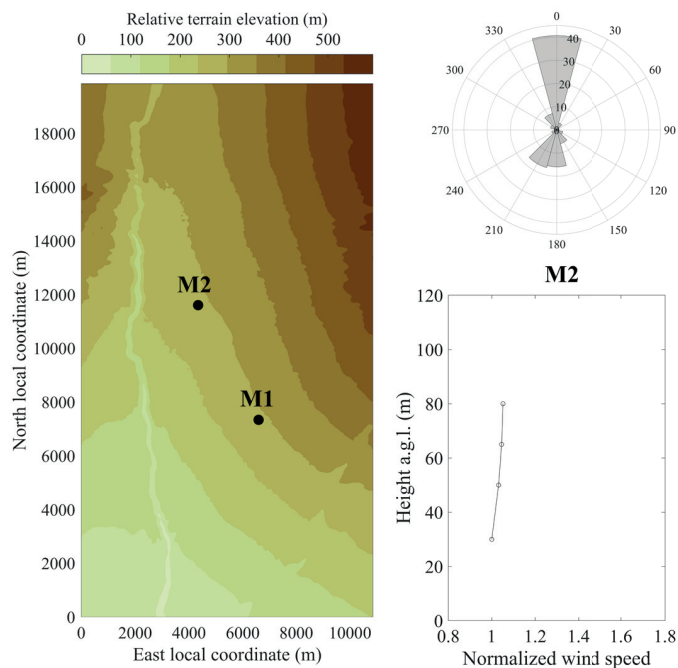


Figure 2. Left-panel: terrain elevation map of the CK site. The location of the measurement points is indicated by black circles with their names above. Right panels: wind rose (top) and vertical profile of wind speed (bottom). The instrument used to compute them is indicated above the bottom-right panel.

2.1. Terrain data

The terrain data consist of the map of terrain elevation. This was constructed using the Shuttle Radar Topography Mission (SRTM) database.² This database also contains land cover data. Nevertheless, it was found that it has poor coverage for the studied area and therefore a constant roughness length = 0.01 m was used instead. The site is relatively flat and with a positive inclination northward (Figure 2). A riven is located at the west part of the site that traverses from south to north.

2.2. Wind measurement data

Wind conditions at the site were monitored through anemometers mounted in 2 meteorological masts and 3 Light Detection and Ranging (LiDAR) systems. Ten-minute averages of horizontal wind speed and wind direction at several heights are available. The measured heights and recorded periods at each of the measurement points are presented in Table 1. The location of each measurement is shown in Figure 2. As shown in the same figure, the wind at the site has on average a very low shear and most of the wind comes from the north. The two meteorological mast have more than 7 years of coverage, while the LiDARs have only coverage for 3 to 5 months.

Table 1. Details of the onsite measurements at CK.

Instrument name	Type of instrument	Measured Heights a.g.l. (m)	Recorded period (month/year)
M1	Meteorological mast	10, 20, 30, 40, 50, 60	04/2010 – 10/2018
M2	Meteorological mast	30, 50, 65, 80	10/2011 – 10/2018

2.3. Mesoscale simulations

One-year worth of mesoscale simulations is produced using the Weather research and Forecasting (WRF) model. The simulation covers from October 2013 to October 2014. This timespan was selected in order to cover the longest concurrent measured year among all measurements at the site (see Table 1). The configuration of the WRF model, including physics parameterizations and grid settings are the same as the ones used by Durán et al. (2020).³ The innermost domain has a resolution of 1 km and it was configured to cover the whole microscale domain. Mesoscale outputs are stored every 1 hr and therefore a total of 8760 timesteps are available.

3. Methodologies

In this work, an automated classification methodology is utilized to extract the dominant patterns from a mesoscale simulation. The obtained mesoscale fields are then used to compute the boundary conditions of a steady-state microscale model. Details of the microscale model, the classification methodology and the procedure to compute the boundary conditions are provided in the following subsections.

3.1. Microscale steady-state CFD model

The CFD software WindSim is used to simulate the microscale wind flow. WindSim's governing equations are based on the steady-state version of the Reynolds-averaged Navier-Stokes (RANS) equations, using the standard $k-\varepsilon$ turbulence closure scheme.⁴ For more details about the actual formulation of the governing equations in WindSim, the reader is referred to the work of Gravdahl (1998).⁵ For non-neutral atmospheric conditions, a temperature equation is introduced and extra terms are added to the momentum and turbulence equations as detailed by Meissner et al (2009).⁶

The digital terrain model of CK consists of a rectangular grid of 11 x 20 km. A refinement area of 5.3 x 13.6 km concentric with the domain area is used, with a horizontal resolution of 40 m. From the boundaries of the refinement area towards the boundary of the domain, the horizontal resolution is gradually reduced up to 170 m. A total of 60 vertical levels is used, spanning up to 4000 m a.g.l. The vertical resolution is the higher towards the ground and gradually reduces upwards. At least 9 vertical levels are located within the first 100 m.

3.2. Automated classification of simulated mesoscale fields

For the classification of the mesoscale fields, only the grid points located within the microscale domain are used. A total of $11 \times 21 \times 19 = 4389$ grid points are considered for the classification. The considered variables are the wind velocity vector in the east direction U_x and in the north direction U_y , as well as the gradient of potential temperature $\Delta\theta = \theta - \theta_0$. Here, θ and θ_0 are the potential temperatures at all heights and at the lowest vertical level of the WRF model,

respectively. U_x and U_y fields contain information about the wind direction, wind veer and wind shear, while $\Delta\theta$ contains information about the atmospheric stability. Therefore, the input data for the classification consist of 8760 samples, each corresponding to a vector length =12936 (=2 x (11 x 21 x 19) + 11 x 21 x 18).

The mesoscale simulation is clustered using a two-level self-organizing map clustering (SOM2L) approach.⁷ SOM2L allows for a fully automated clustering of the data without the need to prescribe the number of clusters a priori, making it more advantageous than other popular clustering techniques like k -means. The first level or stage of the SOM2L corresponds to the training of a self-organizing map (SOM) with the input data.⁸ The SOM consists of interconnected neurons (or nodes) in a 2-D grid array that are iteratively adapted according to the input data. After the training, the SOM provides a visualization of the clustering structures by plotting the distances between the nodes. The second level of the algorithm exploits this feature to determine the number of clusters within the data.⁹ Further technical details of the SOM2L are presented in the following subsections. The configuration of the SOM2L is discussed in the work of Durán et al. (2019)¹ and the references therein. Compared to that study, some of the training parameters were modified and an intermediate step between the two levels was added.

SOM2L level 1 – SOM training

The mesoscale data is filtered by removing the timesteps in which the average wind speed of the nodes between 50 and 150 m is lower than 3 m/s. This way, only timesteps that are of interest for wind energy generation are considered in the classification. It should be noted that depending on the application, this filtering might be omitted. A 25 x 25 SOM with hexagonal grid cells is used, giving a total of 625 nodes. This is much higher than the value given by the rule of thumb proposed by Vesanto et al. (2000),¹⁰ which suggests the use of approximately 468 nodes for a sample size of 8760. This rule of thumb works as a lower limit since the SOM should have as many nodes as possible when used for clustering purposes, as commented by Kohonen (2013).¹¹ The SOM is initialized using linear initialization⁸ and then trained by using the batch algorithm⁸ in two training phases. The first phase uses a neighborhood radius =25 that linearly decreases to 1 in 200 iterations. The second phase uses a radius =1 for another 200 iterations.

SOM2L level 2 – SOM clustering

The method to partition the SOM is based on the distances between the nodes (Figure 3a). These distances are roughly inversely proportional to the probability density function of the input data.⁹ Therefore, it is expected that the local minima of the distances correspond to the cluster centers of the data. A potential problem with this approach is that the distances could have some local minima which are a product of random variations in the data, rather than actual local minima.⁹ For this reason we apply a fully automated smoothing procedure proposed by Garcia (2010)¹² before computing the local minima (Figure 3b). After the smoothing, initial clusters are defined as the nodes corresponding to the local minima. Then, neighboring nodes of these initial clusters are assigned to a cluster based on Ward's criteria (Figure 3c).¹³

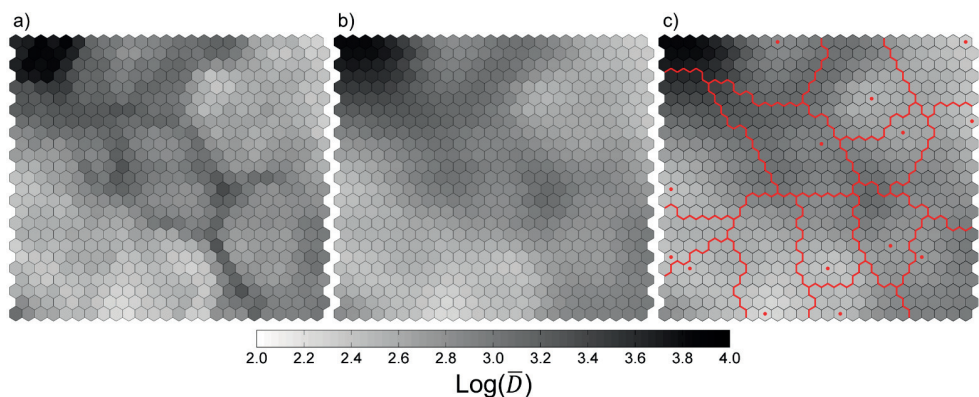


Figure 3. a) Distance map of the trained SOM applied to the CK mesoscale data, b) distance map after the smoothing and c) partition of the SOM based on the local minima of \bar{D} . In c) the local minima are indicated by the red dots and the partitions by the red lines. \bar{D} corresponds to the average distance between a node and its neighbors.

3.3. Coupled boundary conditions

The wind conditions contained in the mesoscale fields extracted by the SOM2L are transferred to the microscale model as initial and boundary conditions. In essence, the wind and potential temperature fields are interpolated into the microscale domain. For microscale points below the lowest vertical level of the mesoscale model, the values are extrapolated using the Monin-Obukhov similarity equations. The turbulent kinetic energy and its energy dissipation are prescribed in the microscale model using the formulation derived by Han et al. (2000).¹⁴ For

further details of the transferring procedure, the reader is referred to the work of Durán et al. (2019).¹⁵

3.4. Crosscheck prediction error

Steady-state wind flow models are used in wind resource assessments to extrapolate observational data to potential locations of wind turbines. This extrapolation is conducted by multiplying the measured wind speeds at the observational point by a factor, the so-called speed-up ratio (SU). The SU is predicted by the model and is calculated as:

$$SU(R, T) = \frac{u_T}{u_R} \quad (1)$$

Here, u_R and u_T correspond to the simulated wind speed at a reference (R) and a target (T) location, respectively. When conducting wind energy estimations, R corresponds to a measurement point and T to a potential wind turbine location. The common practice is to obtain one $SU(R, T)$ value per simulated wind direction. However, in this study different mesoscale patterns are downscaled using the microscale model, instead of simulating different wind directions. These patterns have an associated wind direction, but some of them might have the same one. For this reason, speed-up ratios are obtained per extracted pattern SU_p , where the subscript p indicates the pattern number. Infrequent directions will not be found in the extracted patterns.

Typically in wind resource assessment, 12 or more wind directions are simulated. Each of these 12 wind fields are validated by using measurements that have a similar wind direction. Since this study uses patterns instead, there is no trivial way to determine which downscaled pattern should be used for each timestep. The proposal in this study is to select the downscaled pattern p^* for each timestep as:

$$p^* = \arg \min_{p \in P} \left(\sum_{c \in C} |U_{xp}(c) - U_{xm}(c)| + |U_{yp}(c) - U_{ym}(c)| \right) \quad (2)$$

Here, $U_x(c)$ and $U_y(c)$ correspond to the north and east components of the wind at the observational point c , respectively. The subscript p indicates that the values are taken from the downscaled results of that pattern, while m indicates that the values correspond to the measurement for that timestep. The set P consists of all patterns and the set C consists of the

considered observational points. In this study, five observational points are considered for the procedure: M1 @ 50 and 60 m, and M2 @ 50, 65 and 80 m. XPE is then calculated for each pattern as:

$$XPE_p(R, T) = \frac{\overline{SU_p(R, T)} \times \overline{u_{Rp}} - \overline{u_{Tp}}}{\overline{u_{Tp}}} \quad (3)$$

In this case, R and T correspond to a reference and a target measurement, respectively. One value of $XPE_p(R, T)$ is obtained per pair of measurements and per pattern. In order to facilitate the analysis of the XPE values, their absolute values are averaged per pattern, obtaining the absolute cross-check prediction errors:

$$AXPE_p = \frac{\sum_{R, T \in M; R \neq T} |XPE_p(R, T)|}{N_M} \quad (4)$$

Here M is the set of the observational points considered for the error calculation and N_M is the total number of pair of observational points in M .

4. Results

In this section, two types of results are discussed. First, the extracted mesoscale fields obtained by the SOM2L are presented and characterized. Secondly, the downscaled patterns are validated against onsite measurements.

4.1. Application of SOM2L in 3-D mesoscale timeseries

This subsection illustrates the capabilities of the SOM2L method to facilitate the identification and understanding of the prevalent wind conditions at a site. The SOM2L is applied to the 3-D mesoscale fields generated with WRF for the CK site. One important advantage of using a SOM in the classification procedure is that it provides spatial ordering of the underlying input data. This means that areas that are adjacent to one another in the map share certain characteristics (in this case wind speed, wind shear, wind direction, wind veer and/or $\Delta\theta$), which also applies to the obtained clusters. This feature of the SOM facilitates the characterization of the obtained cluster as well as their relation (Figure 4). It has to be underlined that the ordering is obtained from a fully automated procedure.

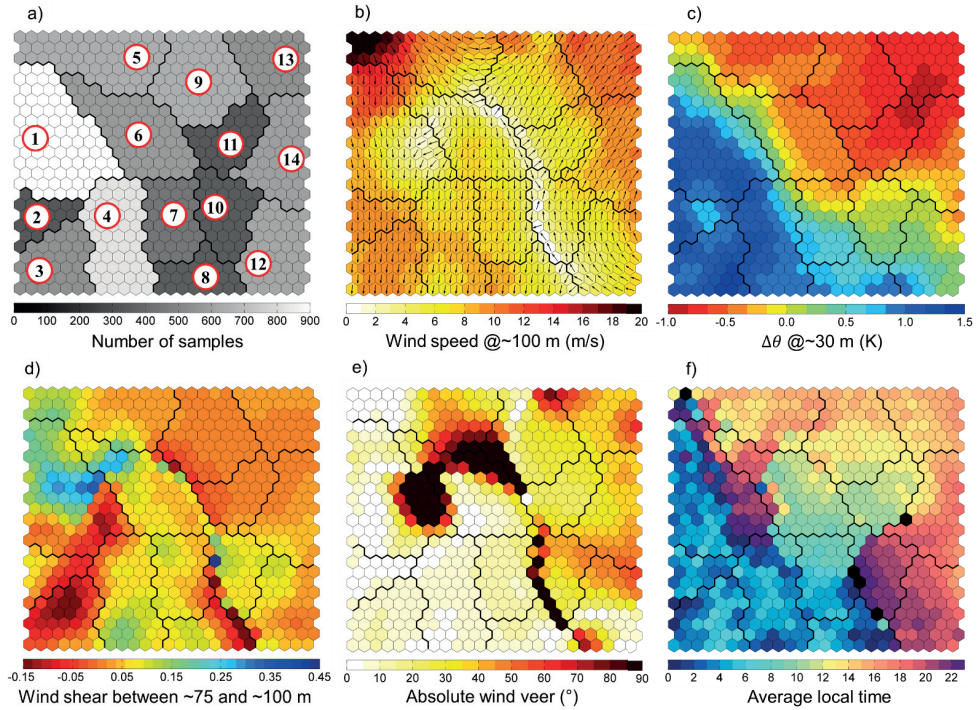


Figure 4. a) Frequency distribution of the partition, b) wind speed, c) $\Delta\theta$, d) wind shear, e) absolute wind veer and f) local time of the nodes of the SOM. In a), the cluster number is indicated. In panels b), c) and d) the coloring corresponds to the representative values of each node in the middle of the microscale domain. The black arrows in panel b) correspond to the wind directions. In a) and c) the values were extracted at the middle of the microscale domain. The bold lines in the panels indicate the boundaries between the clusters. In panel e) the values correspond to the average of the samples associated with the node. In f), nodes with no data are colored in black.

A total of 14 patterns are obtained by the SOM2L at the CK site. In Table 2, some characteristics of these patterns are presented. Using the maps of Figure 4, four types of patterns can be characterized depending on their location in the SOM: 1) patterns at the left and bottom-center parts correspond to northern winds occurring under stable atmospheric conditions ($\Delta\theta > 0$) and between 00:00 and 06:00 LST; 2) patterns located at the center also correspond to northern winds, but with neutral to slightly unstable atmospheric conditions between 06:00 and 12:00 LST; 3) patterns located at the top-center and top-left have unstable atmospheric conditions and low shear with southwestern wind direction, occurring between 12:00 and 18:00 LST; 4) patterns at the left and bottom-left parts correspond to relatively weak southeastern and southern winds with neutral stratification and between 18:00 and 00:00 LST. As expected, stable atmospheric conditions are predominant during nighttime, while unstable atmospheric conditions are predominant during daytime. Combining the information provided

in Figures 4 and 5, it can be inferred that during summer the winds are the weakest and they come mostly from north or southwest directions. During winter, winds are the strongest and they come mostly from north and northeast directions.

Table 2. Characteristics of the wind patterns obtained by the SOM2L.

#	Wind direction @ 100 m (°)		Wind speed @ ~100 m (m/s)		Frequency
	Min	Max	Min	Max	
1	348	16	3.9	9.0	12.1 %
2	352	8	3.8	9.5	4.3 %
3	354	14	3.9	10.5	7.0 %
4	358	17	2.3	8.2	10.6 %
5	293	325	8.5	11.6	8.3 %
6	330	2	2.1	6.5	7.5 %
7	350	12	2.9	7.8	5.7 %
8	356	12	2.8	7.6	4.5 %
9	200	229	4.3	7.5	8.4 %
10	168	214	3.9	7.3	4.5 %
11	182	219	5.3	7.1	4.3 %
12	149	192	3.9	6.7	8.0 %
13	184	234	8.8	11.1	7.0 %
14	182	230	8.6	10.1	7.7 %

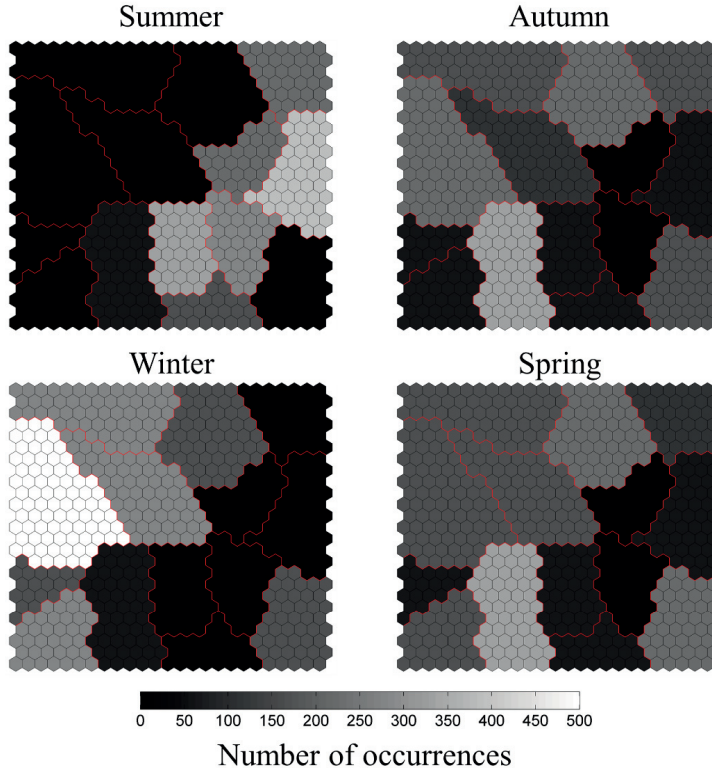


Figure 5. Frequency distribution of the patterns obtained by the SOM2L for summer (top-left panel), autumn (top-right panel), winter (bottom-left panel) and spring (bottom-right panel) seasons.

The horizontal planes of wind speed of the patterns (Figure 6) are very different from one another. However, some of them share certain features in the spatial distribution of the wind speed. For example, patterns 3, 4, 7 and 8 have an area located at the southeast part of the site with high wind speeds. In addition, the patterns 9, 13 and 14 have a similar spatial distribution of the wind veer within the site.

There is also high variability in the vertical planes of wind speed presented in Figure 7. Some of them correspond to high shear (patterns 1 and 5), low shear (patterns 6 and 10) or to a low-level jet (LLJ). The patterns corresponding to LLJs have different jet speed, ranging between weak (patterns 7, 8, 11 and 12), mild (patterns 2, 3 and 4) and strong (patterns 13 and 14). In the case of the vertical patterns of $\Delta\theta$, there is less variability. Three types are here identified

with different atmospheric stratification: unstable (patterns 11 and 13), slightly unstable (patterns 5, 9 and 14), neutral (patterns 6, 10 and 12) and stable (remainder of the patterns).

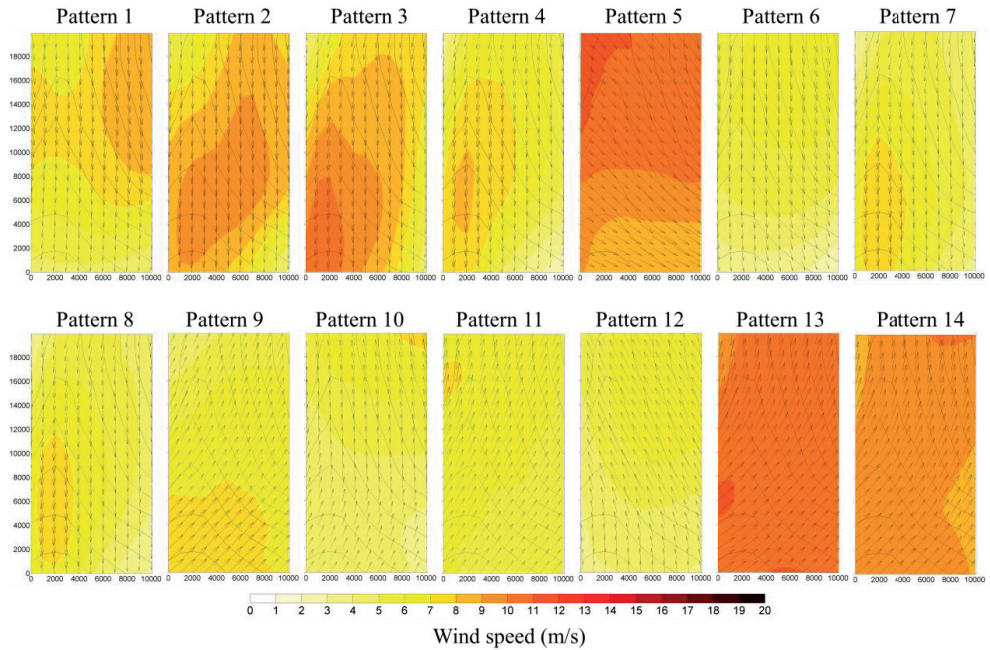


Figure 6. Horizontal planes of wind speed @ ~100 m of the patterns obtained by the SOM2L. The horizontal and vertical axes correspond to the east and north local coordinates, respectively. The wind direction is indicated by the black arrows.

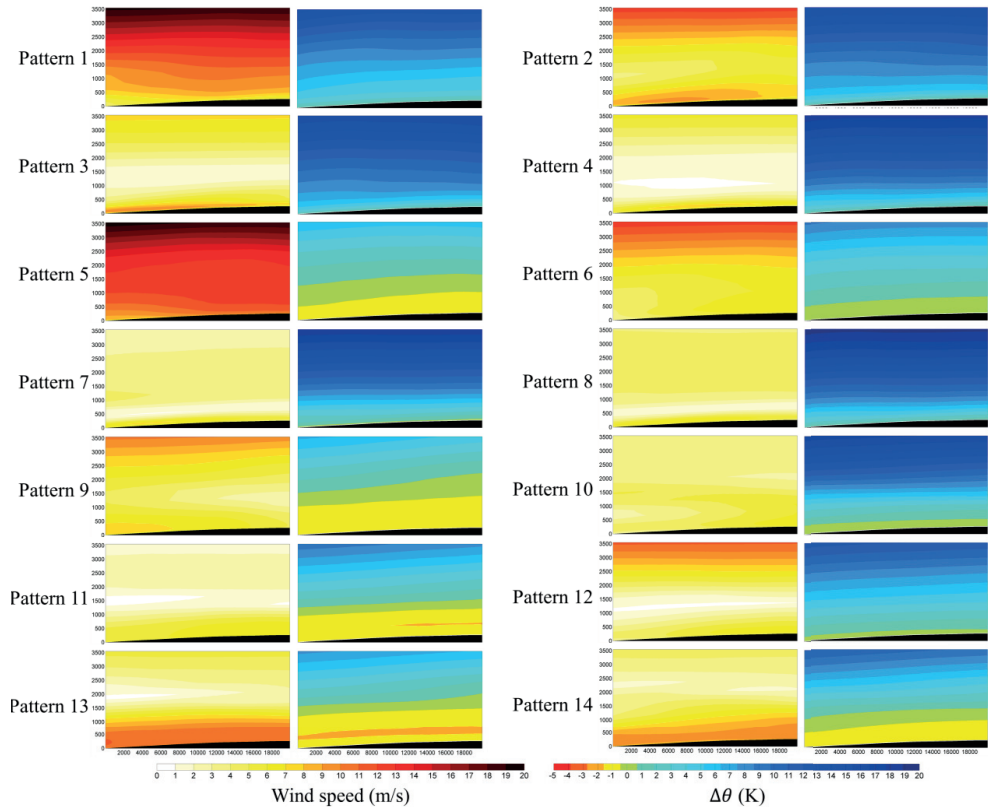


Figure 7. Vertical planes of wind speed (first and third columns) and $\Delta\theta$ (second and fourth columns) of the patterns obtained by the SOM2L. The vertical planes are located at the middle of the domain, spanning from south to north. The horizontal and vertical axes correspond to the north local coordinate (m) and the relative height ASL (m), respectively.

4.2. Downscaling of mesoscale fields

In this section the patterns obtained in Section 4.1 are downscaled using the microscale steady-state CFD model presented in Section 3.1. In Figure 8, the horizontal wind speed maps for the downscaled patterns are presented. When compared to Figure 7, it is clear that most patterns are significantly modified by the microscale model. Patterns with relatively high wind speeds and southwest winds (patterns 13 and 14) are influenced by the river located at the western part of the site. The effect of this terrain feature appears to be similar for both patterns. The river also has an important effect on patterns with north winds and stable atmospheric conditions. For example, in patterns 1, 2 and 3, the mesoscale influence is somewhat preserved, but the wind field has a considerable change where the river is located. For patterns 4, 7 and 8, there

is an area with relatively high wind speeds located at the southwestern part of the domain in the mesoscale model (Figure 7). These high wind speeds are not present in the microscale model. It is likely that this modification is caused by the lower wind speeds at the inlets of the model, and therefore the microscale model is not able to enforce this pattern. A similar effect is observed for patterns 5, 9 and 11, where the wind conditions at the inlet are carried downstream all the way to the outlet. This also modifies the direction of the wind close to the outlets of the model. For these three patterns the effect might be the product of high wind speeds and enhanced mixing due to unstable atmospheric conditions. In the case of patterns with south winds and neutral stratification (patterns 10 and 12) the wind field is just slightly modified.

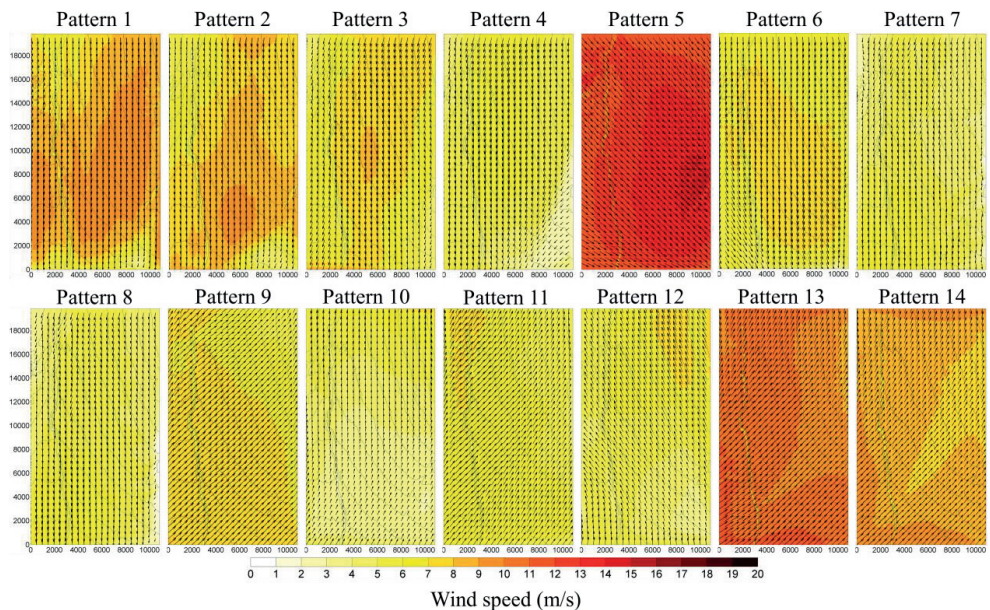


Figure 8. Horizontal planes of wind speed @ 100 m of the downscaled patterns obtained by the SOM2L. The horizontal and vertical axes correspond to the east and north local coordinates, respectively. The wind direction is indicated by the black arrows.

The mesoscale and microscale simulations are compared by means of the *AXPE* values (see Section 3.4 for further details). The horizontal extrapolation errors were calculated using the measured wind speed at M1 @ 60 m and M2 @ 80 m. For most patterns with north winds and stable atmospheric conditions (patterns 1, 2, 4 and 8), the microscale model reduces the error

significantly, ranging from 4 to 15 % in error reduction (Figure 9). Pattern 3 also has these characteristics, but nevertheless, the performance of the microscale model is the lowest for this pattern. This is probably due to the fact that pattern 3 is also the most stably stratified among all patterns. It has been shown that steady-state RANS models do not perform well when downscaling very stable mesoscale fields.³ For most patterns with unstable atmospheric conditions (patterns 5, 9, 11 and 13) the performance of the microscale simulation is inferior to the mesoscale, with an increase in error between 3 to 7 %. A similar trend is observed for the neutral simulations, where the most stably stratified pattern (12) has a reduction in error of 2% and the most unstably stratified patterns (6 and 10) have an increase in error of 7% and 4%, respectively, after downscaling. Overall, the error is reduced by 2.7% when using the downscaling procedure, and the patterns where the microscale model is as good or better than the mesoscale simulation correspond to about 70% of the measured time period.

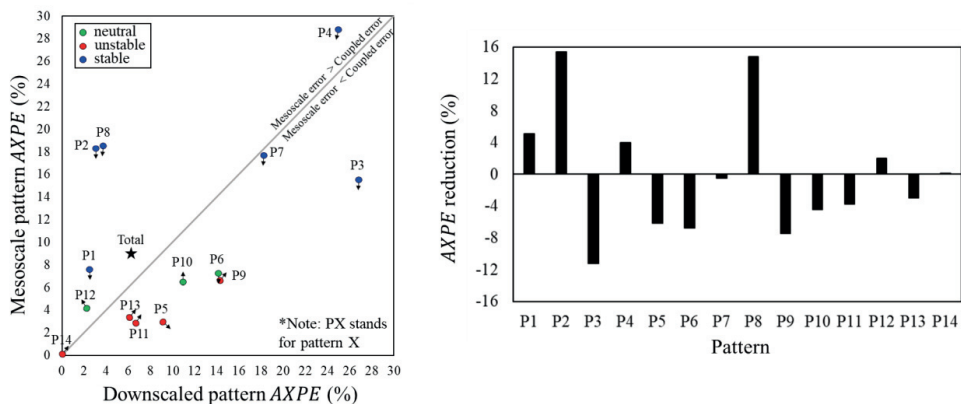


Figure 9. Left panel: Comparison of the crosscheck prediction errors between the mesoscale and downscaled patterns. The arrow and color of each circle indicate the wind direction and the atmospheric stability condition of the pattern, respectively. Right panel: Reduction in crosscheck prediction error after downscaling the patterns.

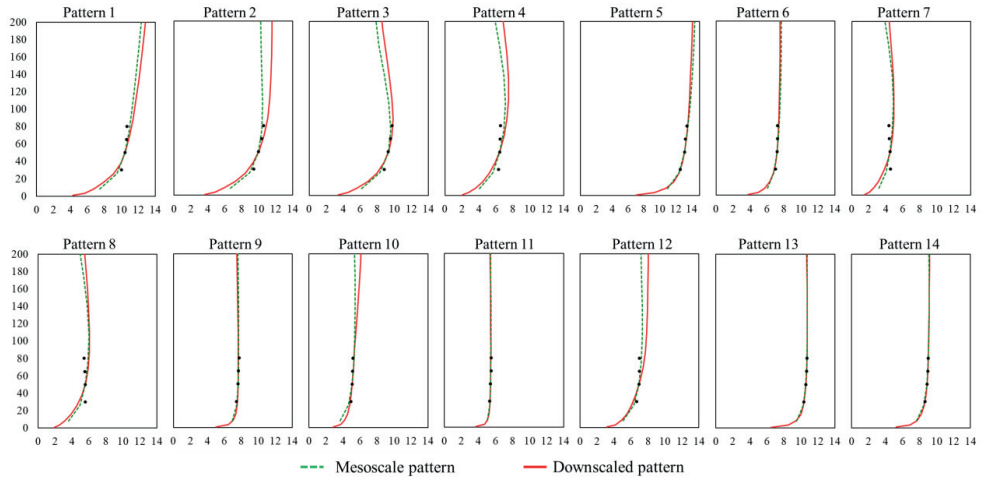


Figure 10. Measured and simulated vertical profiles of wind speed at the location of M2. The horizontal and vertical axes correspond to the wind speed (m/s) and height a.g.l. (m), respectively.

The measured and simulated vertical profiles of wind speed at metmast M2 are presented in Figure 10. The results obtained for the metmast M1 are identical and therefore not presented here for brevity. Overall, the mesoscale and microscale simulations present very similar profiles. For about half of the patterns, the simulations present slight differences in favor of the mesoscale model. Nevertheless, this improvement is minimal, as both simulations reproduce the measured wind shear well. For patterns with unstable atmospheric conditions (patterns 5, 9, 11, 13 and 14), the models perform particularly well. It must be noted that if analytical boundary conditions are used to force the microscale model, the only way to reproduce the very low wind shear observed for these patterns is to use small (negative) values of Monin-Obukhov length.

Patterns 4, 7 and 8 present a weak low-level jet, in addition to north winds and stable stratification. For these patterns, both models are unable to reproduce the observed negative shear. It appears that the reason for this deviation is that the WRF model is not able to properly reproduce the height of the jet for these patterns. This information is transferred into the microscale, which is unable to correct it. The opposite is true for pattern 3, where both models are able to properly capture the shape of the jet.

5. Conclusions

The SOM2L classification methodology utilized in this study is able to extract the dominant mesoscale patterns in an objective manner. The application of the methodology to a 3-D mesoscale dataset extracts a variety of wind conditions without requiring any a priori information about the number of different conditions at the site. Furthermore, with little effort the methodology can be used to analyze how the extracted patterns evolve with respect to time and how they are associated with different phenomena, wind direction or atmospheric stability. The methodology is very promising for sites where the wind has few predominant directions. As it very difficult to separate by weather conditions just by utilizing the measured wind conditions at a few observational points, these sites can be very challenging to model. Given a proper downscaling, the SOM2L is a promising approach for these sites.

Overall, the meso-microscale coupling methodology improves the wind estimations compared with the use of the raw fields. The improvement consists not only of a reduction of extrapolation errors, but also of the inclusion of finer features in the wind flow due to the higher resolution utilized in the microscale model. Nevertheless, the microscale model is not able to properly downscale some of the obtained wind conditions. The reason is that the microscale model is only able to provide information from the inlets into the domain. As a consequence, for example, areas with high wind speed within the domain are not maintained (e.g. pattern 4). Another example is that very high wind speeds at the inlets is propagated downstream, drastically modifying the spatial distribution of the wind speed provided by the mesoscale model (e.g. pattern 5).

Assuming that there is a robust way to downscale the mesoscale patterns, the proposed meso-microscale coupling methodology is very promising for the simulation of wake effects in wind farms. In order to resolve the wake in a steady-state CFD model (with an actuator disk for example), different wind speeds for the same wind direction must be simulated. This multiplies the number required of simulations, and by even more if different atmospheric stability classes must be taken into account. By using the SOM2L, infrequent combinations of wind speed and stability can be skipped, as the conditions derived from the mesoscale data are used instead. This is particularly relevant for offshore wind farms.

Acknowledgments

This research was supported by a grant from The Norwegian Research Council, project number 271080. The author thanks to Mainstream Renewable Power granting access to onsite measurements and mesoscale datasets. A special thanks to Sukanta Basu from the Faculty of Civil Engineering and Geosciences of the Technical University of Delft for his helpful feedback on earlier manuscript drafts.

References

1. Durán P, Basu S, Meißner C, Adaramola MS. Automated classification of simulated wind field patterns from multiphysics ensemble forecasts. *Wind Energy*. January 2020;we.2462. doi:10.1002/we.2462
2. Farr TG, Rosen PA, Caro E, et al. The Shuttle Radar Topography Mission. *Rev Geophys*. 2007;45(2):RG2004. doi:10.1029/2005RG000183
3. Durán P, Meißner C, Casso P. *A New Meso-Microscale Coupled Modelling Framework for Wind Resource Assessment: A Validation Study*. Submitted to *Renewable Energy*; 2020.
4. Launder BE, Spalding DB. The numerical computation of turbulent flows. *Comput Methods Appl Mech Eng*. 1974;3(2):269-289. doi:10.1016/0045-7825(74)90029-2
5. Gravdahl AR. Meso Scale Modeling with a Reynolds Averaged Navier - Stokes Solver Assessment of wind resources along the Norwegian coast. In: *31st IEA Experts Meeting State of the Art on Wind Resource Estimation*. Risø, Denmark; 1998:1-14.
6. Meissner C, Gravdahl AR, Steensen B. Including Thermal Effects in CFD Wind Flow Simulations. *J Environ Sci Int*. 2009;18(8):833-839. doi:10.5322/JES.2009.18.8.833
7. Vesanto J, Alhoniemi E. Clustering of the self-organizing map. *IEEE Trans Neural Networks*. 2000;11(3):586-600. doi:10.1109/72.846731
8. Kohonen TK. *Self-Organizing Maps*. 3rd ed. New York: Springer-Verlag; 2001.
9. Vesanto J, Sulkava M. Distance Matrix Based Clustering of the Self-Organizing Map. In: *International Conference on Artificial Neural Networks 2002*. Madrid: Springer, Berlin, Heidelberg; 2002:951-956. doi:10.1007/3-540-46084-5_154
10. Vesanto J, Himberg J, Alhoniemi E, Parhankangas J. SOM Toolbox for Matlab 5. *Tech*

doi:<http://www.cis.hut.fi/somtoolbox/package/papers/techrep.pdf>

11. Kohonen T. Essentials of the self-organizing map. *Neural Networks*. 2013;37:52-65. doi:10.1016/j.neunet.2012.09.018
12. Garcia D. Robust smoothing of gridded data in one and higher dimensions with missing values. *Comput Stat Data Anal*. 2010;54(4):1167-1178. doi:10.1016/j.csda.2009.09.020
13. Everitt BS, Landau S, Leese M, Stahl D. *Cluster Analysis*. 5th ed.; 2011.
14. Han J, Arya SP, Shen S, Lin Y-L. *An Estimation and Energy Atmospheric Theory of Turbulent Dissipation Boundary Kinetic Energy Rate Based on Layer Similarity*. NASA Technical Report. Hampton, Virginia; 2000.
15. Durán P, Meißner C, Rutledge K, Fonseca R, Martin-Torres J, Adaramola MS. Meso-microscale coupling for wind resource assessment using averaged atmospheric stability conditions. *Meteorol Zeitschrift*. 2019;28(4):273-291. doi:10.1127/metz/2019/0937

ISBN: 978-82-575-1693-2

ISSN: 1894-6402



Norwegian University
of Life Sciences

Postboks 5003
NO-1432 Ås, Norway
+47 67 23 00 00
www.nmbu.no